2022

Localized Surface Plasmon Resonances in Semiconductor Nanocrystals

Carl Conti III

FLORIDA STATE UNIVERSITY

COLLEGE OF ARTS AND SCIENCES

LOCALIZED SURFACE PLASMON RESONANCES IN SEMICONDUCTOR NANOCRYSTALS

By

CARL RICHARD CONTI III

A Dissertation submitted to the
Department of Chemistry & Biochemistry
in partial fulfillment of the
requirements for the degree of
Doctor of Philosophy

2022

Carl Conti defended this dissertation on March 25th, 2022.
The members of the supervisory committee were:

Geoffrey Strouse
Professor Directing Dissertation

William Oates
University Representative

Lea Nienhaus
Committee Member

Albert Stiegman
Committee Member

Robert Schurko
Committee Member

The Graduate School has verified and approved the above-named committee members and certifies that the dissertation has been approved in accordance with university requirements.

This dissertation is dedicated to plasmons. My first big hurdle in graduate school was figuring out the answer to one of the greatest questions of our time, “What even are plasmons?” I am proud to say that I finally know what a plasmon is and I hope that this dissertation can help you learn what a plasmon is too.

ACKNOWLEDGMENTS

First and foremost, I would like to thank my advisor Dr. Geoffrey Strouse. I knew after meeting you during my recruitment week that your mentorship would be invaluable and help me achieve all that I could during my graduate career. Next, I want to thank both current and former members of the Strouse group for guiding me though my PhD and helping me learn more about both my own research as well as yours. I want to specifically thank some of those who spent a significant amount of time with me in the lab, Eddie, Raul, Bella, Jason, Rodney, David, and Tony. I'd also like to thank both the Schurko group (Rob, Adam, and Robert) and Dr. Banghao Chen for all your help with SSNMR experiments. I never imagined that SSNMR would become such a significant part of my research when I arrived, but your help was integral to my success. I want to thank my non-SSNMR collaborators including the Nienhaus group (Lea, Alex, and Zach) as well as Joshua Kays and Dr. Allison Dennis. It was a great experience publishing multiple papers with both groups. I also thank Drs. Raaj Vellore Winfred and Xinsong Lin for their endless assistance with almost every instrument in the department. Thank you to the Odom group (Aaron, Kelly, Tanner, and Brennan) for introducing me to research during my undergraduate years and sparking my love of air-free chemistry. Thank you to Faith Hall, for her love and support while working on her own PhD. Lastly, I want to thank my friends and family for always supporting me on this nearly ten-year journey towards earning a PhD.

TABLE OF CONTENTS

LIST OF TABLES

LIST OF FIGURES

ABSTRACT

This dissertation examines the origins of free carrier density in semiconductor nanocrystals and relates these findings to the observed localized surface plasmon resonances (LSPRs). The first chapter introduces some of the most relevant and fundamental concepts in solid state physics, nanomaterials, plasmonics, and key analytical instrumentation used for the studies. Chapter two focuses on what is likely the most famous example of all plasmonic semiconductors, indium tin oxide (ITO) nanocrystals. ITO was one of the first semiconductors shown to exhibit a LSPR, a phenomenon previously thought to only occur in metallic systems such as gold and silver. In this chapter, the concentration of tin dopant is synthetically tuned to investigate its effect on the total number of free carriers generated and their relation to the overserved infrared LSPR. One electron chemical titrations are used to show that the Drude model is shown to be inaccurate for calculating free carrier concentrations and appropriate corrections are proposed.

The third chapter examines the effect of dopant size mismatch on free carrier generation. Al^{3+}, Ga^{3+}, and In^{3+} doped ZnO nanocrystals are synthesized and shown to exhibit unique mid-infrared LSPRs that are not dependent on dopant concentration like is seen in ITO. A combination of infrared spectroscopy, powder X-ray diffraction, and chemical titrations were used to show that better dopant/host ion size matching results in higher free carrier densities. This work is further extended in chapter four, where solid state nuclear magnetic resonance spectroscopy is used as an element specific probe for Al^{3+} and Ga^{3+} doped ZnO nanocrystals. Evidence of the formation of an insulating spinel phase (AB_2X_4) explains the lack of tunability of the LSPR with dopant concentration.

CHAPTER 1

INTRODUCTION

1.1 Band Theory

1.1.1 Extension from Atomic Orbitals to Bulk Materials

Isolated atoms possess atomic orbitals with discrete energies in which electrons can occupy. When atoms form bonds with each other in a molecule, the atomic orbitals begin to overlap and form molecular orbitals. For a system with $x \gg 1$ atoms such as a bulk crystal, there is a large increase in the amount of overlapping atomic orbitals to the point that the orbitals are no longer discrete. This leads to the formation of bands of tightly spaced orbitals that the electrons can move freely through. Bands tend to form from valence orbitals rather than core orbitals due to the smaller energy separations of the states relative to the core. The concepts of highest occupied molecular orbital (HOMO) and lowest unoccupied molecular orbital (LUMO) can be translated to band theory to describe the valence band (HOMO) and conduction band (LUMO). The valence band consists of the lower energy states that contain the bonding electrons while the conduction band represents the higher energy states and can often be described as having no electrons.[1–4]

1.1.2 Metals vs. Semiconductors vs. Insulators

The overlap (or lack thereof) of the valence and conduction bands is key to determining the electronic properties of the material. Figure 1 shows the three possible band structures. When there exists an overlap of the conduction and valence bands, the material is a metal. The electrons in the valence band are now free to move into the conduction band due to this overlap in energy of the electronic states. This phenomenon is what causes metals to be highly electrically conductive. The material can be described as a semiconductor once a small gap is

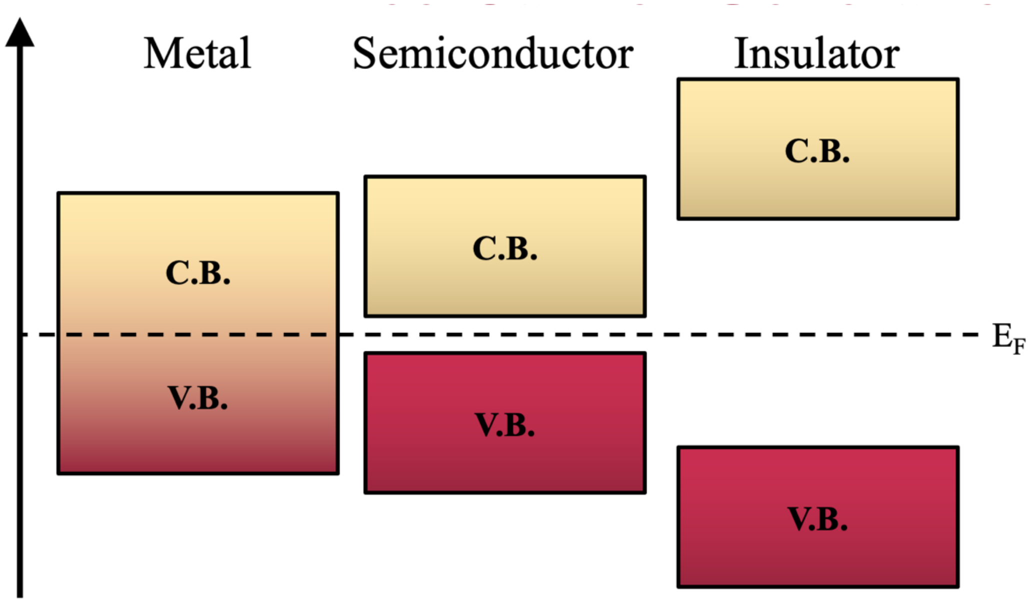

Figure 1. Examples of band diagrams for a metal, semiconductor, and insulator

introduced between the valence and conduction bands. This area where no electronic states exist is known as the band gap (E_g). The introduction of a band gap prevents electrons from the valence band from freely moving into the conduction band without sufficient energy being input into the system dependent on the size of the E_g. Common values of E_g for semiconductors range from 0.1 to 3.0 eV, which is the threshold energy required to excite an electron from the valence band to the conduction band. Semiconductors with $E_g > kT$ will have thermally populated conduction bands and higher conductivities than semiconductors with larger band gaps. Once E_g becomes large enough (>3.0 eV), the material can be considered an insulator. Insulators typically have no free electrons in the conduction band and therefore do are poor electrical conductors. Insulators are often optically transparent, since the energy of visible light (1.6-3.2 eV) is not enough to excite an electron from the valence band to the conduction band.[1–3]

1.1.3 Fermi Level and Free Carriers

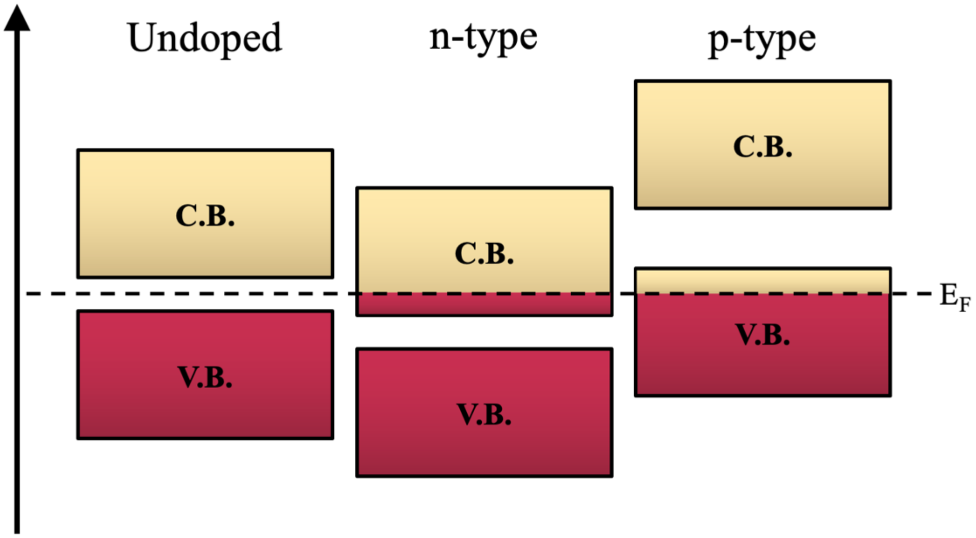

Figure 2. Band diagrams of undoped, n-type, and p-type semiconductors

The Fermi level (E_F) is the hypothetical energy at which there would be a 50% probability of an electron occupying that state. In a metal, E_F can be found somewhere within the overlapping bands. This reflects the high conductivity of metals, as there is a high probability of electrons residing within the conduction band. In undoped semiconductors and insulators, E_F is generally considered to fall in the middle of the band gap. This may seem counterintuitive, since there are no electronic states for electrons to reside in within the band gap. However, when something is forbidden in terms or quantum mechanics it means that there is simply a low probability of it occurring. A temperature dependent probability function can be used to describe the likelihood of an electron residing within the band gap. By tuning E_F, the energy at which there is a 50% probability can be controlled.[1–3]

Free charge carriers can be generated when E_F is found within either the valence or the conduction band. Free carriers are quasiparticles and can be divided into two categories, free electrons (n-type) and free holes (p-type). E_F is typically considered to be static, while the bands change energy (Figure 2) to create n and p-type semiconductors. For a n-type system, E_F resides within the conduction band of the material. This results in free electrons populating the conduction band and increased electrical conductivity. The valence band analogues of free electrons are known as holes and are created when E_F is found within the valence band. Holes are essentially a missing electron and are treated as having a positive charge. As E_F moves deeper into either the valence or conduction band, the total number of free carriers (carrier density) increases. The free carrier density is related to the conductivity of the material as well as its optical properties.[1–3]

1.1.4 Effective Mass

Free carriers often have a different mass than valence electrons. The effective mass of a free carrier (m^*) is the mass of the quasiparticle with all forces acting upon it. Free carriers can interact strongly with the lattice of the material through a variety of mechanisms, leading to values of m^* typically ranging from 0.01 to 10 times the resting mass of an electron (m_e). Knowing the m^* of a free carrier is key to understanding the conductivity, carrier mobility, as well as optoelectronic properties of a material. Forces that can impact m^* include electron-electron scattering, electron-phonon coupling, surface scattering, impurity scattering, and more. All of these are forces that couple the free carrier to the lattice or impact the mean free path of the carrier. The stronger the coupling or the more scattering centers that are present, the more m^* will increase. As m^* increases, carrier mobility decreases as well as the electric conductivity of the material. Since m^* is related to the momentum of the free carrier, the degree of curvature of the band structure reflects the change in m^*. As the degree of curvature of the band increases, m^* will decrease.[1–3]

1.2 Doping Schemes for Free Carrier Generation

1.2.1 Intrinsic vs. Extrinsic Doping

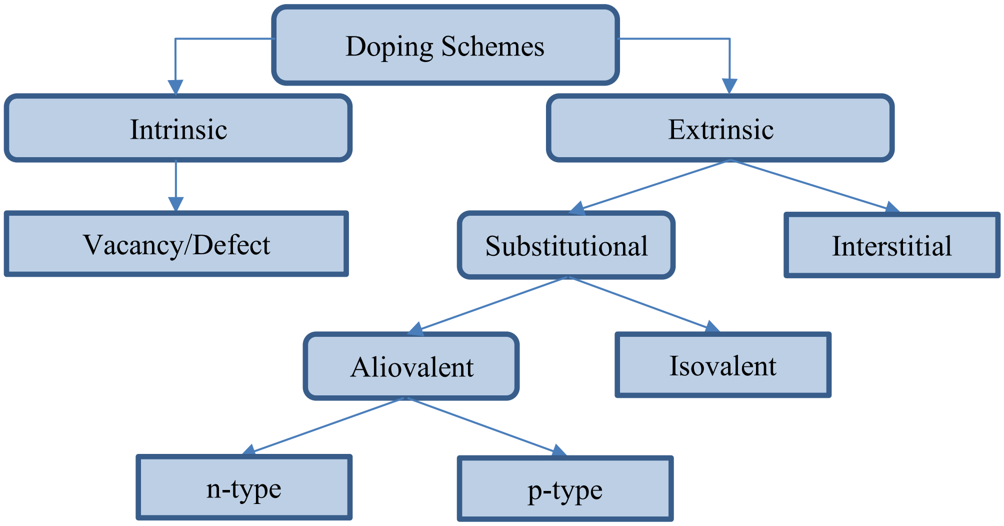

Scheme 1. Flowchart of doping mechanisms

All possible semiconductor doping mechanisms can be divided into one of two classes, intrinsic and extrinsic doping. Extrinsic doping is what traditionally comes to mind, where an impurity is added into the semiconductor at a low concentration to alter its electronic, optical, and/or structural properties. One of the most famous examples of extrinsic doping is the case of phosphorus doped silicon. Very small amounts (ppm) of phosphorous atoms are incorporated into the silicon crystal structure, resulting in a net charge imbalance due to the differing valence electron counts of silicon and phosphorous. Free electrons (e^-) are then generated to compensate for this charge imbalance, creating a n-type semiconductor. A p-type silicon semiconductor can be created through extrinsic doping by choosing boron as the dopant instead of phosphorous. Since boron has one less valence electron than silicon, one free hole (h^+) is generated for every boron atom doped into the silicon crystal.[5]

Intrinsic doping constitutes a smaller class of materials since the dopant is a defect within the material and no outside impurities are introduced. This typically occurs due to the semiconductor becoming off stoichiometric during either the formation of the crystal or because of post-synthetic modification. Intrinsic doping can be either n or p-type and used to control the number of free carriers generated in the same way that extrinsic doping operates. However, the key distinction between the two is that no foreign atoms are introduced to the semiconductor for an intrinsic doping process.[6]

1.2.2 Vacancy Doping

Vacancy doping is the most common type of intrinsic doping. One of the most famous examples is n-type ZnO, where the presence of oxygen vacancies results in a deviation from the 1:1 stoichiometry and generates free electrons to compensate for the charge imbalance created.[7,8] The pure ZnO material will possess zero free carriers, while the n-type carrier concentration will increase as the number of oxygen atoms in the system decreases. Each oxygen vacancy generates two free electrons because the oxygen ion carries a charge of two minus. Vacancy doping can also occur for the cation of the semiconductor, although it is less common.

1.2.3 Isovalent vs. Aliovalent Doping

Extrinsic dopants often incorporate substitutionally, meaning the foreign dopant atom replaces an atom within the crystal and maintains the same overall crystal structure. Substitutional dopants can then be classified into two categories, isovalent and aliovalent. Isovalent dopants are those with the same oxidation state as the atom that they are substituting.[6,9] An example of isovalent doping is Ga:In_2O_3. The gallium dopant will substitute at the indium sites and both ions possess a three plus charge. This means that no free carriers will be generated because no charge imbalance is created by the incorporation of gallium. However, the size differs between gallium and indium, which can affect the energies of phonons within the material.

Aliovalent dopants do have a difference in oxidation state from the atom that they are substituting. Therefore, aliovalent doping does result in a net charge imbalance and the generation of free carriers. These free carriers can be n or p-type depending on the identities of the dopant and host atoms. An famous example of aliovalent doping is $Sn:In_2O_3$.[10–12] Here, the tin can possess either a two or four plus charge, while the indium will remain three plus. In either case, the tin will be aliovalent, create a net charge imbalance, and therefore generate free carriers. The concentration of the aliovalent dopant is directly correlated to the resulting free carrier concentration. The larger the difference between the dopant oxidation state and host ion oxidation state, the greater the number of free carriers that will be created is.

1.2.4 Interstitial Doping

While substitutional dopants sit on atomic crystal sites, interstitial dopants lie in the spaces within the crystal structure where there are no host atoms. Since no atom is being replaced, the total additional charge created by interstitial dopants needs to be compensated for. One example of interstitial doping is in $Cs:WO_3$.[13,14] Here, the cesium dopant ions lie in the negative space of the WO_3 crystal structure. Interstitial doping is typically limited to small dopant ions as they must fit within the crystal structure with minimal perturbation.

1.3 Bulk vs. Nanoscale Materials

1.3.1 Effects of Surface Area to Volume Ratio

The optical, chemical, and electronic properties of a material can change significantly as size decreases to the nanoscale regime. One of the most important factors causing such change is the relation between surface area and volume (SA:V). This ratio is one of the defining characteristics of nanomaterials. In a bulk material, SA:V is extremely low. This means that the properties of the sample are determined by the atoms that are not at the surface, since they constitute a much higher percentage of the sample. Bulk materials can be thought of to behave more ideally since >99% of the atoms reside in environments reflecting the unit cell if it is a crystalline material. Deviations from this chemical environment will exist at the surface, but the surface atoms make up too small of a percentage to affect the properties of the material.[15]

The opposite is true for a nanoscale material. SA:V is very high at the nanoscale, meaning that a significant portion of the atoms reside at or near the surface of the material. This results in large deviations from the ideal crystal structure to dangling bonds and incomplete unit cells. The surface is also an interface between the material itself and the surrounding environment. Therefore, most of the atoms within the nanoscale material will interact with the surrounding environment instead of other atoms that make up the material. This makes nanoscale materials much more sensitive to changes in their environment and can cause significant deviations in the crystal structure near the surface of the particle.[15]

1.3.2 Size Effects on Electronic Properties

The electronic properties of a material can change drastically as the size moves into the nanoscale. Specifically, there exists a regime in between molecular and nanoscale systems where bulk band theory begins to break down. This is known as quantum confinement and occurs when a material becomes smaller than its Bohr radius. When a material is within the quantum confinement regime, its band gap becomes inversely proportional to its size. Many quantum confined nanomaterials are emissive, therefore the color of this emission can be tuned by controlling the size of the particles. Eventually, the particle becomes so small that discrete electronic states form. These states lie within the bandgap and severely alter the electronic and optical properties of the sample.[16]

1.3.3 Surface Effects on Free Carriers

Nanoscale confinement can also affect both the number of free carriers and their properties. As the mean free path of the free carrier is reduced, so too is the carrier mobility. The carrier mobility is related to both its effective mass as well as the electric conductivity of the sample. The maximum mean free path of a free carrier in a nanomaterial is inherently limited by the dimensions of the particle. This confinement can be in one, two, or three dimensions and each of these vary in how the free carrier is affected. In a 0D material, such as a spherical quantum dot, the majority of the sample can consist of surface atoms. This reduces the mean free path of the free carriers by introducing larger amounts of surface scattering. The surface of a nanocrystal can also trap free carriers. Once a free carrier becomes pinned at the surface, it is effectively localized and its effective mass increases. These carriers are more similar to valence electrons rather than conduction electrons.[15]

1.4 Surface Plasmon Resonances and LSPRs

1.4.1 Permittivity

An electrically insulating material that can be polarized is known as a dielectric. In this instance, polarization refers to the ability of the field to form an instantaneous electric dipole in the material. This electric dipole forms because of shifting electric charges within the insulating material. Permittivity is the measure of the degree of polarizability of the material as a function of the frequency, magnitude, and direction of the applied electric field. Permittivity is often discussed in terms of relative permittivity, which is a normalizes absolute permittivity by dividing the value by the permittivity of free space constant. The relative permittivity of a material as a function of frequency can be represented by a complex dielectric function consisting of a real and an imaginary component. The real component represents the ability of the material to scatter light, while the imaginary term is the lossy or absorptive term.[17]

1.4.2 Surface Plasmon Resonances

Figure 3. Depiction of a SPR wave at the surface of a material

When the dielectric function is a positive and real function, then all optical interactions with the material will consist purely of scattering If the dielectric function is complex with a positive real component, then the optical interactions will also include Rayleigh scattering. A third possibility occurs when the dielectric function is complex and contains a negative real term. The optical extinction reaches a maximum at the point that the real component crosses zero and this phenomenon is known as a surface plasmon resonance (SPR). A SPR can be thought of as a collection of free carriers that oscillate and propagate across a surface when excited with a resonant frequency of light, as shown in Figure 3. SPRs can be observed in materials with high carrier densities such as noble metals like gold and silver.[6]

1.4.3 Localized Surface Plasmon Resonances

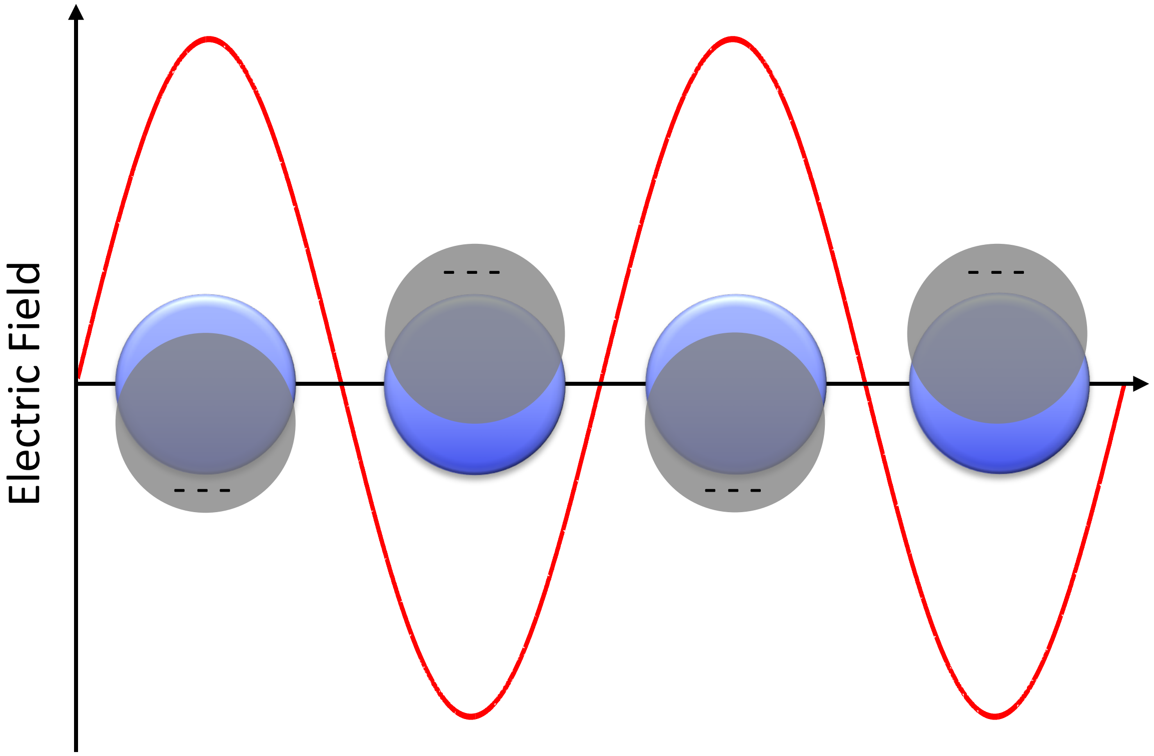

Figure 4. Oscillation of plasmon in response to incoming resonant electric field

When a plasmonic material is confined so that the diameter of the particle is less than the wavelength of the SPR divided by 20, the SPR is no longer free to propagate across the surface of the material. Instead, the SPR oscillates back and forth and is now known as a localized surface plasmon resonance (LSPR).[6] This makes LSPRs unique in that they can overcome the diffraction limit of light. Nanocrystals (NCs) as small as 5 nm can host LSPRs and confine light from the visible through the infrared regions. One powerful example of this is aluminum doped zinc oxide NCs that can strongly absorb 5000 nm infrared light even at a size of 10 nm in diameter. Figure 4 illustrates how the free carriers collectively oscillate when irradiated with resonant light. In this example, the free charge carriers are conduction band electrons (n-type) and therefore the plasmon moves opposite of the maximums in electric field generated by the incoming light.

1.4.4 Sensitivity to Local Dielectric Environment

LSPRs are interfacial dielectric phenomena, which causes these quasiparticles to be extremely sensitive to changes in the dielectric function at the surface of the NC. As the local dielectric field changes, the frequency of the observed LSPR is tuned. The three major dielectric constants the affect the LSPR are the NC itself, the capping ligand, and the surrounding environment. The environment that the NCs reside could be a solvent, air, or potentially even other NCs depending on the packing density. The dependence of the LSPR frequency on the dielectric constant of its environment makes plasmonic NCs powerful chemical sensors. As the local dielectric constant changes, the plasmon will shift to higher or lower frequencies depending on the sign of the change.[18]

1.4.5 LSPR Extinction

The extinction coefficient is a measure of how well a molecule or material absorbs a particular frequency of light. It is used to compare the absorbing capabilities of different samples. Typical values for poor absorbers such as lanthanides are in the range of 10^2-10^3 M^{-1}*cm^{-1}, while common molecular dyes reach values of 10^6 M^{-1}*cm^{-1}. One of the most unique properties of LSPRs is their extraordinarily high molar extinction coefficients. A study of plasmonic Sn:In_2O_3 (ITO) NCs of various sizes and doping levels revealed extinction coefficients as high as 10^8 M^{-1}*cm^{-1}, which is four orders of magnitude higher than commercial infrared dyes.[19] This means that plasmonic materials are extremely efficient light harvesters, which is the first step towards their applications in photocatalysis and energy transfer.

1.4.6 Near Field Enhancement

One of the most well-known applications of plasmonic materials is in surface enhanced Raman spectroscopy.[20–22] This variation on a typical Raman measurement involves adsorbing the sample onto a rough metallic surface, typically gold, and subsequent measure of the Raman scattered light. The plasmonic gold surface interacts with the sample and results in an enhancement of the detected Raman signal of up to 10^{11}.[23] This drastic increase in sensitivity can even allow for the detection of single molecules. The mechanism of this increase in scattering is due to the plasmonic modes at the gold surface. The adsorbed sample can interact with these plasmonic modes in the near field, which is typically defined as within one wavelength. In a typical Raman experiment, the wavelengths of incident light used are from the visible region. This means that the near field regime is approximately 0.5-0.8 microns from the gold surface. Adsorbed samples that enter this region undergo an effect called near field enhancement (NFE), which is the mechanism that causes the drastic increase in Raman signal from the sample.[22]

Hot spots of increased near field enhancement typically form at corners or edges of plasmonic materials. While a spherical NC may have slight hot spots at the poles, a cubic morphology results in increased NFE at each of the corners.[24] It is for this reason that a roughened metal surface is used for surface enhanced Raman spectroscopy to maximize the amount of NFE. By increasing the number of edges and corners, the number of localized NFE hot spots will increase. Various gold morphologies and packing densities have been compared to measure the increase in sensitivity of Raman measurements.[23] NFE increases with anisotropy of the NCs and therefore so does the measured Raman signal. The number of NFE hot spots can also increase as interparticle spacing decreases. As the number of NC-NC interactions increase, new hot spots can form and the localization of the NFE can also increase. The third method of increasing NFE is to increase the quality factor (Q-factor) of the LSPR. The Q-factor is a measure of the plasma frequency of the LSPR divided by the full width-half maximum (FWHM) of the extinction feature. The degree of NFE increases with Q-factor, therefore higher energy LSPRs with a narrow linewidth are better options for increases Raman sensitivity.[25,26]

1.5 Drude Model

1.5.1 Basis of the Drude Model

The Drude model is one of the earliest attempts to describe the conduction of electrons in a solid. The original Drude model predates Rutherford's model of the atom and was established shortly after Thompson's discovery of the electron. Drude built his model on the assumption that a solid was composed of positively charged scattering centers and that a sea of negatively charged electrons created the neutral charge.[27] These electrons are free to move around the solid under the assumption of Brownian motion. The Drude model uses the kinetic theory of gasses to accomplish this and therefore treats the sea of electrons as a gas. The frequency dependent dielectric function of a solid can be derived from the Drude model as shown in the following equation,

$$\varepsilon(\omega) = 1 - \frac{ne^2}{\varepsilon_0 m^* \omega^2} \tag{1}$$

where ω is the frequency, n is the total number of free electrons, e is the charge of an electron, ε_0 is the permittivity of free space, and m^* is the effective mass of the charge carrier.[28] This function describes the total dielectric function of the material and can be used to describe the LSPR. When the frequency is held constant at the plasma frequency (ω_p), the equation can be rewritten as follows:

$$\omega_p = \sqrt{\frac{ne^2}{\varepsilon_0 m^*}} \tag{2}$$

where ω_p represents the resonant frequency of the plasmon oscillation. This equation is used extensively in the literature to relate the experimentally measure ω_p to the free carrier density of the sample.[9,29–33] As the number of free carriers increases, so too does the frequency of the observed LSPR. The inverse relationship is true for the effective mass of the free carrier, where decreasing m^* results in higher energy LSPRs.

1.5.2 Relation between Plasma and Plasmon Frequency

While the plasma frequency of a SPR can be determined by absorption experiments alone, the ω_p of a LSPR can differ from the observed LSPR frequency (ω_{LSPR}). This relationship can be described by the following equation:

$$\omega_{LSPR} = \frac{\omega_p}{\sqrt{\varepsilon_\infty + 2}} \tag{3}$$

where ε_∞ represents the high frequency dielectric constant of the material.[6,11] This effect happens due to the plasmon no longer being free to propagate across the surface of a material and instead being localized. An example of this is seen in the LSPR of ITO NCs, where ε_∞ is equal to 4.08.[34] This results in the frequency of the observed LSPR being almost 2.5 times lower than the actual ω_p. Assuming these two values to be identical can result in large errors in the calculation of the free carrier density using equation 2.

1.5.3 Frequency Independent and Dependent Damping

The Drude or free electron contribution to the overall dielectric function of a material can be described using the following equation:

$$\varepsilon_D(\omega) = -\frac{\omega_p^2}{\omega^2 + i\omega\Gamma} \tag{4}$$

where Γ represents a damping constant of the plasmon resonance. This damping constant describes the sum of all possible free carrier scattering mechanisms, which ultimately determine the lifetime and the linewidth of the plasmon. These scattering mechanisms include electron-

electron (el-el), hole-hole (h-h), el/h-phonon, el/h-impurity, interband, and surface scattering.[28] These mechanisms can result in a decreased mean free path of the carrier, increased effective carrier mass, and shorter plasmon lifetimes.

The damping constant can be thought of as frequency independent or dependent. Ignoring frequency dependence typically results in poor fits of the LSPR and can lead to incorrect calculations of the free carrier density and effective mass. To account for frequency dependent damping, the constant is broken down into four more constants in the following equation:

$$\Gamma = \gamma_L - \frac{\gamma_L - \gamma_H}{\pi}\left(\tan^{-1}\left(\frac{\omega - \gamma_X}{\gamma_W}\right) + \frac{\pi}{2}\right) \tag{5}$$

where γ_L is the low frequency damping constant, γ_H is the high frequency damping constant, γ_X is the crossover frequency, and γ_W is the crossover width. The low and high frequency damping constants are named with respect to the resonant frequency of the plasmon. The crossover frequency is the region where the damping changes from high to low and the crossover width defines the boundaries of this region. Most plasmonic materials exhibit asymmetric extinction features reflecting the frequency dependence of the various scattering mechanisms.[28]

1.6 Noble Metal vs. Semiconductor LSPRs

1.6.1 Typical LSPR Frequencies

The earliest known plasmon resonances were observed in noble metals such as silver and gold.[32,35,36] Metals intrinsically possess high free carrier densities due to their overlapping valence and conduction bands. This results in high frequency LSPRs that can be found in the visible region. Since the number of free carriers cannot be changed in a metallic system and resonant wavelength of a LSPR is highly dependent on the free carrier concentration, noble metal plasmons are typically limited to visible wavelengths.[32] Semiconductors are defined by the introduction of a band gap and therefore do not have overlapping valence and conduction bands. This results in semiconductors having far fewer free carriers than metals. Semiconductor LSPRs are thus typically found in the near and mid-infrared regions.[37,38]

1.6.2 Advantages of Semiconductors over Noble Metals

The ability to host infrared LSPRs provides semiconductors several advantages over noble metals. One of these is the lack of absorbing features in the visible region. This means that semiconductors can host strongly absorbing plasmon resonances while simultaneously remaining completely transparent to the human eye. Many plasmonic semiconductors have intrinsically wide bandgaps ($Sn:In_2O_3$, Al:ZnO, TiO_{2-x})[10,39,40] and are especially suited for applications requiring the transmission of visible light. The wide range of infrared LSPR frequencies observed in semiconductors also opens the door to many applications that are inaccessible by noble metals. Examples of these include thermal waste management,[41] on-resonance surface enhanced Raman,[22] photon upconversion,[42] and more.

1.6.3 Tuning Free Carrier Density

The most important advantage of plasmonic semiconductors over noble metals is the ability to tune their free carrier density and therefore the frequency of the LSPR. Free carrier concentrations are commonly tuned via aliovalent doping, with the most famous exampling being plasmonic ITO NCs.[10,29] By controlling the concentration of tin dopant, the LSPR can be tuned from the mid-infrared region to as high in energy as 1600 nm. This method can be used to control free carrier density in both n and p-type systems.[6,18] The concentration of interstitially incorporated dopants can also be used to control the number of free carriers, as seen in the case of $Cs:WO_3$ NCs.[13,14] Free carrier density can also be tuned using intrinsic doping methods such as vacancy doping. Creating oxygen vacancies in WO_{3-x} NCs results in two free electrons generated per vacancy. The number of oxygen vacancies can be controlled by varying synthetic conditions, resulting in specific WO_x phases with different LSPR frequencies.

1.6.4 Tuning Effective Mass

Although carrier density is the primary method for tuning LSPR frequencies seen in the literature, it is not the only way. The plasma frequency of a material is also inversely proportional to the effective mass of its free carriers. Heavier carriers result in low energy LSPRs, while lighter carriers can push the LSPR even into the visible region. This is another advantage of semiconductors over noble metals, where the effective mass of the free carriers can be difficult to change. One simple method for tuning the effective mass without altering the carrier density in a semiconductor is through isovalent substitutional doping. By replacing a host atom with a larger or smaller dopant atom of the same valency, the strength of free carrier-phonon interactions can be tuned, resulting in a tunable m^*.

1.7 Analytical Instrumentation

A wide variety of spectroscopic techniques are needed to fully characterize plasmonic semiconductor NCs. The information that can be obtained is dependent on the frequency of electromagnetic spectrum that is used to probe the sample. This section details what can be learned by irradiating a sample using ultraviolet (UV), visible, infrared (IR), and radio frequencies.

1.7.1 Ultraviolet-Visible-Near Infrared Spectroscopy

Ultraviolet-Visible-Near Infrared (UV-Vis-NIR) spectrometers use the frequencies listed in the name to measure the absorption of a sample. This is accomplished by probing the sample with a single wavelength at a time and measuring the amount of light that is transmitted through

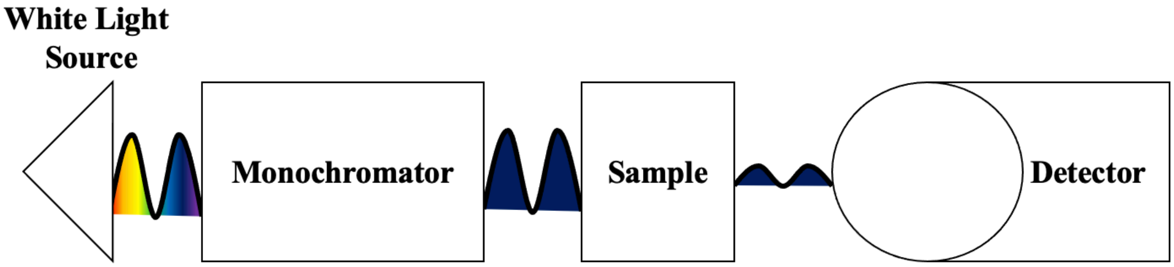

Figure 5. Dispersive setup for a UV-Vis-NIR spectrometer

the sample. The measured transmittance can then be converted to absorbance using the Lambert-Beer law:

$$A = \varepsilon bc \tag{6}$$

where A represents the absorbance, ε is the molar extinction coefficient of the sample, b is the optical pathlength, and c is the concentration of the sample. In practice, this is accomplished by using a white light source (or infrared lamp) that contains all the frequencies of interest and separating each wavelength by using a monochromator. The angle of the dispersive grating within the monochromator is changed so that sample is probed by a single wavelength, which is systematically tuned from low to high energy. The sample is suspended in an appropriate solvent at a dilute concentration to limit sample-sample interactions. The transmitted light is then measured by a detector and converted to absorbance as shown in Figure 5.[43]

A blank spectrum of the is first collected to correct for background absorption from factors such as the solvent or the cuvette. Afterwards, the blank is replaced with the sample and the same experimental parameters are used to measure the sample. Simple subtraction of the blank spectrum from the sample spectrum results in the absorption of the sample by itself. Valence electron transitions are typically observed in the UV and visible regions. UV-Vis-NIR experiments can also be used to measure the bandedge absorption of NCs as well as the LSPR extinction feature for samples with high plasma frequencies. Changes in the free carrier density will result in shifts of both the LSPR and optical band gap, therefore UV-Vis-NIR experiments are critical towards examining the impact of doping on the material's properties.[43]

1.7.2 Fourier Transform Infrared Spectroscopy

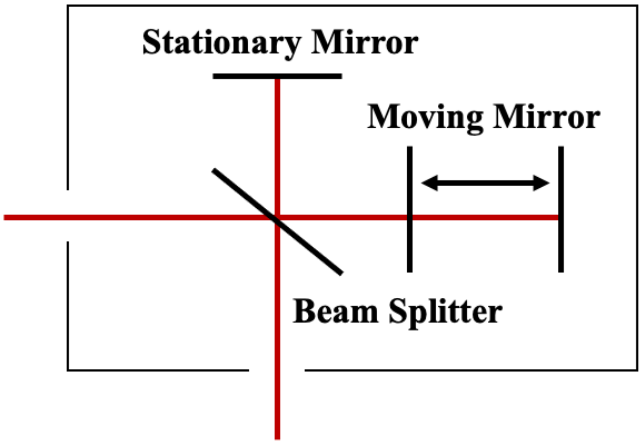

Figure 6. Michelson interferometer used to generate interferogram in FTIR measurements

UV-Vis-NIR spectrometers are typically limited to about 3000 cm^{-1} in the IR region. This is due to the limits of detection in the IR that can be reached using a dispersive setup. However, there is a great deal of important information in the mid and far infrared regions (4000-50 cm^{-1}) including vibrational transitions and low energy LSPR features. Rather than using a dispersive setup which includes a monochromator and measures each frequency individually, modern IR spectrometers utilize a Michelson interferometer (Figure 6) to measure all frequencies at the same time.[44]

The interferometer works by splitting the broadband IR light into two beams, which are directed at a stationary and a moving mirror. When the mirrors are the same distance away from the beam splitter, the light will recombine constructively at the beam splitter. When the moving mirror is positioned so that the phase of the light is modulated by half of a period, the light will then recombine destructively. The position of the moving mirror is adjusted throughout the measurement to create varying degrees of interference. This light is then directed at the sample and detector analogous to a UV-Vis-NIR spectrometer. Rather than measuring the intensity of each wavelength independently, the intensity of the broadband light is measured over time. This plot of intensity vs. time is known as an interferogram. A background interferogram is first collected and subtracted from the sample interferogram. The interferogram can then be converted from the time domain into the frequency domain by using a Fourier transform, giving us the name Fourier transform infrared (FTIR) spectroscopy. This instrumental setup allows for faster data collection with less background noise, making FTIR measurements fast and accurate. The resolution of the spectrum can be increased by moving the mirror over a greater distance and the S/N can be increased by collecting more scans.[44]

1.7.3 Nuclear Magnetic Resonance Spectroscopy

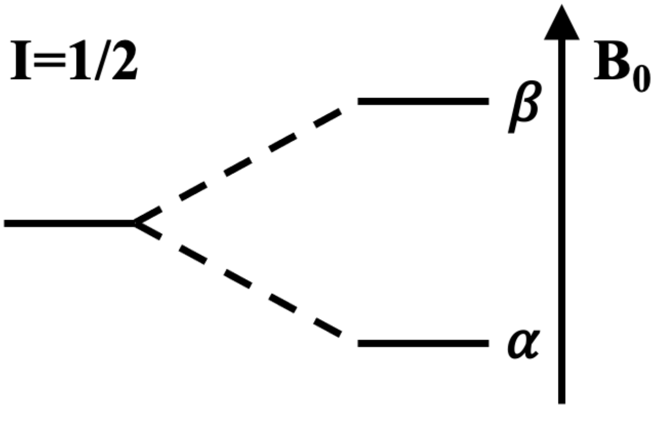

Figure 7. Zeeman splitting of the nuclear spin under a magnetic field for I=1/2

While UV-Vis-NIR and FTIR examine electronic and vibrational transitions respectively, Nuclear Magnetic Resonance (NMR) spectroscopy probes the absorption of radio frequencies by nuclear spins. These measurements reveal information about the local chemical environment of a specific element of interest, a major advantage over many other non-selective optical measurements. NMR operates under many of the same principles as other steady-state absorption techniques.

When subjected to a static magnetic field, a nucleus with a spin of (I) of 1/2 will undergo a process known as Zeeman splitting and the degeneracy of the two spin states will be lifted. This results in the spin 1/2 state (α) being of lower energy than the spin -1/2 state (β), as shown in Figure 7. Analogous to the HOMO – LUMO transition in UV-Vis, a nuclear spin can be excited from the lower energy α state to the higher energy β state when a photon matching the energy of this transition is absorbed. In NMR, this resonance condition corresponds to the radio frequency (r.f.) region of the electromagnetic spectrum.[45]

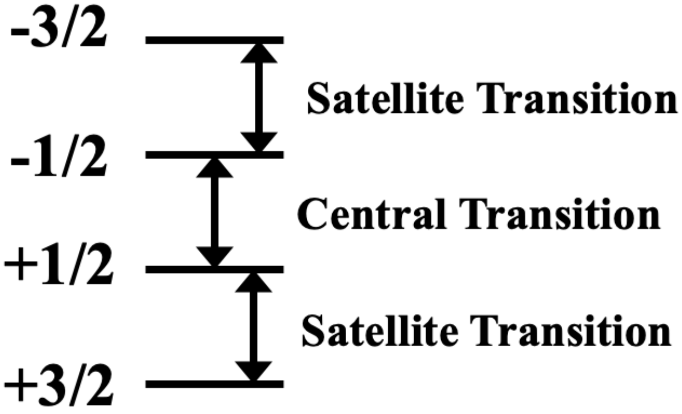

Figure 8. Allowed NMR transitions for a I=3/2 system

NMR signals can be observed for any nuclei that possesses a non-zero value for its nuclear spin. If I=0, then the nuclear spin state will not be separated under a magnetic field and there is no transition to analyze. This is the case for isotopes where both the number of protons and neutrons is even, such as ^{12}C or ^{16}O. Nuclei with I=1/2 are known as dipolar and exhibit only one NMR transition. Common dipolar nuclei frequently studied via NMR include ^{1}H, ^{13}C, ^{19}F, and ^{31}P. When I>1/2, the nucleus is known as quadrupolar, and the number of possible transitions increases. For example, a spin 3/2 nucleus will split into four non-degenerate spin states under a magnetic field (Figure 8). The introduction of satellite transitions results in a broadening of the observed NMR signal. It is important to note that only m=±1 transitions are allowed, resulting in only three possible transitions. Nuclei can have spins up to 9/2 (one central and 8 satellite transitions) such as ^{115}In and ^{209}Bi. The degree of quadrupolar splitting and therefore the linewidth of the resulting NMR feature is dependent on the strength of the magnetic field of the spectrometer. Experiments on nuclei with large quadrupolar moments are typically performed at high magnetic fields to narrow the quadrupolar broadening of the features for easier interpretation.[45]

To measure the NMR spectrum of a sample, it is placed inside the bore of the spectrometer and subjected to the static magnetic field dependent on the instrument. The nuclear spins align parallel (or anti-parallel) to the magnetic field B_0. A short r.f. pulse is then used to excite the sample, which knocks the spin out of alignment with B_0. The frequency of the pulse is tuned to match the resonance condition of the nucleus that is to be observed. This induces an orthogonal magnetic field (B_1) to be generated that can then be measured by the current it is causes in the coil surrounding the sample. The strength of this current is then measured over time and used to create what is known as the free induction decay or FID. The FID can then be converted into the frequency domain by using a Fourier transform, analogous to FTIR, resulting in a NMR spectrum. The simplest and the most common pulse sequence is known as a Bloch decay. It uses a single 90° pulse to align the spins perpendicular to B_0 and then the FID is measured after the completion of this pulse.[45]

1.7.3.1 Solution NMR. Most NMR experiments are performed in the solution state. This is advantageous compared to solid state because the sample is free to rotate and tumble, which causes any anisotropy to be averaged. Samples are first dissolved in an appropriate solvent such as a deuterated chloroform. Using a deuterated solvent is critical when performing ^{1}H NMR so that the signal from the solvent protons does not drown out the sample of interest. Deuterated solvents are also used to lock the spectrometers by calibrating to the deuterium signal. This is important to account for field drift and is also used to shim the magnetic field. Shimming is a process where the magnetic field is adjusted to eliminate inhomogeneities that would otherwise result in broadening of the NMR signals.[45]

Solution NMR is often used to analyze small organic molecules for purity and chemical structure. Today, ^{1}H spectra can be acquired in a few seconds and ^{13}C in a few minutes. Solution NMR is also utilized to examine ligands coordinated to the surface of nanocrystalline materials. Since the molecules are bound to a relatively large crystal, the ligands are not free to tumble like they typically are in a solution measurement. This results in an enhancement of the nuclear relaxation rate and a broadening of the observed peaks. The increase in peak width helps identify which ligands are bound to the surface of the NCs and which are simply dissolved in the solution. Multidimensional pulse sequences can also be utilized to examine homo- and heteronuclear spin couplings of various nuclei. Such experiments can help identify how ligands are bound and what the surface of NCs look like. However, solution NMR measurements are often inadequate for studying the NC itself due to factors such as solubility, sample concentration, and probe capabilities. Solid state NMR spectrometers can be used to address these issues.

1.7.3.2 Solid State NMR. Solid state NMR (SSNMR) spectrometers operate using many of the same principles as solution measurements, except for that the sample is prepared in the solid state, typically as a fine powder. There are number of additional challenges that arise when performing SSNMR measurements compared to common solution studies. One of the primary issues is that the sample is not free to tumble like it is in solution, therefore the various anisotropic NMR interactions are not averaged out. This results in much broader and intricate lineshapes that are more different to interpret but contain much more information about the sample.[46]

SSNMR experiments have several advantages over solution measurements. The most important of these is that samples that are too large to be dissolved, such as NCs and bulk materials, can be measured without the need for a deuterated solvent. This also means that there is no need to lock on the deuterated solvent because none is used. Instead, SSNMR experiments are calibrated using a reference standard for the nucleus of interest. Since SSNMR signals are much broader than solution measurements, it is also unnecessary to shim the magnet. Shimming is very important for solution measurements, where the observed signals are typically very narrow. However, the magnetic fields of today's spectrometers are already homogenous enough for accurate solid-state measurements without the need for shimming due to their increased linewidths.[46]

One of the most important developments in the field of SSNMR was the introduction of magic-angle spinning (MAS). This technique involves rotating the sample around an axis at 54.74° (known as the magic angle) to simulate motion and overcome some of the anisotropic interactions. Samples are typically spun at rates from 1-35 kHz but can even go as high as 100 kHz. The spinning rate must be greater than the linewidth of the dipolar coupling to completely average the anisotropy to zero. The spinning speed is often insufficient, and a manifold of spinning sidebands (ssb's) is observed. These ssb's are sharp peaks that appear at multiples of the MAS rate away from the isotropic chemical shift. ssb's can be identified by changing the MAS rate and observing which peaks in the spectrum shift in frequency. This is also used to identify the isotropic chemical shift, as it is not necessarily the peak of the highest intensity.[46]

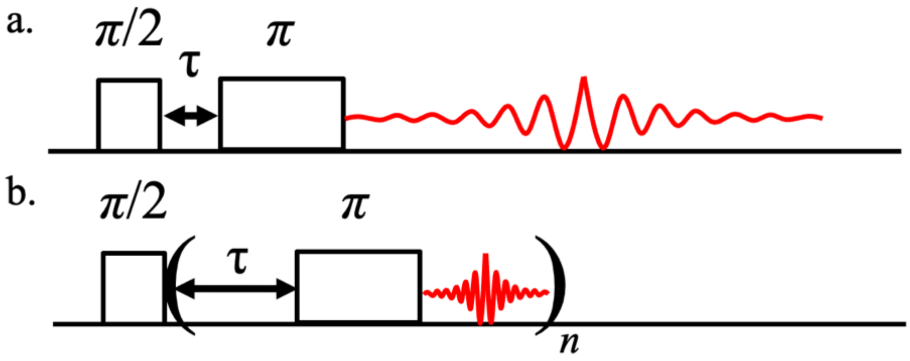

Figure 9. Schematics of a (a) spin-echo pulse sequence and (b) a CPMG pulse sequence

Specialized pulse sequences are often used in SSNMR experiments to increase S/N or to measure broad patterns. One of the most common pulse sequences is known as spin-echo. It consists of a single 90° pulse followed by a delay period (τ), and then a 180° pulse that refocuses the relaxing spins (Figure 9a). The acquisition then begins once the signal has reached maximum intensity and the FID is recorded. This pulse sequence helps maximize S/N and avoid issues due to ringdown by delaying the start of the acquisition from the end of the last pulse. The first pulse can also be changed to other angles (30°, 45°, etc.) to cut down on the recycle delay so that more scans can be collected in a shorter period.[46]

The spin-echo sequence can be flipped (180° pulse, followed by 90° pulse) to measure the spin-lattice relaxation (T_1) of a sample using what is known as a saturation recovery experiment. The delay time between the pulses is systemically changed to modulate the signal intensity and phase of the NMR feature. The resulting change in intensity can then be fit to an exponential to calculate T_1. T_1 is also known as longitudinal relaxation and is the measure of the nuclear spin decay in the z direction, in line with B_0. The length of T_1 is often the limiting factor determining the recycle delay, which is how long the spectrometer waits between scans. The recycle delay must be set to at least five times greater than the T_1 to allow for the nuclear spin to fully relax to its ground state.[46]

Another common SSNMR pulse sequence is known as Carr-Purcell Meiboom-Gill or more commonly, CPMG. This sequence is similar to a spin-echo but with the addition of more 180° pulses with the same echo delay to continually refocus the spins (Figure 9b). CPMG sequences create a spikelet pattern that outlines the lineshapes of the NMR features of interest. By concentrating the signal into smaller frequency ranges, the overall S/N can be increased substantially.[47,48]

CPMG sequences can also be used to measure the spin-spin relaxation (T_2). T_2 relaxation, also known transverse relaxation, measures how fast the nuclear spin decays in the xy plane, orthogonal to B_0. The decay of the overall intensity with each subsequent echo can be fit to an exponential to extract T_2. T_2 relaxation can be related to linewidth of the observed feature, where shorter values correspond to broader NMR signals. CPMG sequences are ineffective for samples where T_2 is so short that multiple refocused echoes cannot be generated.[46]

One of the most important pulse sequences that can only be utilized in the solid state is cross polarization-magic angle spinning or CP-MAS. CP-MAS uses two channels on the spectrometer simultaneously, typically the ^{1}H and X channels, to enhance the S/N of an experiment while often decreasing the recycle delay (time between scans). While the sample is spinning on the magic angle, a proton nearby the nucleus of interest is first irradiated to build up sufficient polarization. This polarization is then transferred to the nearby X nuclei over a period known as the contact time. The CP process leads to the X nucleus being as easy to polarize as a proton and the recycle delay is now only dependent on the T_1 of the proton, which is typically much shorter than other common SSNMR nuclei. Efficient CP can be accomplished despite the two nuclei having different Larmor frequencies by relying on what is known as the Hartmann-Hahn matching condition. The power on each channel is adjusted so that both spins precess at the same frequency in the rotating frame, a process known as spin-locking. The contact time can then be adjusted to achieve CP, typically limited to about a 1 nm distance between the nuclei.[46]

Recently, SSNMR has become more user friendly to non-experts as pulse sequence and spectrometer design has improved. This has allowed for users in the nanocrystal and quantum dot communities to leverage the technique as an element specific probe for investigating nanomaterials. The Strouse group has previously used ^{113}Cd and ^{77}Se SSNMR to investigate surface reconstruction in CdSe quantum dots (QDs).[49] This 2004 investigation was one of the first examples of the power of SSNMR towards advancing our understanding of nanocrystalline structure. In this work, a 2D ^{77}Se {^{1}H} HETCOR spectrum was measured to identify the unique ^{77}Se sites located on the surface of the QD. This single experiment using a 7 T spectrometer required 21 days to collect, rendering similar experiments infeasible due to time and cost constraints. Nowadays there is much greater access to higher field spectrometers and more sophisticated pulse sequences that can greatly reduce the amount of experimental necessary for such measurements.

One such method that can greatly improve S/N, reduce experiment time, as well as selectively probe the surface of a nanomaterial is dynamic nuclear polarization (DNP) NMR.

DNP operates in a similar fashion to CP-MAS, only the initial nucleus that is polarized is instead a nearby electron. While protons have much higher gyromagnetic ratios than all other nuclei, the value for electrons is substantially higher. This means that the Larmor frequency of an electron can be found in the microwave region rather than the radio wave, a fact already leveraged in the electron paramagnetic resonance (EPR) experiments. Therefore, if one can combine the sensitivity of EPR with the element specificity of NMR, then a great deal of information about a NC very quickly. In a DNP experiment, a microwave field is first used to polarize an electron radical impregnated within the sample of interest. This polarization is then transferred to a nearby proton, followed by the nucleus of interest. Analogous to the increase in S/N obtained by using CP-MAS, DNP experiments can increase signal by 50,000 times due to the high Larmor frequency of an electron.[50]

The significant improvements in S/N attained through DNP-NMR mean that experiments that would normally take weeks can now be accomplished in hours. Rossini and coworkers recently used DNP to investigate the surface of Cd treated InP QDs.[51] DNP enhanced 2D $^{31}P\{^{113}Cd\}$ D-HMQC experiments were performed in 16 hours rather than 3 weeks. The results showed that postsynthetic Cd treatment causes Cd incorporation into the surface lattice of the QD as well as Cd carboxylate groups binding to surface P sites. Rossini has also followed up on the Strouse group's earlier CdSe studies by using DNP.[52] The sensitivity enhancement of DNP allowed for experiments including 2D ^{113}Cd-^{113}Cd, ^{77}Se-^{77}Se, and ^{113}Cd-^{77}Se to be conducted to further elucidate the nature of nanocrystal's surface in both spherical and platelet morphologies. Such experiments show the power of SSNMR over X-ray diffraction for NC crystallography.

CHAPTER 2

EXAMINING FREE CARRIER EFFECTS IN PLASMONIC TIN DOPED INDIUM OXIDE (ITO) NANOCRYSTALS

2.1 Introduction

A growing interest in plasmonic semiconductor nanocrystals (PSNCs) generated by aliovalent doping of wide band gap semiconductors has appeared due to the observation that the LSPR frequency and extinction are directly dependent on the carrier density at the Fermi level.[31,37,38,40,53–56] In PSNCs, the LSPR extinction feature arises from the coherent oscillation of carriers introduced at the Fermi level by carrier delocalization into the valence (p-type) or conduction (n-type) band upon doping. LSPRs are well known in coinage metals where the carriers are treated as a Fermi gas and an extinction feature in the visible regime is observed that is dampened by electron-electron and electron-phonon interactions.[20,21,32,35,36,57–59] The observed frequency is attributed to the interference of the real and imaginary terms of the dielectric function. In PSNCs, the LSPR feature is highly tunable but occurs in the infrared instead of the visible due to their lower carrier density when compared to metals such as Au and Ag.[26,31,53,60]

The incorporation of n and p-type dopants into semiconductors results in changes to the Fermi level and should produce changes in the UV-Vis (band edge) and NMR features that scale with carrier density. A shift in the band edge absorption has been observed in degenerately doped n and p-type semiconductors and should appear in aliovalent doped metal oxides that exhibit a LSPR. The absorption shift arises from the non-zero occupancy of states at the conduction band minimum that scales with carrier density, which results in a change to the energy required to excite an electron from the valence band into the conduction band.[61,62] The change in energy can be fit to the Burstein-Moss expression and the shift in the optical band gap is treated as a

Coulombic repulsion term renormalizing the band gap.[63–66] In terms of NMR, free carriers can induce changes to the nuclear relaxation rates (T_1 and T_2) due to paramagnetic relaxation enhancement, as well as shift the NMR resonance by altering the local electric shielding due to an induced metallic character of the observed nuclei.[67,68]

Optical methods are convenient for carrier analysis within a sample; however, such methods require approximations to extract actual carrier density. The LSPR shift with carrier density has been shown to be adequately fit by the Drude-Lorentz model for ITO NCs at <10% donor incorporation.[28,60] Although the LSPR fit follows the square root of dopant concentration, as expected from the Drude-Lorentz model, recent studies have questioned whether the extraction of carrier densities from the model is accurate.[69,70] Millstone and coworkers reported that the carrier densities extracted from the Drude model were inconsistent with ^{77}Se solid-state nuclear magnetic resonance (ssNMR) analysis of a Knight shift and decreasing T_1 relaxation rates in vacancy doped $Cu_{2-x}Se$.[70–72] Beaulac and coworkers suggested in InN that chemical titration is necessary to accurately measure the carrier densities in PSNCs.[69] Although correlations between each method and carrier densities have been observed, accurately measuring carrier densities using chemical titrations can allow for direct correlation of the physical properties observed by carrier induced band edge shift, LSPR changes and NMR effects. Comparison of the change in the LSPR[25,53,73] and the shift in the band gap absorption edge[61,64,66] as a function of the actual carrier density may allow the incorporation of a correction factor in analogy to the use of a dampening term (Γ) to explain the size dependent plasmon response in gold.[35] By comparing the chemically measured carrier density to observed plasmon frequency, band edge energy, and NMR properties, a correlated picture of the physical property changes that occur with increasing dopant concentration can be evaluated.

In this chapter, the electronic and nuclear perturbations that arise from changes in the Fermi level upon incorporating an aliovalent ion into a semiconductor lattice are evaluated in spherical, oleic acid passivated, $Sn_xIn_{2-x}O_3$ (ITO, 5 ± 0.5 nm). The carrier density, as measured by chemical titration with a one-electron oxidant, is compared to the observed spectral shifts in the NIR LSPR, the absorption edge in the UV-Vis, and the ^{119}Sn NMR resonance. Analysis of the LSPR shift using the Drude model and the absorption band edge shift via the Burstein-Moss relationship reveal that while the anticipated relationships with carrier density are observed for the optical features, both models either underpredict the carrier density or require a correction term to be quantitative. A linear dependence of the ^{119}Sn linewidth and Knight shift on carrier density is observed in the ^{119}Sn NMR spectra. The small Knight shift (<10 ppm) most likely reflects the band structure lacking Sn s-orbital contributions in the conduction band. The observed linear dependence on the NMR linewidth for the ^{119}Sn features with carrier density indicates that T_2 relaxation is enhanced with increased carrier density. This behavior is anticipated in n-type ITO NCs, confirming the chemical titration values are valid. Although T_1 is also an important relaxation pathway, T_1 is observed to be too long to be directly measured for the Sn:In_2O_3. The experimental observations are consistent with the expectation that when Sn(IV) is doped into In_2O_3, the presence of carriers at the Fermi level will impact the optical spectra and nuclear spin relaxation rate due to paramagnetic enhancement.

This study allows a direct correlation of carrier density measured by chemical titration with the observed changes in the optical and NMR spectral response to increasing carrier density in ITO NCs and illustrates the power of ssNMR to act as a local probe in plasmonic systems providing deeper insight into structure and carrier relaxation pathways. The study extends the use of ssNMR probe methods to analyze commercially relevant ITO NCs is an important step to developing a full understanding of the plasmonic behavior outside of the confinement limit and the role of T_2 on carrier relaxation in an n-type semiconductor induced by aliovalent doping. Developing probe techniques that measure carrier density and carrier relaxation rates is important for the continued development of electrochromic windows,[73,74] photocatalysis,[75,76] and biomedical treatments.[77,78]

2.2 Experimental Methods

2.2.1 Synthesis of ITO Nanocrystals

ITO NCs of various doping concentrations were synthesized as previously reported by Hutchison and coworkers.[79] Metal oleate precursors are formed in oleic acid under N_2 and then added dropwise at a rate of 0.2 mL/min to 12.5 mL of oleyl alcohol kept at 230 °C while N_2 is continuously run over the reaction. After the injection was completed, the solution was kept at 230 °C for an additional 20 minutes, followed by cooling to room temperature and isolation/cleanup of the NCs using toluene/acetone (3x) and centrifugation.

2.2.2 General Characterization

Inductively Coupled Plasma-Mass Spectrometry (ICP-MS) was performed using a Thermo Scientific iCAP RQ ICP-MS to confirm the ratio of Sn:In in the NCs. Samples were digested in concentrated nitric acid and then diluted to 2% HNO_3. Calibration curves were prepared from serial dilutions of a Sn/In standard dissolved in 2% nitric acid with R^2 values >0.999 for both ions. Each sample was measured in triplicate after an initial survey run and there was a minimum 30 second wash time between samples.

Powder X-ray diffraction (pXRD) patterns were collected with a Rigaku MiniFlex powder X-ray diffractometer using a Cu-Kα X-ray source. Samples were dried out and crushed into a fine powder and then loaded onto a zero-background micropowder plate. Scans were collected from 15-80° 2ϴ at a rate of 5°/min and a 0.1° step size. Whole powder pattern fitting and the Halden-Wagner method for Scherrer analysis were completed using the Rigaku SmartLab Studio software and performed for all samples to confirm the average NC size.

Nanocrystal samples were diluted and suspended in chloroform and then dropcast onto Formvar-coated copper TEM grids (Ted Pella) and allowed to dry in a desiccator overnight. Experiments were performed at the National High Magnetic Field Laboratory using a JEM-ARM200cF electron microscope operating at 200 kV.

Purified ITO NCs were suspended in tetrachloroethylene. UV-Vis-NIR data was collected using a Perkin Elmer Lambda 950 Spectrophotometer. A 1 cm pathlength NIR Quartz cuvette (Spectrocell) was used for all absorption experiments. Spectra were baseline corrected using neat tetrachloroethylene and normalized to the band edge absorption of the ITO NCs.

2.2.3 Optical Titrations

The one electron oxidation of the ITO NCs was adapted from ref. 20. A known concentration of purified ITO NCs was suspended in dry tetrachloroethylene and brought into an inert atmosphere glovebox. A known concentration of $NOBF_4$ in MeCN was titrated into the ITO suspension and left to oxidize for 30 minutes. The sample was then loaded into a Pike Technologies Liquid FTIR cell with BaF_2 windows and a pathlength of 0.5 mm. FTIR measurements were performed in transmission mode using a Jasco 6800 FTIR spectrometer. This procedure was repeated until the LSPR absorbance did not decrease upon oxidation. The absorbance at each titration point was integrated to account for changes in the shape of the LSPR. The linear region of the titration was then extrapolated to determine the amount of $NOBF_4$ theoretically required to completely extract all free carriers. This number was then converted to the carrier density of the ITO NCs by dividing the extracted number of electrons by the volume of NCs in the suspension calculated using the density of indium oxide and the size of the NCs.

2.2.4 NMR Spectroscopy

Solution ^{19}F NMR was performed using a 400 MHz Bruker AVIII spectrometer. The concentration of the $NOBF_4$ in MeCN solution was determined using a known concentration of 1, 2, 4, 5-tetrafluorobenzene as an internal standard and by measuring the ratio of the integrated $NOBF_4$ feature to the tetrafluorobenzene signal.

SSNMR spectroscopy was performed on dried nanocrystals crushed into a fine powder and packed into a 4 mm zirconia rotor. A 500 MHz Bruker AVIII HD Wide Bore spectrometer was used for all measurements. Spectra were collected using a standard spin-echo pulse sequence with a pulse width of 6.4 μs, an acquisition time of 5.5 ms, and 24,576 scans for each sample at the ^{119}Sn Larmor frequency 186.49 MHz. The chemical shifts were referenced to solid SnO powder at -206 ppm. Magic angle spinning was used for all samples at a rate of 10 kHz.

2.3 Results and Discussion

A series of oleic acid passivated 5.0 $\pm$ 0.5 nm $Sn_xIn_{2-x}O_3$ (ITO) (x = 0.020, 0.031, 0.040, 0.050, 0.063, and 0.073) NCs were prepared following the synthetic protocol of Hutchison and coworkers.[79] The Sn concentrations were verified by inductively coupled plasma-mass spectrometry (ICP-MS). Powder X-ray diffraction (pXRD) allows assignment of all samples to the bcc bixbyite phase (PDF #03-065-3170) (Figure 10). There are no discernible pXRD shifts in the diffraction peaks and calculations of the lattice parameter for each sample showed little to no change, owing to the similarity in size of the In(III) and Sn(IV) ions ($r_{In(III)}$ = 81 pm, $r_{Sn(IV)}$ 71

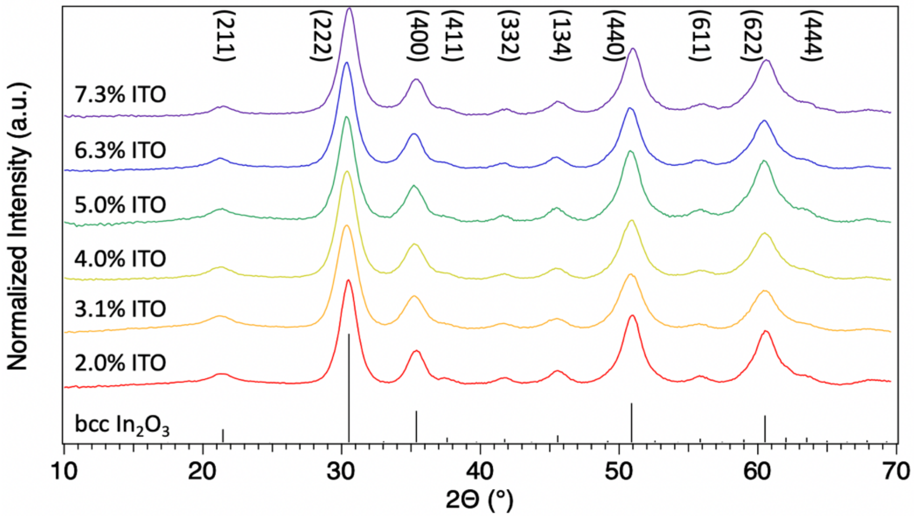

Figure 10. pXRD of 2.0-7.3% ITO NCs indexed to the bcc-bixbyite In_2O_3 phase

pm).[80] Scherrer analysis of the calculated using all diffraction lines using whole powder pattern fitting is provided in Table 1. Figure 11 shows a representative TEM image of the ITO NCs, a high magnification image showing the lattice planes, and the corresponding size distribution of the nanoparticles.

Table 1. Scherrer, Drude, and $NOBF_4$ titration analysis of X% ITO NCs

[Sn]	2.0%	3.1%	4.0%	5.0%	6.3%	7.3%
Size (nm)	5.1(2)	4.7(3)	4.4(2)	5.0(3)	4.6(2)	4.7(3)
Drude Carrier Density/10^{18} (cm^{-3})	495.59	537.46	591.47	613.12	633.88	703.98
$NOBF_4$ Carrier Density/10^{18} (cm^{-3})	412.58	597.95	833.38	1037.96	1261.85	1458.42
Drude Γ (cm^{-1})	1849.17	2660.98	3127.25	3397.95	3607.15	3712.40

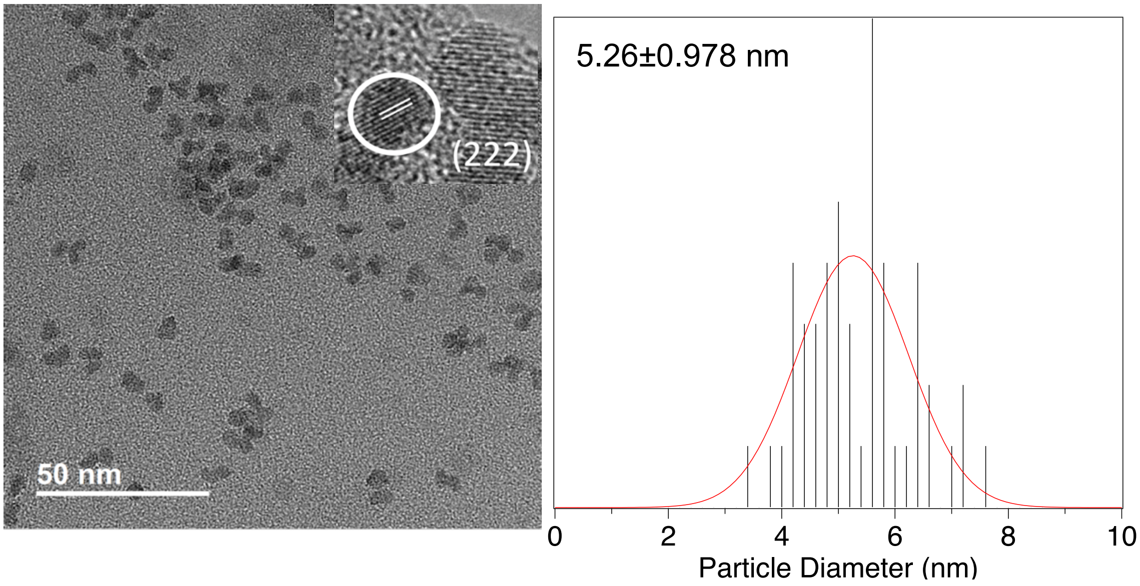

Figure 11. TEM image and corresponding histogram of 7.3% ITO NCs

2.3.1 Free Carrier Density in ITO

The carrier density of the prepared ITO samples in this study was quantified by chemical titration with NOBF$_4$, a one-electron oxidant. The use of NOBF$_4$ to evaluate carriers was previously reported for InN by Beaulac and coworkers.[69] In Figure 12, a plot is shown of the carrier concentration determined via chemical titration vs. % Sn incorporation into In$_2$O$_3$ measured by ICP-MS. The linear relationship confirms that dopant concentration is directly proportional to the carrier density of the ITO NCs within this regime (2.0-7.3%). The dependence of carrier density on Sn(IV) doping is consistent with earlier studies suggesting the Sn(IV) incorporation into In$_2$O$_3$ is stochastic across the entire nanocrystal volume and exhibits equivalent dopant activation within this doping range based on the LSPR shift.

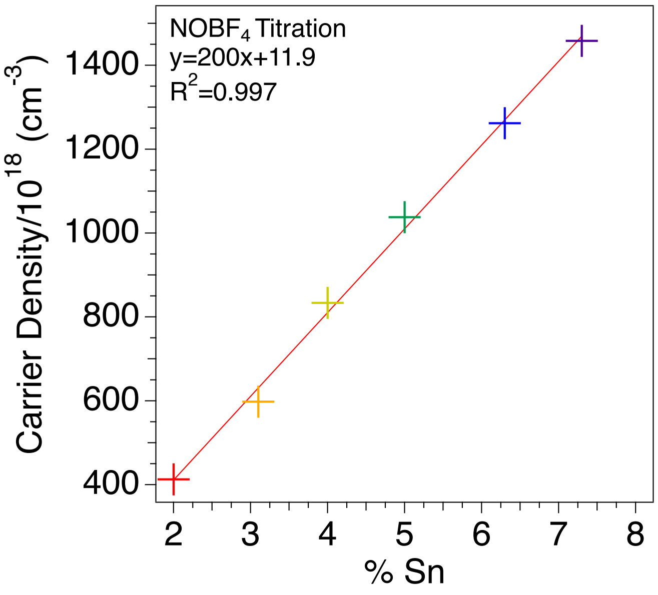

Figure 12. Carrier density determined by one electron oxidant NOBF4 titrations for 2.0-7.3% ITO NCs

Evaluation of the plot reveals the carrier density ranges from 0.4 to 1.4 x 10^{21} cm^{-3} or 27 to 95 electrons per NC. It is expected that one free carrier will be generated per Sn dopant incorporated into In_2O_3, but the measured carrier density values indicate that only 0.65 free carriers are generated per Sn dopant. The observed 35% dopant deactivation is attributed to compensating defect complexes within the NC arising from inherent oxygen vacancies within the bixbyite crystal structure that produces oxygen interstitial complexes of the form $2Sn_{In}^{\bullet} - O_i''$.[81,82] It is worth noting the titration experiment is in excellent agreement with the previously reported <70% dopant activation in ITO NCs.[82] Such deactivation may also arise from the existence of a surface depletion region where surface defects result in decreased free carrier generation.[83] Further evaluation allows the intrinsic carrier density to be established in the ITO samples. Native carriers in the undoped In_2O_3 NCs are expected to be present due to inherent oxygen vacancies.[81,82] From the chemical titration plot, the intrinsic carrier density can be estimated by extrapolating the plot to 0% Sn, yielding a value of 1.2 x 10^{19} cm^{-3} or 0.78 intrinsic carriers per NC from native defects in the ITO samples.

2.3.2 Carrier Induced LSPR Shift

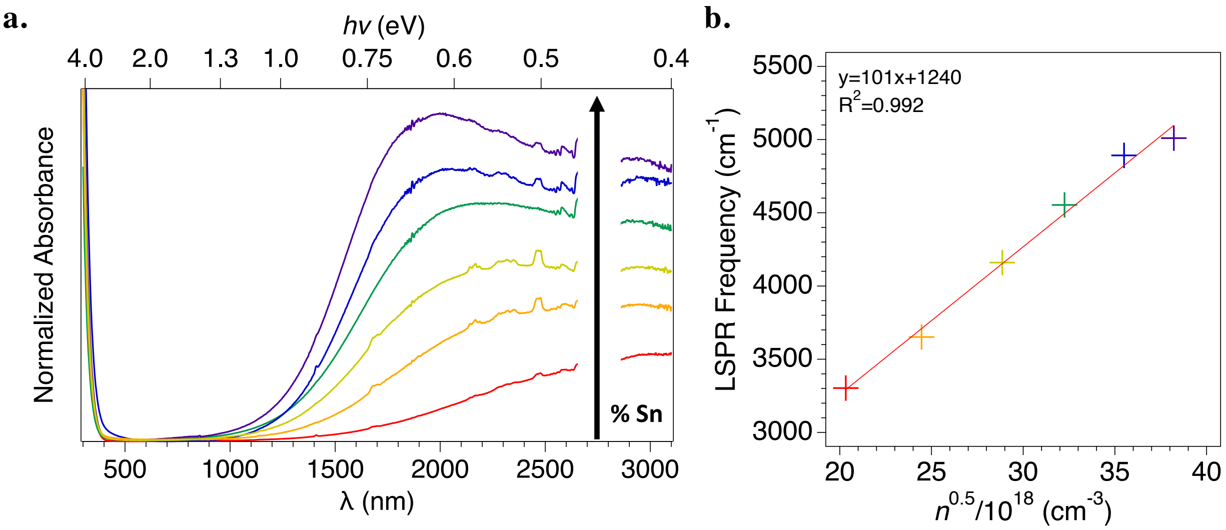

Figure 13. (a.) UV-Vis-NIR of ITO NCs with increasing % Sn. Data from 2700-2850 nm has been removed for visual clarity (b.) Square root of carrier density measured via NOBF4 titration vs. LSPR frequency

In Figure 13, the LSPR extinction feature, as measured using UV-Vis-NIR, is observed to shift to higher frequency with increasing Sn concentration. Since LSPRs are inherently interfacial and dielectric phenomena, the Drude-Lorentz free electron model is typically used to model their absorbance to extract useful information.[28,63,84]

$$\varepsilon(\omega) = \varepsilon_\infty + \varepsilon_{BG}(\omega) + \varepsilon_{UV}(\omega) + \varepsilon_{Vis}(\omega) + \varepsilon_D(\omega) \qquad (7)$$

$$\varepsilon_D(\omega) = -\frac{\omega_p^2}{\omega^2 + i\omega\Gamma} \qquad (8)$$

$$\omega_p = \sqrt{\frac{ne^2}{m^*\varepsilon_0}} \qquad (2)$$

Eqn. 7 represents the sum of dielectric contributions including the high frequency dielectric constant (ε_∞) and the background, UV, visible, and Drude terms respectively. The Drude contribution is responsible for the LSPR absorption feature and can be described using the plasma frequency (ω_p) and a dampening term (Γ). ω_p can be further broken down as shown in eqn. 8, where n is the free carrier density, e is the charge of the free carrier, m^* is the effective mass of the carrier, and ε_0 is the permittivity of free space. It is worth noting that the experimentally measured LSPR frequency of a nanocrystalline sample (ω_{LSPR}) can be described as by the following eqn.[84]

$$\omega_{LSPR} = \frac{\omega_p}{\sqrt{\varepsilon_\infty + 2}} \tag{3}$$

$\varepsilon_\infty = 4.08$ for In_2O_3,[34] therefore the observed LSPR will appear at ~2.45 times lower frequency than the calculated ω_p.

From eqns. 1-4, the value of ω_p, and therefore ω_{LSPR} will be directly proportional to the square root of n. A plot of the LSPR shift as a function of the square root of carrier concentration extracted from the chemical titration is shown in Figure 13b. The values for ω_{LSPR} were determined via Drude modeling of the absorption data using Matlab code written by the Milliron group.[28] The linear dependence of the LSPR frequency with the square root of carriers is consistent with earlier findings,[85] however, extraction of the carrier densities from LSPR data using the Drude model is inconsistent with values obtained from chemical titration (Figure 3a). The linear relationship confirms the LSPR shift is due to free carriers, but the difference in carrier density requires a correction factor of $\gamma = 0.18$. This suggests the Drude-Lorentz model underestimates the carrier densities by nearly 20% most likely due to an additional dampening term being required, analogous to Drude-Lorentz analysis of metallic plasmonic systems.

Such a correction term for PSNCs has been previously proposed by Jung and Pedersen[84] to account for large deviations in the calculated ω_p for ZnO when using a simple effective mass approach compared to the full band structure calculations. They proposed an advanced effective mass model of ω_p, which contained a correction term to eqn. 2 to account for the deviation.

$$\omega_p^2 = \frac{e^2 n}{\varepsilon_0 m^*}\frac{1}{\sqrt{1+(9\pi^2 n)^{2/3}\hbar^2/(m^*\alpha)}} \qquad (9)$$

In this eqn., α is the correction factor that accounts for the change in local band shape as the Fermi level moves further into the conduction band with increases n-type doping.

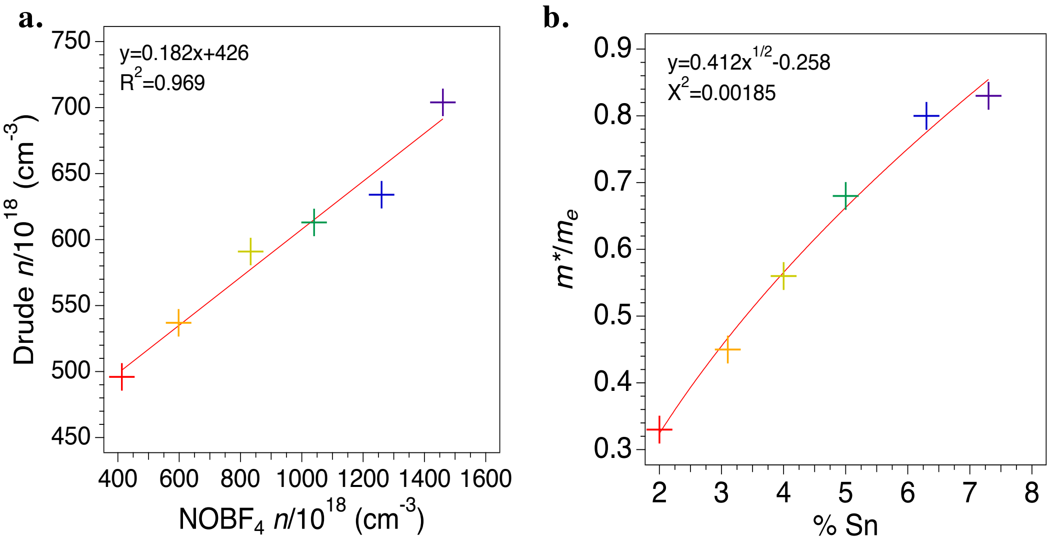

Figure 14. (a.) Carrier density determined by one electron oxidant NOBF$_4$ titrations for 2.0-7.3% ITO NCs (b.) m^* values for each ITO sample calculated using the Drude model and chemical titration determined carrier densities

To evaluate the model of Jung and Pederson for the ITO samples, the effective mass of the free carriers for each ITO sample is extracted from the LSPR data using the Drude model (Figure 14). This plot shows that the value for m^* varies substantially with Sn loading, ranging from 0.33*m_e at low doping levels to 0.83*m_e (where m_e is the mass of an electron) at higher concentrations. The unexpected variance is in disagreement with prior results from ITO thin films and cyclotron resonance measurements on ITO NCs that confirm m^* values are 0.4*m_e at low doping levels.[33,55,86] By combining the values of ω_p extracted from optical measurements, n measured via NOBF$_4$ titrations, and the literature value of m^* for ITO (0.4*m_e), the Jung-Pederson model (eqn. 9) can be used to calculate a suitable correction factor (α) for each sample.

These results are illustrated in Figure 15 and show that different correction factors were required to model the experimental results. The high carrier density samples (6.3%, 7.3% ITO) show that α converges to a value of 1.48 eV, while lower carrier density samples approach the simple effective mass calculation (i.e. no correction factor). The modeling for the 2.0% ITO is omitted from Figure 15 due to this convergence with the simple effective mass model.

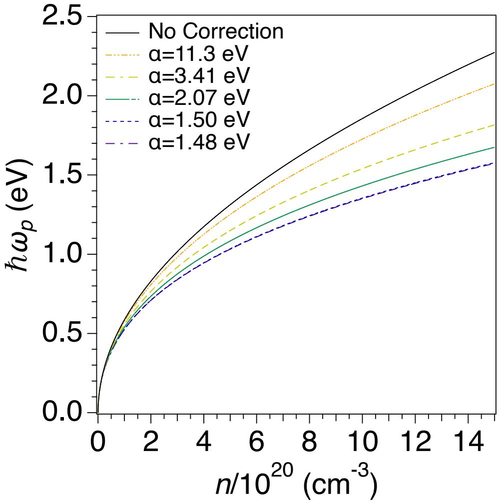

Figure 15. Dirac effective mass modeling of 3.1-7.3% ITO NCs (dashed lines) and simple effective mass model (solid line)

The high carrier density limit of 1.48 eV is notable as it agrees well with the value of 1.52 eV calculated by Jung and Pedersen for n-type ZnO.[84] However, one would expect a consistent value of α for all samples if free carrier concentration were the only variable. The shift from the uncorrected Drude model to the convergence of high carrier density samples at 1.48 eV for the advanced effective mass model indicates that there are more variables involved in this process than just carrier density. When the Fermi level lies close to the conduction band minimum, m^* is equal to the known value of $0.4{*}m_e$ and the uncorrected Drude model can effectively explain the optical data. Once the Fermi level passes deep enough into the conduction band, as is the case for the samples with high carrier densities, the value for α ceases to change and the advanced effective mass model can accurately describe the change in parabolicity of the band structure with a constant m^* of $0.4*m_e$.

2.3.3 Carrier Induced Burstein-Moss Shift

A Burstein-Moss (B-M) shift is often observed in degenerately doped semiconductors. This shift has not been widely considered for PSNCs; however, it is anticipated that a B-M shift of the absorption edge will occur in the ITO samples due to the shift in the Fermi level relative to the valence band maximum with increasing n-type dopants.[61,62] B-M shifts for thin film ITO have been reported to be proportional to the carrier density, and can be fit to the B-M expression,

$$\Delta E_{abs} = E_g^{Sn} - E_g^0 = \left(\frac{\hbar^2}{2m^*}\right)(3\pi^2 n)^{2/3} \qquad (10)$$

where E_g^{Sn} is the measured bandgap as a function of % Sn and E_g^0 is the native bandgap at the intercept when % Sn = 0, and n/m^* remain the carrier density and effective mass of the free carrier respectively.[64,66] The B-M expression can be used to analyze the relative change in carrier density with Sn doping and can also be used to extract an average value of m^* for the series of ITO NCs.

In Figure 16a, the band edge shift with increasing Sn incorporation is plotted in the form of a Tauc plot. In a Tauc plot, the product of the absorbance and energy of light raised to $1/r$ $[(\alpha h\nu)^{1/r}]$ is plotted against $h\nu$.[87] A value of r = 1/2 is used for a direct band gap semiconductor like ITO, where the interband absorption is allowed.[87] The value of E_g is obtained by extrapolating the linear region of the plot. Plotting E_g vs. $n^{2/3}$ (Figure 16b) shows the expected linear correlation predicted by the B-M shift. As observed in Figure 16b, the shift in E_g with increasing carrier density for each ITO sample follows the anticipated 2/3 power law with a y-

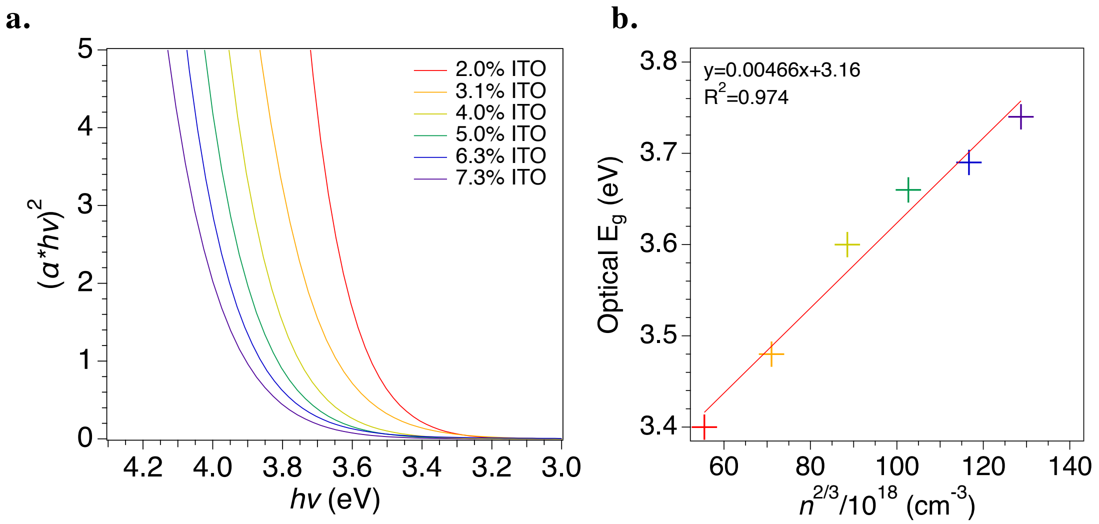

Figure 16. (a.) Direct band gap Tauc plot of 2.0-7.3% ITO NCs (b.) Plot of the optical bandgap vs. chemical titration measured carrier density raised to the 2/3 power

intercept value of $E_g^0 = 3.16$ eV. This 2/3 power law behavior with increasing carrier density is consistent with previous literature reports for ITO thin films[65,88,89] and is due to the parabolic nature of the conduction band minimum in In_2O_3. The average m^* for the ITO NCs can be determined using eqn. 10 and the slope extracted from the linear fitting in Figure 16b. This leads to a value of $0.78{*}m_e$, which is inconsistent with the expected value for ITO. The overestimation of m^* by parabolic band theory confirms the analysis via the Drude model showing that a loss of parabolicity in the band structure is likely occurring as the Fermi level moves further from the conduction band minimum. Analogous to extracting m^* using the standard Drude model, a correction factor is needed to accurately determine m^* of a system using the Burstein-Moss shift. For 5 nm ITO NCs, this leads to a value for the correction term (defined here as Ω) being equal to 0.51.

2.3.4 Free Carrier Effects on Nuclear Relaxation Pathways

The extrapolation of early efforts to correlate Knight shift and changes in T_1 with carrier density by Schmidt-Rohr in $Ag_{1-y}Pb_{18}Sb_{1+z}Te_{20}$[72] and more recently by Millstone in $Cu_{2-x}Se$[70]

suggests ssNMR methods are more effective for understanding carrier behavior. To evaluate the possible discrepancy in the optical methods in ITO NCs, ^{119}Sn magic angle spinning (MAS) ssNMR measurements were performed on the powdered samples of the ITO NCs. For these studies, samples were packed into a 4 mm zirconia rotor and spun at the magic angle at 10 kHz. The ^{119}Sn experimental data was collected using a spin-echo pulse sequence. The choice of measuring ^{119}Sn rather than ^{115}In is due to ^{119}Sn being a dipolar nucleus and because the low concentration of ^{119}Sn leads to the elimination of dipolar-dipolar coupling. ssNMR also has the advantage over optical methods in that the participation of deactivated (pinned carriers) can be directly probed by inspection of the observed NMR features.[90,91]

The ^{119}Sn spin-echo MAS NMR spectra for the ITO series is presented in Figure 17a. The feature between -500 and -600 ppm is assigned to a six-coordinate Sn(IV) center. As % Sn increases, the assigned feature is observed to increase in intensity, shift slightly downfield (higher ppm), and broaden. It is worth noting that additional structure in the SSNMR spectrum reflects contributions that scale inversely with % Sn and arise from noise and the probe feedback that are observable due to poor S/N associated with the low concentration and natural abundance (8.6%)[90] of Sn dopant. The overall intensity of the ^{119}Sn feature increases linearly with % Sn (Figure 17b), as expected since S/N is directly proportional to the number of nuclear spins present in the sample.[68] Many factors can influence the total integrated area of a SSNMR spectrum, therefore comparing the integrated areas is often unreliable when compared to using this method for solution NMR. This analysis serves only to further demonstrate the ICP-MS confirmed trend of increasing % Sn in the PSNCs.

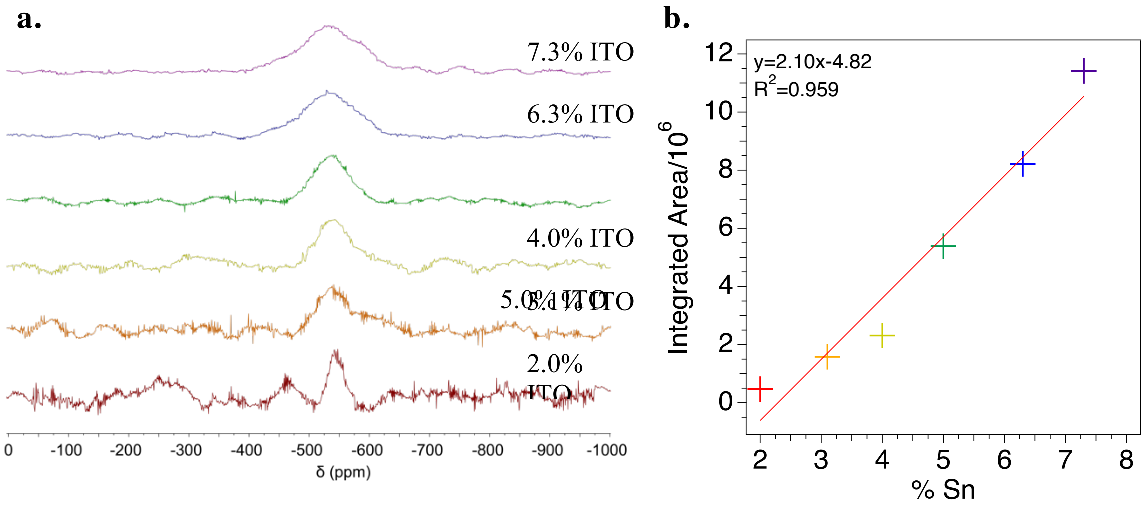

Figure 17. (a.) ^{119}Sn MAS SSNMR spectra of X% ITO NCs. Data was collected using a spin-echo pulse sequence on a Bruker WB 500 MHz SSNMR spectrometer. Peak intensities are normalized for visual clarity (b.) Absolute integrated areas of the ^{119}Sn feature for 2.0-7.3% ITO NCs

The observed linear downfield shift (Figure 18a) and change in the full width at half maximum (FWHM) (Figure 18b) of the ^{119}Sn feature as a function of Sn(IV) concentration can be understood by considering each Sn(IV) incorporation leads to a carrier at the Fermi level interacting with the ^{119}Sn nuclear spin, allowing assignments of the change in chemical shift as a Knight shift and the increase in linewidth to Knight shift anisotropy (KSA).[68,92] The Knight shift occurs due to free electron-nuclear spin interactions resulting in the observed concentration dependent shift since $\delta_{obs} = \delta_{CS} + \delta_{KS}$. The values δ_{obs}, δ_{CS}, δ_{KS} are the observed chemical shift, chemical shift without paramagnetic influence, and the Knight shift contribution respectively. While the shift is small and potentially within instrumental error, the positive sign of the Knight shift indicates that this interaction occurs through a delocalization mechanism,[68] which would be the expected result for electron-nuclear interactions stemming from free carriers residing in the conduction band. The results support the idea that in ITO NCs the Knight shift and KSA changes are directly proportional with Sn concentration, which is consistent with attributing the behavior to the free carrier population at the Fermi level in these PSNCs.[68,93]

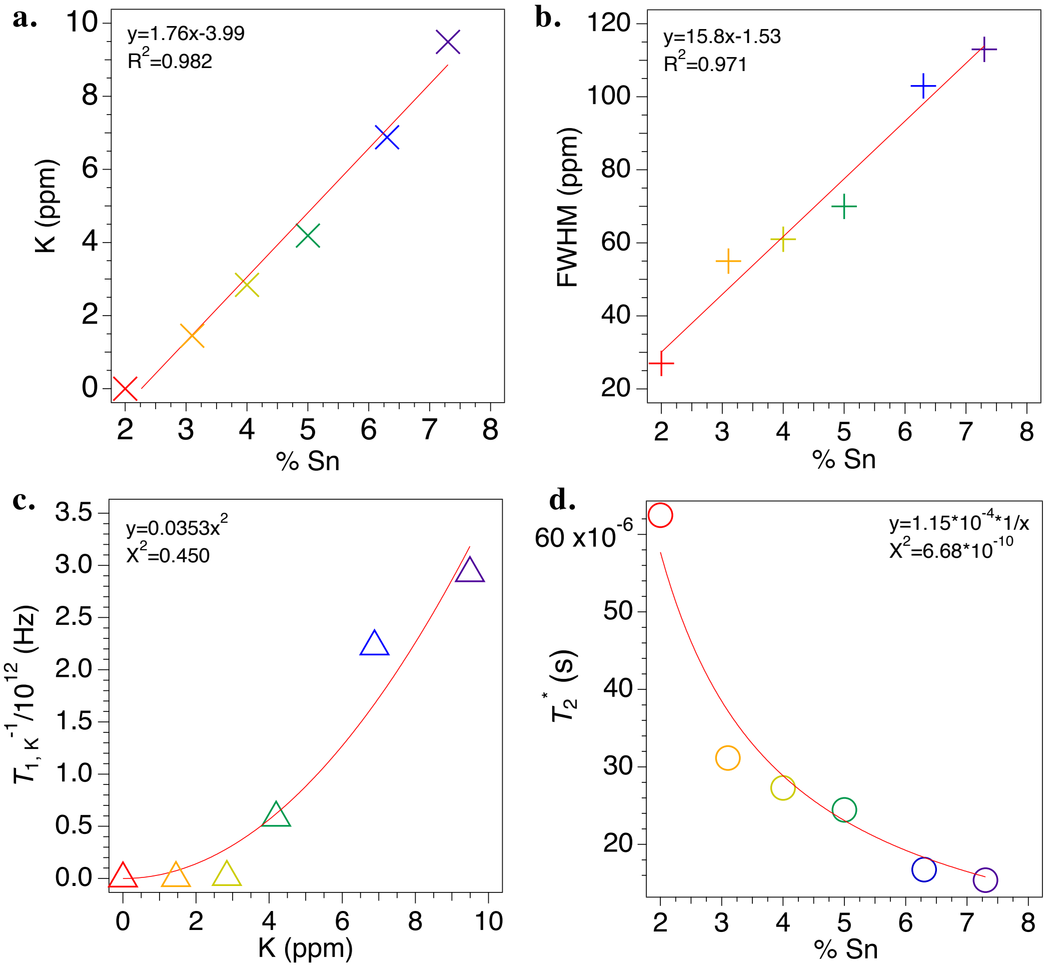

Figure 18. (a) Knight Shift of ITO NCs as a function of % Sn (b) Change in FWHM as a function of % Sn (c) Knight-Korringa relation estimating the change in T_1 as a function of the Knight shift (d) Effect of % Sn on T_2^*

In addition to the observed Knight shift and KSA effects induced by free carriers, changes in the T_1 (spin-lattice) and T_2 (spin-spin) relaxation pathways for the Sn(IV) nuclei are anticipated.[70–72] T_1 is related to the Knight shift, while T_2 can be correlated with KSA. It is expected that as the n-type carrier density in ITO NCs increases with increasing % Sn, the T_1 and T_2 will decrease because of paramagnetic relaxation enhancement by the free electrons.

However, direct measurements of the T_1 and T_2 of ^{119}Sn are challenging in ITO NCs. T_1 measurements are difficult due to the long T_1 of ^{119}Sn, coupled with the lengthy acquisition times required to obtain suitable spectra at low % Sn. Conversely, the T_2 relaxation rates of these samples are too short to conduct cross-polarization (CP-MAS) or Carr-Purcell-Meiboom-Gill (CPMG)[47,48] experiments.

An estimate for the change in T_1 can be obtained from the observed Knight shift (K) through the Knight-Korringa relationship[24,94]

$$T_{1,K}^{-1}(K,T) = \left(\frac{\gamma_n}{\gamma_e}\right)\frac{4\pi k_B T}{\hbar}K^2 \tag{11}$$

where γ_n and γ_e are the gyromagnetic ratios of the nuclear and electronic spins, k_B is the Boltzmann constant, T is the absolute temperature, and $T_{1,\mathrm{K}}$ is the Korringa contribution to the spin-lattice relaxation. The observed spin-lattice relaxation, $T_{1,\mathrm{K}}^{-1}$(K,T), is a result of the sum of contributions from the paramagnetic relaxation enhancement $T_{1,}^{-1}$(K, T) and the temperature and Knight shift independent $T_{1,0}^{-1}$. The relationship will hold for a metallic system, which is consistent with the Fermi carrier density present in a n-type PSNC. A plot of the Knight shift vs. the calculated change in $T_{1,\mathrm{K}}^{-1}$(K,T) is shown in Figure 18c. The experimental data follows the predicted K^2 dependence for the Knight-Korringa relationship confirming T_1 is shortened as carrier density increases in ITO. While the shortening of the calculated T_1 agrees with the trend seen for $Cu_{2-x}Se$, a p-type PSNC,[70] the magnitude of $T_{1,\mathrm{K}}$ for the n-type ITO nanocrystals in this study is small. The small magnitude is believed to be due to the relatively long T_1 for Sn(IV), which has been shown to be between 15 and 80 seconds[95,96] compared to that of the ^{77}Se nucleus measured by Millstone on the order of ms. These results indicate that T_1 relaxation is not a good measure for carrier density for all PSNCs.

The T_2 relaxation is not directly measured, but T_2^* can be extracted by relating the linewidth of the NMR signal to T_2^*[97]

$$\Delta\nu_{FWHM} = \frac{1}{\pi T_2^*} \tag{12}$$

where $\Delta\nu_{FWHM}$ is the FWHM of the NMR signal measured in Hz. The value of T_2^* is related to T_2 by the following expression[98]

$$\frac{1}{T_2^*} = \frac{1}{T_2} + \gamma\Delta B_0 \tag{13}$$

where $\gamma\Delta B_0$ is the change in strength of the local magnetic field. Modern NMR spectrometers exhibit field inhomogeneities below 1 ppm, therefore for a typical solid-state NMR experiment the broadening of the signal is primarily due to chemical shift anisotropy, rendering any local changes in magnetic field negligible. This means that for these experiments, T_2 and T_2^* can be considered to be equivalent. In Figure 18d, a plot of T_2^* as a function of % Sn shows T_2^* is observed to decrease very rapidly at low % Sn levels and then taper off at higher doping concentrations. The extracted value of T_2^* is very short in these systems, owing to the large number of free carriers present in n-type ITO NCs. Consistent with a short T_2^*, measurement of T_2 using CPMG pulse sequences were not successful. This short transverse relaxation rate for 2.0% and 7.3% ITO samples was insufficient to produce a suitable echo train and produced no discernable signal.

For ITO, the Knight-Korringa relation shows little change with increasing free carrier concentration due to the nature of the ^{119}Sn isotope. The change in linewidth due to KSA effects for these samples (from ~30-115 ppm) is much greater than the resulting Knight shift (~10ppm). This signifies that T_2 is a more sensitive probe for carrier density than T_1 for plasmonic ITO NCs. Overall, the observed decrease in T_2 with increasing % Sn confirms the role of carriers at the Fermi level in ITO.

2.4 Conclusions

ITO NCs from 2.0-7.3% Sn were synthesized and fully characterized via UV-Vis-NIR, FTIR, pXRD, ICP-MS, TEM, and by chemical titrations of the free carriers. Carrier density increases linearly with % Sn within this doping regime, as evidenced by the corresponding change in plasmon frequency and B-M shift. Based on the results of the chemical titrations, the Drude model underpredicts the carrier density and the number of carriers generated per incorporated dopant ion, while overpredicting the number of native free carriers in ITO. The B-M shift serves as an accurate predictor of changes in carrier density, but severely underestimates the number of free carriers needed to induce a band edge shift. Both the Drude and parabolic band theory models fail to predict accurate values for m^*, as they do not consider the non-parabolicity of the local band structure with respect to the Fermi level. This can be accounted for by using an advanced effective mass model to examine the LSPR and by applying a correction factor to the value for m^* obtained via B-M analysis. ^{119}Sn SSNMR experiments show that these PSNCs demonstrate linewidth broadening that is directly proportional to the carrier density of the NCs. A possible Knight shift exhibits the correct sign for a delocalization mechanism, as expected for free carriers present at the Fermi level. The magnitude of any Knight shift in these materials is far smaller than that of $Cu_{2-x}Se$.[70] This is likely due to the differences in electronic band structure between $Cu_{2-x}Se$ and ITO. The magnitude of a Knight shift is dictated by interaction of unpaired electrons with the nucleus, which can only occur in orbitals with s-character due to the non-zero probability of the electrons residing at the nucleus.[99] The valence band of $Cu_{2-x}Se$ contains strong contributions from the Se 4s orbitals, for which free holes can strongly interact with causing the large Knight shift.[100,101] The conduction band of ITO is composed mostly of In 5s, 5p, and 4d orbitals, therefore the free electrons have less interaction with any Sn(IV) orbitals.[102] The correlation of line broadening with free carrier concentration serves as a relative measure of carrier density, which is very useful for systems whose LSPR cannot be fully resolved or those that do not possess a LSPR.

CHAPTER 3

INVESTIGATING DOPANT DEACTIVATION IN PLASMONIC M^{3+} DOPED ZINC OXIDE NANOCRYSTALS

3.1 Introduction

PSNCs have become an increasingly important area of research due to their advantages over traditional metallic plasmonic systems that include tunable carrier density via doping, complete transparency in the visible region, and their ability to strongly absorb near and mid-infrared wavelengths.[6,103,104] These unique properties have led to applications in the fields of sensing,[105–107] electrochromics,[13,73,108] and catalysis.[75,109,110] For a typical plasmonic system, the plasma frequency (ω_p) is primarily determined by the total number of free carriers (n) and the effective mass (m^*) of these carriers, as illustrated by the Drude-Lorentz model.[28] For systems with the same concentration of aliovalent dopant ion, it is expected that the same number of free carriers would be generated. However, it has been shown in recent literature that as the dopant atom for ZnO changes down group III (Al^{3+} to In^{3+}), ω_p shifts to higher frequencies.[111,112] The origin of this phenomenon has not yet been thoroughly investigated, but this observation could be explained in two ways: 1) an increase in carrier density as the dopant changes from Al^{3+} to In^{3+} or 2) a decrease in the value of m^*. The change in the ionic radius of the dopant atom can lead to better size matching with Zn^{2+} and increased dopant activation (i.e. higher values of n). However, better size matching of the dopant and host lattice ions could result in increased carrier mobility and therefore a decrease in m^*.

While much of the PSNC research has focused on ITO,[10,12,113,114] studies on Al:ZnO reveal plasmonic behavior that is size, dopant, and reaction dependent.[60,111,115] n-type ZnO is an industrially important material as it has long been studied as a cheaper alternative to indium tin oxide (ITO) for transparent conducting oxide applications.[116–118] M:ZnO nanocrystals ($M=Al^{3+}$,

Ga^{3+}, or In^{3+}) exhibit a LSPR in the MIR region.[60,111] Such low frequency LSPRs make these materials important for applications such as surface-enhanced Raman[22,23] and thermal waste management.[41,119] The method developed by Hutchison and coworkers[79] for the controllable synthesis of metal oxide PSNCs has been modified by Gaspera and coworkers for ZnO based systems, allowing for a broader study of the group III dopant effects on the LSPR in ZnO.[112]

In this chapter, the influence of group III doping on the frequency, extinction, and linewidth of LSPRs are investigated for spherical, oleic acid passivated AZO, GZO, and IZO NCs using a combination of analytical methods. The effect of dopant incorporation on the crystal structure is investigated via Vegard analysis of powder X-ray data and correlated to the change in the observed LSPR. The simple and advanced effective mass Drude models are utilized to evaluate the measured MIR LSPR, while a one-electron oxidant chemical titration method is used as a direct measure of the total number of carriers for each sample. Utilizing this independent measurement of free carrier concentration allows for the Drude correction factor to be calculated for each sample and these values are compared to that obtained via full band structure calculations of n-ZnO. These results serve to highlight the importance of dopant activation and the various mechanisms through which deactivation occurs in plasmonic semiconductor NCs, which is critical towards the future rational design of these materials.

3.2 Experimental Methods

3.2.1 Synthesis of M:ZnO Nanocrystals (M=Al^{3+}, Ga^{3+}, In^{3+})

MZO NCs were synthesized using a modified method previously reported by Gaspera and coworkers.[112] X mmol of $Al(acac)_3$, $Ga(acac)_3$, or $In(OAc)_3$ were combined with 1-X mmol of $Zn(OAc)_2$ dihydrate and 2 mL of oleic acid. This mixture was degassed at 110 °C for one hour, followed by the addition of 1 mL of oleylamine and subsequent degassing for 10 min. The metal oleate precursors are then added dropwise at a rate of 0.3 mL/min to 12.5 mL of oleyl alcohol kept at 240 °C while N_2 is continuously run over the reaction. After the injection is complete, the solution was kept at 240 °C for an additional 20 minutes, followed by cooling to R.T. and isolation/cleanup of the NCs using toluene/ethanol (3x) and centrifugation.

3.2.2 General Characterization

ICP-MS was performed using a Thermo Scientific iCAP RQ ICP-MS to confirm the ratio of (Al, Ga, In):Zn in the NCs. Samples were digested in concentrated nitric acid and then diluted to 2% HNO_3. Calibration curves were prepared from serial dilutions of an Al/Ga/In/Zn standard dissolved in 2% nitric acid with R^2 values >0.995 for all ions. Each sample was measured in triplicate after an initial survey run and there was a minimum 30 second wash time between samples.

pXRD patterns were collected with a Rigaku MiniFlex powder X-ray diffractometer using a Cu-Kα. Samples were dried out and crushed into a fine powder and then loaded onto a zero-background micropowder plate. Scans were collected from 20-70° 2θ at a rate of 5°/min and a 0.1° step size. Whole powder pattern fitting and the Halder-Wagner method for Scherrer analysis were completed using the Rigaku SmartLab Studio software and performed for all NCs.

TEM measurements were collected on nanocrystal samples were diluted and suspended in hexanes and then dropcast onto Formvar-coated copper TEM grids (Ted Pella) and allowed to dry in a desiccator overnight. Experiments were performed at the Vanderbilt Institute of Nanoscale Science and Engineering using a FEI Tecnai Osiris electron microscope operating at 200 kV.

Purified MZO NCs were suspended in toluene and then diluted into tetrachloroethylene for UV-Vis-NIR experiments. Data was collected using a Perkin Elmer Lambda 950 Spectrophotometer. A 1 cm pathlength NIR Quartz cuvette from Spectrocell was used for all absorption experiments. Spectra were baseline corrected using neat tetrachloroethylene and normalized to the band edge absorption of the NCs.

FTIR measurements were performed on purified MZO NCs suspended in tetrachloroethylene and diluted to appropriate concentrations. Samples were then loaded into a Pike Technologies Liquid FTIR cell with BaF_2 windows and a pathlength of 0.5 mm. FTIR measurements were performed in transmission mode using a Jasco 6800 FTIR spectrometer. Ligand absorption features were removed using Jasco's Sectra Manager software and the spectra were smoothed using a Savitzky-Golay filter.

Solution ^{19}F NMR was performed using a 400 MHz Bruker AVIII spectrometer. The concentration of the $NOBF_4$ in MeCN solution was determined using a known concentration of 1, 2, 4, 5-tetrafluorobenzene as an internal standard and by measuring the ratio of the integrated $NOBF_4$ feature to the tetrafluorobenzene signal.

3.2.3 Optical Titrations

One electron chemical titrations were performed using a known concentration of purified MZO NCs was suspended in dry tetrachloroethylene and brought into an inert atmosphere glovebox. A known concentration of $NOBF_4$ in MeCN was titrated into the NC suspension and left to oxidize for 30 minutes. After this time, the LSPR was measured via transmission FTIR (described above) and then the liquid cell was returned to the glovebox. This procedure was repeated until the LSPR absorbance did not decrease upon oxidation. The absorbance at each titration point was integrated to account for changes in the shape of the LSPR. The linear region of the titration was then extrapolated to determine the amount of $NOBF_4$ theoretically required to completely extract all free carriers. This number was then converted to the carrier density of the NCs by dividing the extracted number of electrons by the volume of NCs in the suspension calculated using the density of zinc oxide and the size of the NCs.

3.3 Results and Discussion

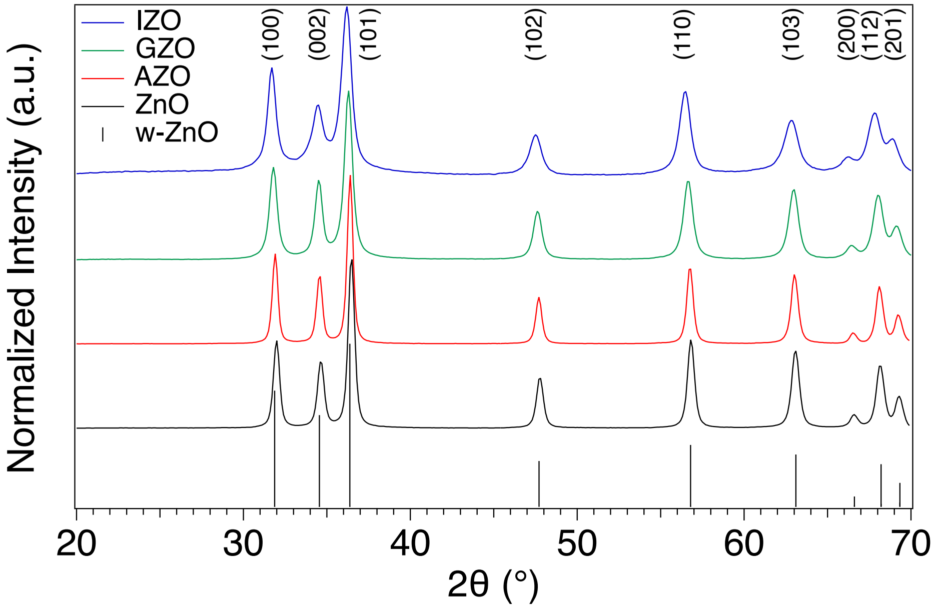

Figure 19. pXRD of ZnO and MZO NCs indexed to the wurtzite ZnO card (PDF #036-1451)

ZnO and MZO (M=Al^{3+}, Ga^{3+}, or In^{3+}) NCs were synthesized following the procedure of Gaspera and co-workers.[112] The MZO samples are ~10 nm in size and exhibit electron diffraction patterns assignable to a hexagonal lattice. The M:Zn incorporation into the MZO samples is 12%, as verified by ICP-MS. pXRD patterns (Figure 19) are assigned to the hexagonal wurtzite phase of ZnO (PDF #036-1451) and the sizes extracted by fitting the patterns via Scherrer analysis using whole powder pattern analysis corroborates the 10 nm size measured using TEM (Figure 20, Figure 21, Figure 22).

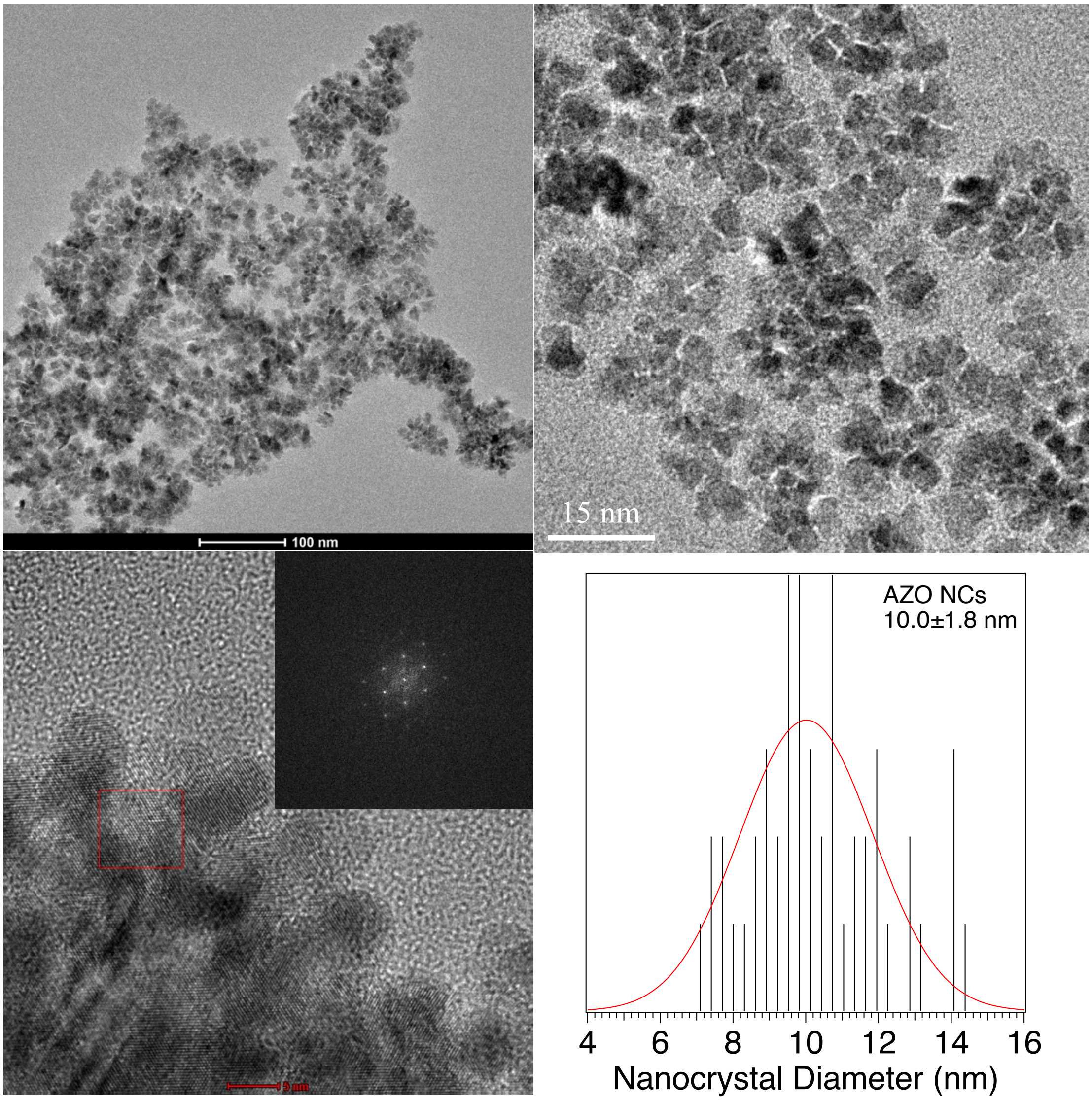

Figure 20. TEM/HRTEM/FFT images of AZO NCs and particle size distribution analysis based on 100 particles. Analysis of the lattice fringes shows d-spacings of 0.284 and 0.164 nm, reflecting the (100) and (110) planes respectively

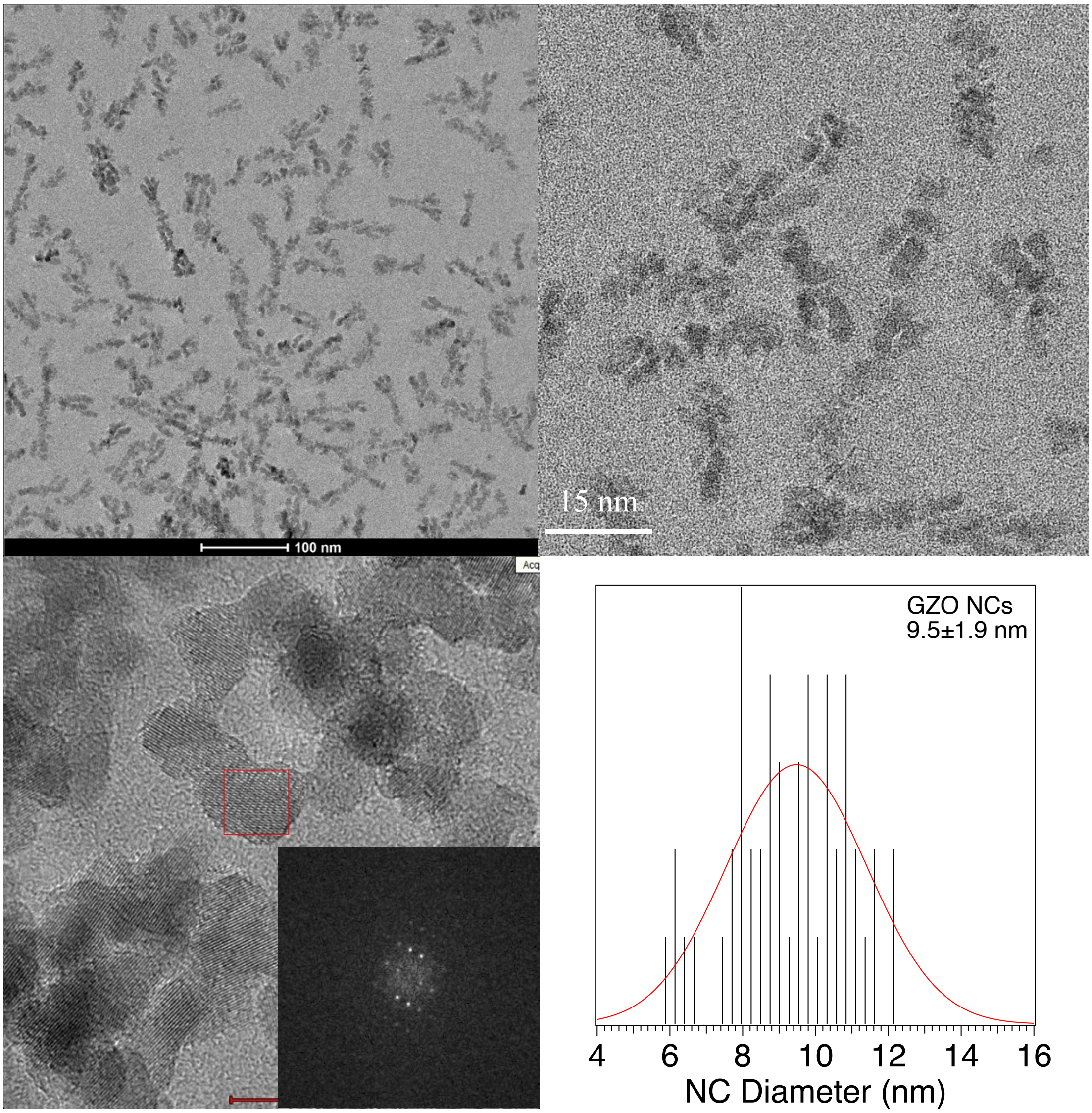

Figure 21. TEM/HRTEM/FFT images of GZO NCs and particle size distribution analysis based on 100 particles. Analysis of the lattice fringes shows d-spacings of 0.286, 0.265, and 0.249 nm, reflecting the (100), (002), and (101) planes respectively

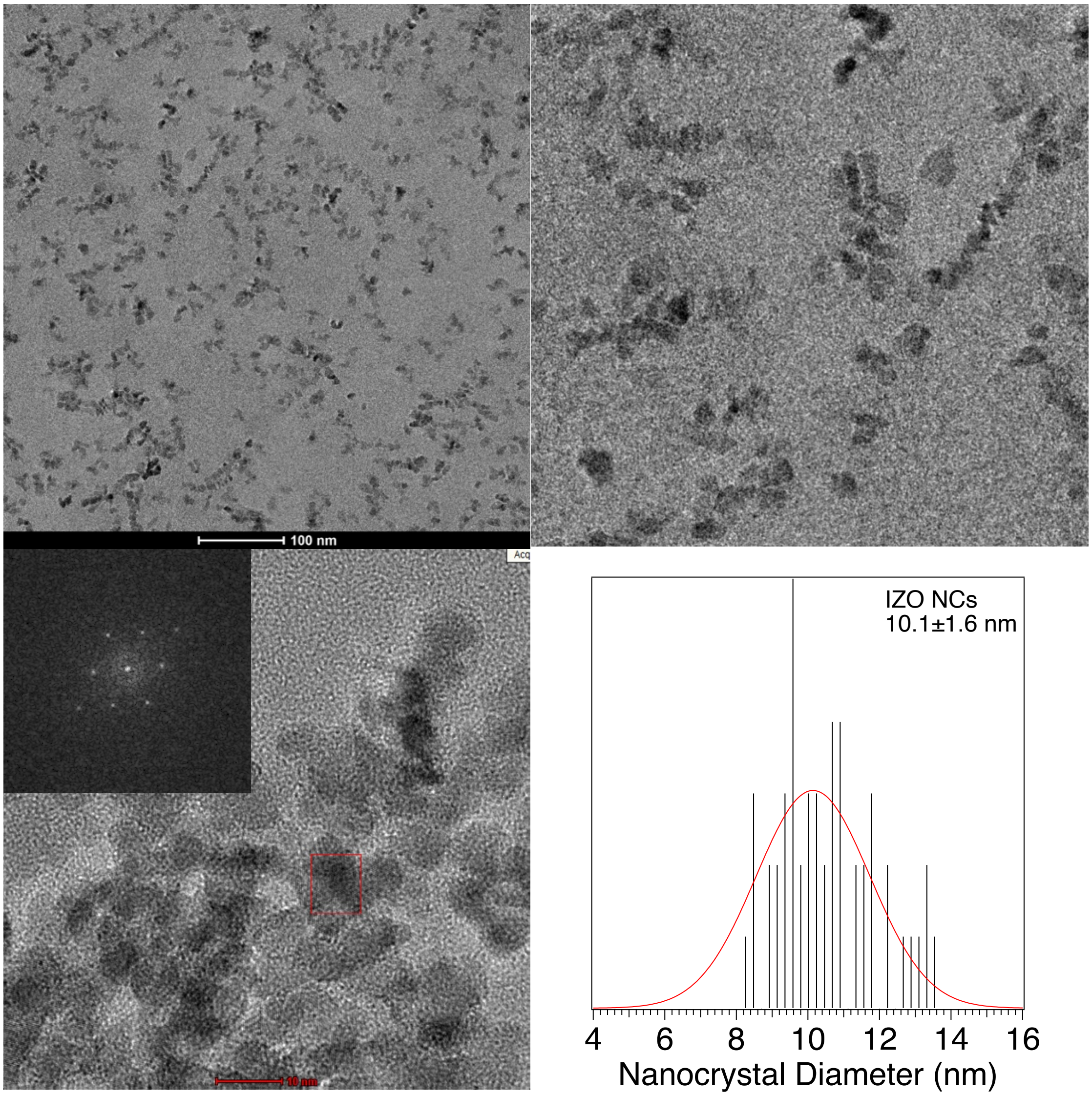

Figure 22. TEM/HRTEM/FFT images of IZO NCs and particle size distribution analysis based on 100 particles. Analysis of the lattice fringes shows d-spacings of 0.284 and 0.249 nm, reflecting the (100) and (101) planes respectively

3.3.1 Size Mismatch of the Aliovalent Dopant Ion

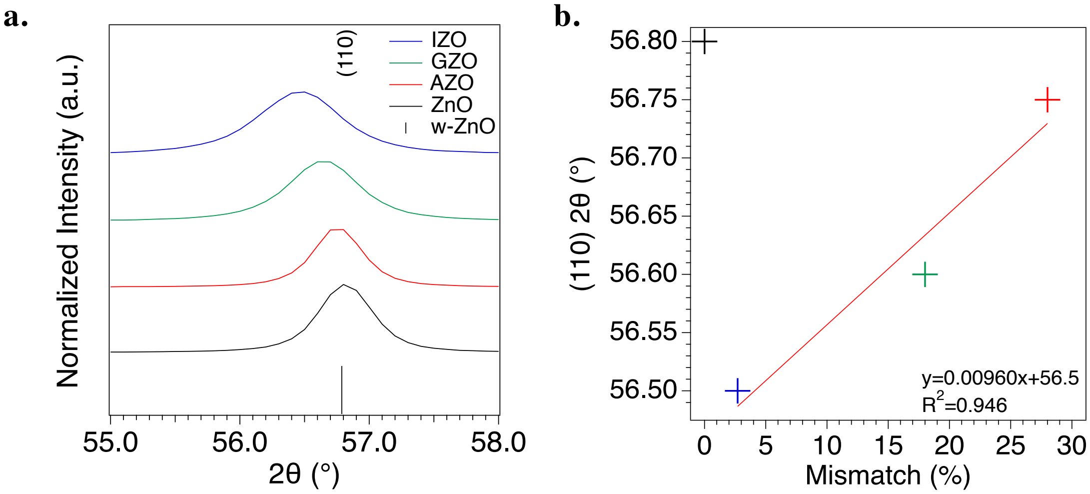

Figure 23. (a.) Closeup of the (110) lattice reflection for each sample. This feature shifts ~0.3° down with increasing size of the dopant ion. (b.) Vegard shift of the (110) reflection for MZO NCs. ZnO feature (Black) included for reference. IZO-Blue GZO-Green AZO

The incorporation of the aliovalent Al^{3+}, Ga^{3+} or In^{3+} guest ion into the ZnO host lattice, whether as a substitutional ion or an interstitial dopant, can either produce a n-type free carrier or introduce Zn vacancies (V_{Zn}) to ensure charge balance is maintained.[120] The effect on the pXRD pattern's average lattice spacing is telling, as a substitutional ion without vacancy formation is likely to follow Vegard's law reflecting the cation size difference, while V_{Zn} or interstitial ion occupation would likely deviate from the predicted Vegard law behavior. As smaller dopant atoms substitute at Zn host sites, the d-spacing in the lattice is expected to decrease and diffraction peaks will move to higher values of 2θ following Bragg's law.[121] The difference in size for substitutional occupation of the four-coordinate Zn site by Al^{3+} (0.53 Å), Ga^{3+} (0.61 Å), and In^{3+} (0.76 Å) dopant ions relative to Zn^{2+} (0.74 Å)[122] suggests that a clear increasing trend in d-spacing should be observable if all aliovalent ions occupy Zn sites.

The (110) reflection in the pXRD patterns (Figure 23) is seen to shift to lower values of 2θ or larger d-spacing with M^{3+} incorporation. From the Vegard behavior prediction for a substitutional site occupation,[123] the shift to lower 2θ is expected for In^{3+} as it is a slightly larger ion than Zn^{2+}, but not for the smaller Al^{3+} and Ga^{3+} ions. This phenomenon has previously been observed for group III doped ZnO.[124] Occupation of an interstitial site rather than the substitutional site could result in the observed d-spacing shift for the smaller cation. As cations are introduced into interstitial sites, the lattice will slightly expand to accommodate them, provided the atom is not significantly smaller than the interstitial space in which it occupies. As such, the pXRD shift for Al^{3+} and Ga^{3+} indicates that a significant percentage of these dopants may lie interstitially compared to In^{3+}, which typically incorporates substitutionally due to the excellent size matching. As a note, the larger GZO shift relative to AZO is believed to be due to the larger size of the Ga^{3+} ion, not less efficient substitution. This conclusion is supported by the expected Vegard behavior for each dopant given their relative size mismatches as well as the higher LSPR frequency of GZO compared to AZO.

3.3.2 Effect of Dopant Ion on Bandedge Absorption

The free carrier properties in the MZO samples can be evaluated by analysis of the LSPR via the Drude-Lorentz model[28] and from the band edge shift using Tauc plots.[87] The UV-Vis-NIR absorption spectra for ZnO and MZO NCs suspended in tetrachloroethylene is shown in Figure 24. As expected, the NCs are primarily transparent across the visible region and show a sharp increase in absorbance past 400 nm that is assigned to the band edge. The first derivative of the normalized absorption data is shown in the inset of Figure 24, allowing assignment of the $1S\text{-}1S_{3/2}$ exciton transition at 375 nm (3.30 eV) for the undoped ZnO, consistent with literature

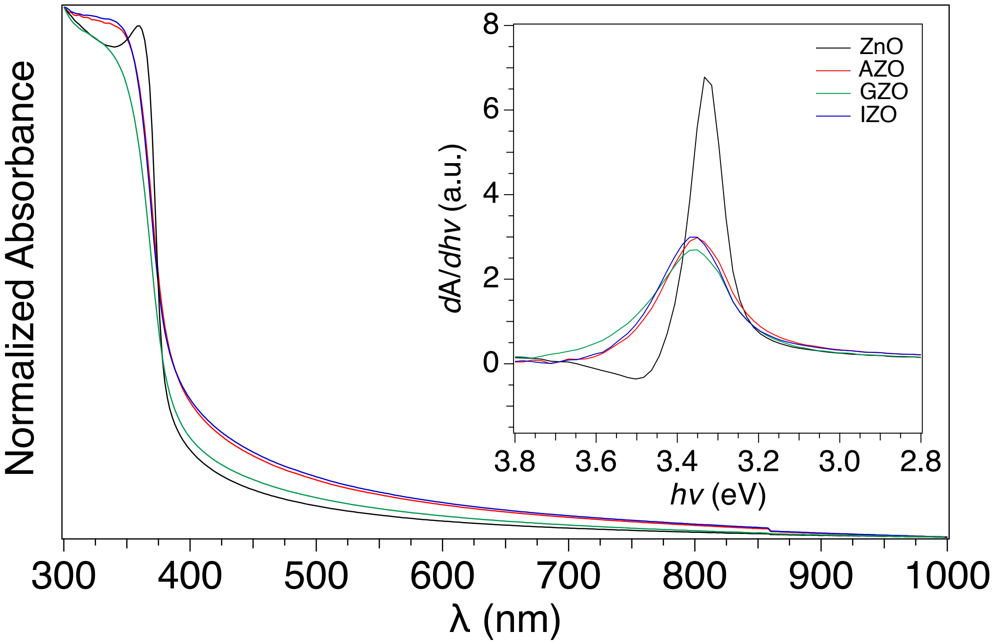

Figure 24. UV-Vis-NIR of ZnO (black), AZO (red), GZO (green), and IZO (blue) NCs. All spectra are normalized at 300 nm. (Inset) First derivative of the absorption bandedge, plotted in energy

reports.[125] As dopant ions are incorporated into the lattice, the exciton peak broadens and undergoes a hypsochromic shift to 3.36 eV. A direct band gap Tauc plot of this data reveals shifts in the optical E_g (3.26-3.29 eV), but no definitive correlation to ionic radii is observed in Figure 24. The change in band intensity is believed to reflect changes to the band structure from dopant incorporation, either via the breaking of symmetry or due to the presence of donor-acceptor states.[125]

3.3.3 Drude Fitting vs. Chemical Titration

The LSPR absorption feature provides more information about the effects of the different sized dopants on the resulting carrier density. In Figure 25, the observed LSPR extinction spectra are shown for AZO, GZO, and IZO. The spectra are fit using the Drude-Lorentz model[28]

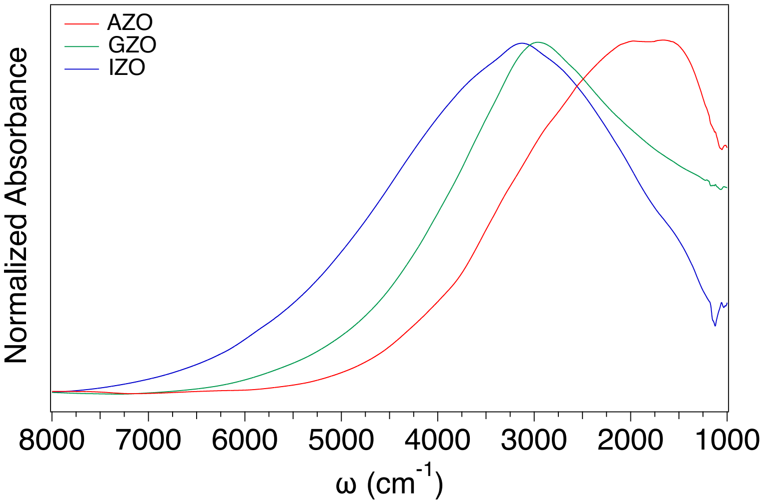

Figure 25. FTIR spectra of MZO NCs. Surface ligand absorption features have been removed for clarity

assuming a constant value of m^* (n-ZnO, $0.23m_e$)[126] and using an average value of 3.11 for the high frequency dielectric constant.[127] The extracted values of ω_p, Γ, and n are listed Table 2. A linear increase in carrier density with the ionic radius of the dopant atom is observed. While the observed shift in the LSPR parameters could be accounted for by a combination of empirical arguments including carrier delocalization via enhanced orbital expansion and changes to ionization potential as one progresses down a periodic group, such perturbations should also be reflected in the value of m^*. Therefore, it is critical to directly extract the value of carriers via chemical titration to accurately evaluate the changes in the extracted Drude parameters for each LSPR, since fitting the data using the simple Drude model assumes a constant m^* for all samples. In Table 2, a comparison is made between the Drude extracted carrier densities and the chemical titration measured carrier densities determined by observing the change in LSPR as the MZO sample is titrated against the one electron oxidant (Figure 27). An increase in carrier density from Al^{3+} to In^{3+} is observed; however, the extracted carrier densities are approximately an order

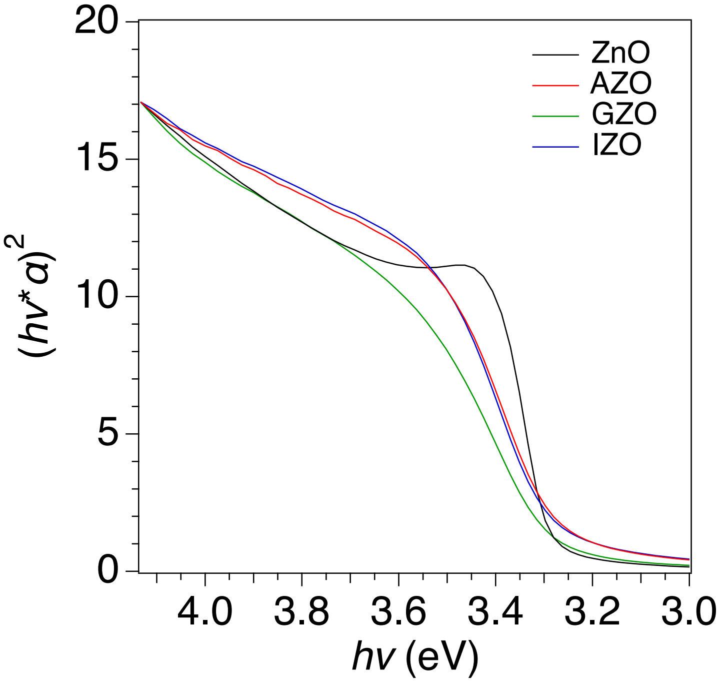

Figure 26. Direct band gap Tauc plot of MZO NCs. ZnO-3.29 eV, AZO-3.26 eV, GZO-3.28 eV, IZO-3.27 eV

Table 2. Simple Drude model fitting and chemical titration results for AZO, GZO, and IZO NCs

	AZO	**GZO**	**IZO**
Drude-Lorentz Fitting			
ω_p (cm^{-1})	4943.81 ± 10.38	6582.33 ± 20.28	8009.85 ± 11.35
Γ (cm^{-1})	1914.88 ± 7.94	2379.89 ± 14.81	2586.49 ± 10.22
$n/10^{20}$ (cm^{-3})	0.654 ± 0.002	1.159 ± 0.004	1.716 ± 0.002
e$^-$/Dopant	0.081 ± 0.001	0.143 ± 0.001	0.212 ± 0.001
NOBF$_4$ titration			
$n/10^{20}$ (cm^{-3})	12.3 ± 0.3	13.4 ± 0.3	15.4 ± 0.4
e$^-$/Dopant	1.53 ± 0.04	1.66 ± 0.04	1.91 ± 0.05

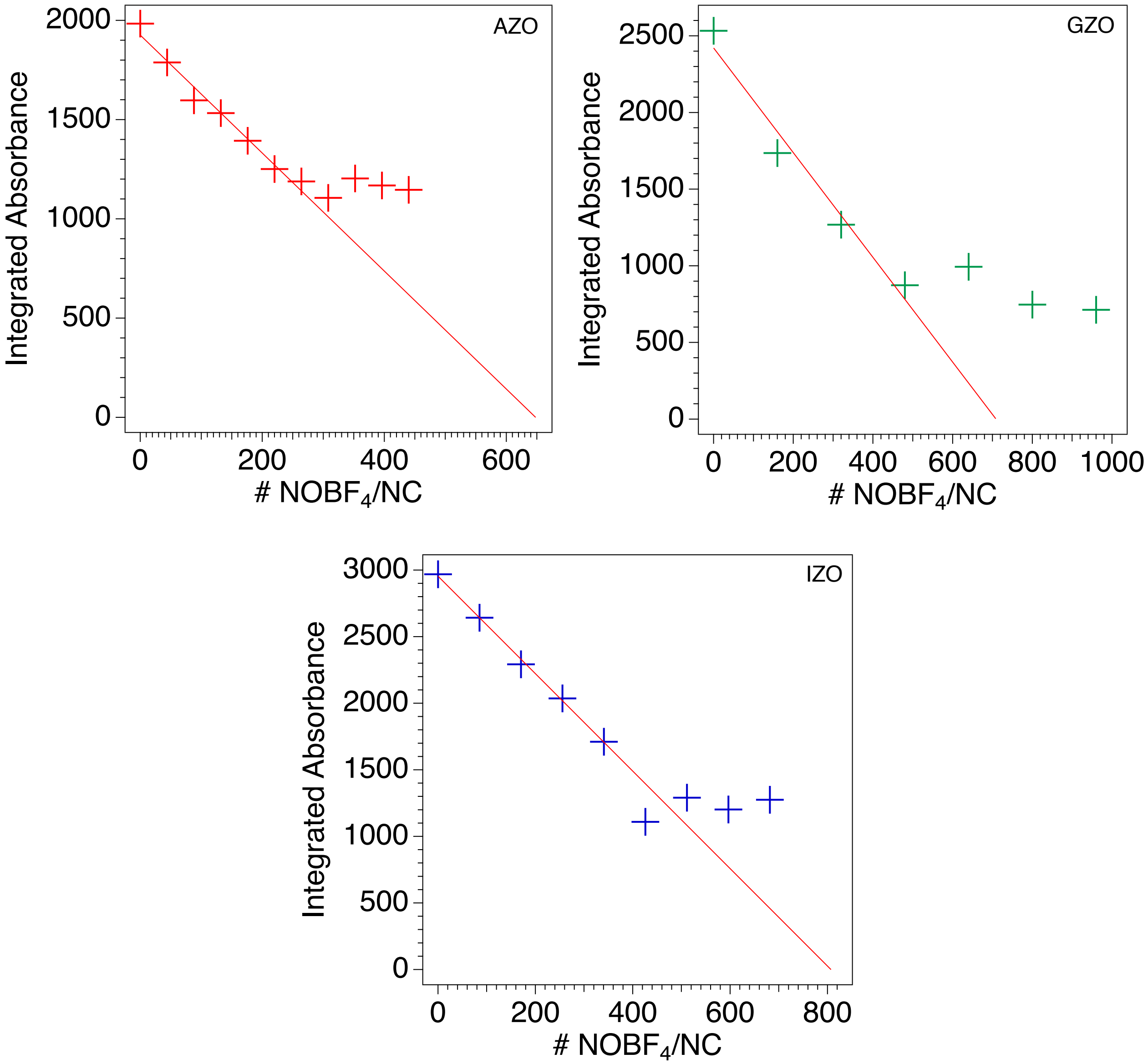

Figure 27. NOBF$_4$ chemical titrations of MZO NCs. The initial linear regime is fit and the extrapolated x-intercept is used to calculate the theoretical amount of NOBF$_4$ required to oxidize all free carriers.

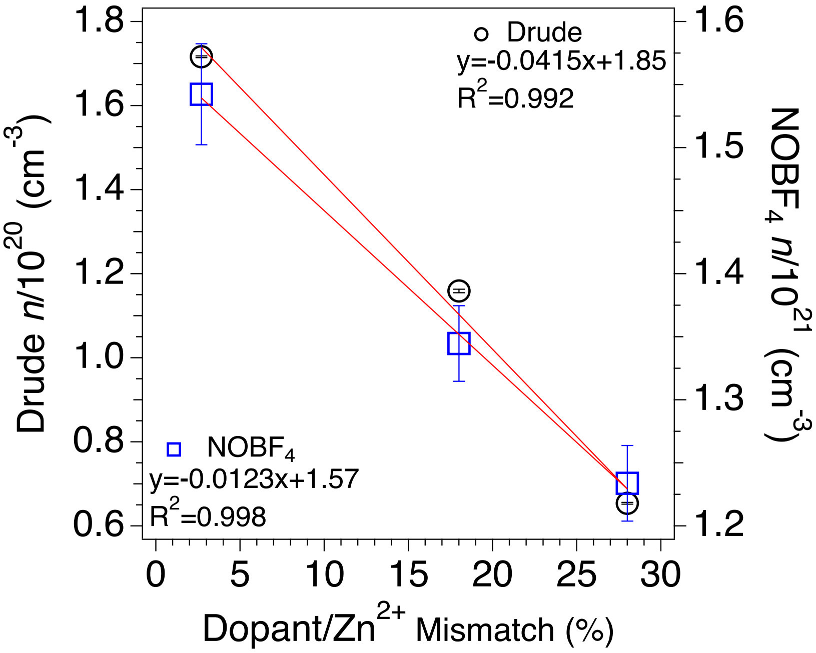

Figure 28. Drude and NOBF$_4$ measured carrier densities vs. relative size mismatch of the incorporated dopant with respect to the Zn host site

of magnitude higher than those predicted by the Drude model. Plotting the Drude and NOBF$_4$ measured carrier densities for each sample as a function of dopant size mismatch reveals a linear trend (Figure 28). As the size mismatch increases from In^{3+} to Al^{3+}, the carrier density continues to decrease. The lack of free carriers generated per dopant ion is referred to as dopant deactivation and is an important property to consider when examining PSNCs, as high levels of deactivation can significantly affect the resulting plasmonic properties.[29,83]

3.3.4 Evidence of Spinel Formation

One plausible explanation for the observed cation size dependence has been previously suggested in the AZO thin film literature. The large size mismatch of Al^{3+}/Zn^{2+} results in poor dopant solubility at higher concentrations, which induces a conductivity limit in thin films past which adding more Al^{3+} dopant does not induce more $Al_{Zn}^{\cdot}$ defects to form. Instead, the dopant ions begin to form insulating layers of Al_2O_3 at the grain boundaries of the thin film.[39,128,129] This phenomenon should hold true for Ga^{3+} and In^{3+} as well, but the increasing dopant solubility of these ions due to better size matching will lead to a higher percent of $M_{Zn}^{\cdot}$ defects forming for these larger dopant ions. Hard x-ray photoelectron spectroscopy (XPS) studies by Gabás et al. have even suggested that Ga incorporates only as a substitutional dopant in ZnO films.[129] This is applicable to PSNCs in that only a certain percentage of the nominal dopant concentration will aliovalently substitute and generate a free carrier for the LSPR. The Kröger-Vink notation[130] for this aliovalent substitution defect is shown in eqn. 14.

$$(2M_{Zn}^{\cdot}:O_i'')^x \rightarrow 2M_{Zn}^{\cdot} + {}^{1}/_{2}\,O_2(g) + 2e' \tag{14}$$

$$4M_2O_3 + 3Zn_{Zn}^x \rightarrow (2M_{Zn}^{\cdot}:V_{Zn}'')^x + 3ZnM_2O_4 \tag{15}$$

Free charge carriers can also be generated via the interstitial incorporation of dopant ions, but this inclusion at the octahedral interstitial sites of w-ZnO will favor the formation of insulating spinel (AB_2X_4) inclusions (eqn. 15) within the PSNC. Evidence for the formation of spinel inclusions in Cr:ZnSe NCs has been previously reported by the Strouse group[131] and the $ZnAl_2O_4$/$ZnGa_2O_4$ spinels are known to form more readily than the $ZnIn_2O_4$ analogue due to the smaller size of the B site cation.[132]

3.3.5 Dopant Deactivation

The deactivated dopants can be accounted for in several ways. The first of these is the formation of an insulating spinel phase, as previously discussed. The next likely source of deactivation lies in the existence of a surface depletion region, where dangling bonds at the surface result in pinned carriers that do not contribute to the resulting LSPR feature.[83,133] For a spherical, 10 nm NC, a mere 1 nm surface depletion region would result in ~27% dopant deactivation (Appendix), provided the dopant is incorporated homogenously as is the case for the bottom-up slow injection synthetic method utilized in this study.[79,112] Studies by Hutchison and coworkers suggest surface passivation by a non-doped metal oxide layer enhances plasmonic properties, signifying that surface depletion is a contributor.[134] Since the contribution of surface carriers would be size dependent, further studies are needed to rule out the contribution entirely. A third source of dopant deactivation lies in the pinning of carriers at anion vacancies within the crystal, which would produce F-centers. These defects are well known in ZnO[7,135] and result in the introduction of color to an otherwise transparent semiconductor.

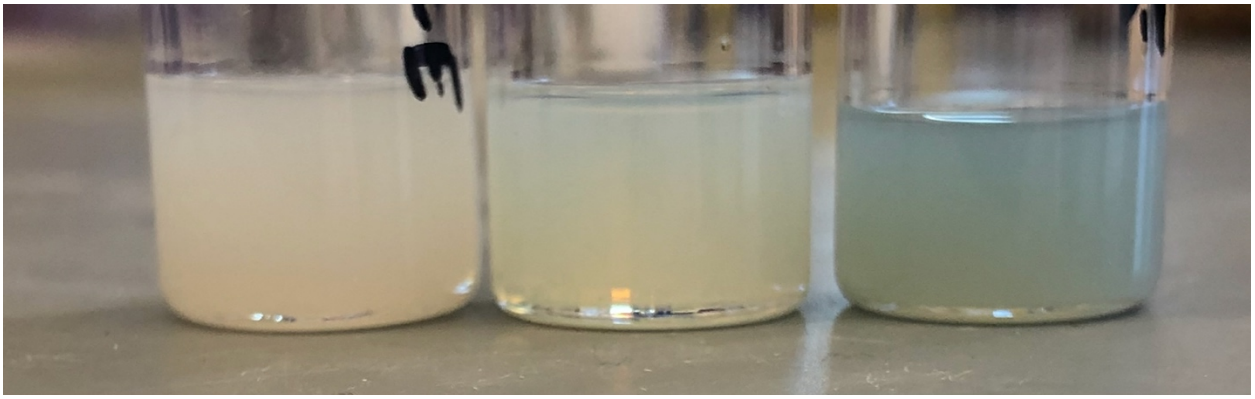

Figure 29. Photograph (from left to right) of AZO, GZO, and IZO NCs

Each plasmonic sample exhibits a unique color depending on the dopant (Figure 29), which supports the formation of F-centers in these samples. Oxygen vacancies that are generated both intrinsically and/or as a side effect of aliovalent substitution can pin free carriers in anionic sites where they will not contribute to the observed LSPR. However, these F-centers can still be titrated via $NOBF_4$, which would result in inflated values for the free carrier density measurements.

This is also shown in Table 2, where the $NOBF_4$ determined free carriers/dopant all exceed values of 1, the theoretical maximum for aliovalent substitution efficiency. These results suggest that there are several defect sites being generated upon dopant incorporation that result in "invisible carriers", in that they do not contribute to the LSPR and therefore its frequency/extinction. It is also shown in Figure 28 that the slope of the Drude fit is ~3.4x greater than that of the chemical titration fit. Since the Drude model only accounts for carriers that contribute to the observed LSPR, while the chemical titration totals all free electrons (including those trapped at defect sites), this suggests that there are more pinned carriers than free carriers. The greater number of pinned carriers formed compared to free carriers generated via aliovalent substitution means that the increase in free electron count shown in the Drude model has a small effect on the total electron concentration and therefore results in a lower value for the slope of the $NOBF_4$ plot.

The presence of lattice effects on carrier deactivation leading to spectral changes in the LSPR is also evidenced in the LSPR dampening value (Γ). This is not surprising, as the dampening term is typically dictated by surface, impurity, electron-electron (el-el), and electron-phonon (el-ph) based scattering mechanisms.[82,136,137] Since each sample has a similar size, morphology, and concentration of dopant ions, the effects from surface and impurity scattering can be considered to be negligible across the MZO NCs. An increase in carrier density would result in higher el-el scattering and therefore an increase in Γ. The Drude fitting reflects this trend as Γ increases linearly with carrier density from Al^{3+} to In^{3+} (Figure 30). This trend supports the hypothesis that IZO NCs generate a larger number of free carriers due to the better size match of In^{3+}/Zn^{2+} compared to Al^{3+} and Ga^{3+}.

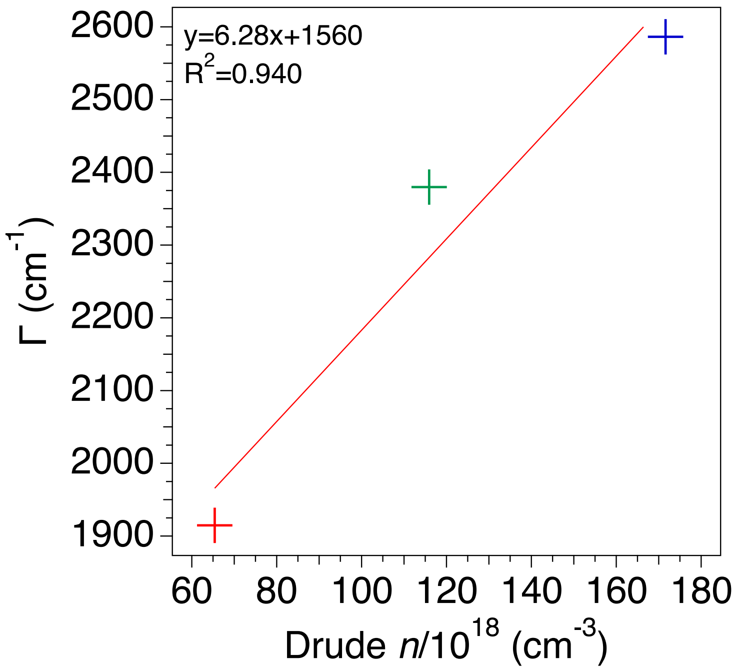

Figure 30. Dampening constant as a function of carrier density. The direct proportionality indicates that el-el scattering is the primary cause of the increase in linewidth.

3.3.6 Advanced Effective Mass Model for Drude Correction

While higher dopant activation can account for the increases in both ω_p and Γ, the NOBF$_4$ measured carrier densities are still approximately one order of magnitude higher than those determined using the simple Drude model. One method for examining the effects of these additional electrons is to compare to the literature value for a corrected Drude model previously proposed by Jung and Pederson for ZnO.[84] This model examines the large deviations between the calculated and experimentally measured ω_p by using a simple effective mass approach compared to when using full band structure calculations specifically for ZnO. The proposed advanced effective mass model of ω_p contains a correction term to eqn. 9 in order to account for this deviation.

$$\omega_p^2 = \frac{e^2 n}{\varepsilon_0 m^*} \frac{1}{\sqrt{1+(9\pi^2 n)^{2/3}\hbar^2/(m^*\alpha)}} \qquad (9)$$

In this eqn., α is the correction factor designed to account for the change in local band shape as the Fermi level moves further into the conduction band with increased n-type doping. The change in the degree of parabolicity of the local density of states (LDOS) results in a deviation in the value of m^*, a phenomenon that has been previously shown in plasmonic ITO and InN NCs.[29,69] In other words, m^* cannot always be treated as a constant with increasing values of n and a varying Fermi level relative to the conduction band minimum. This holds doubly true for MZO systems, where the change in dopant identity and site incorporation will also change the aliovalent substitution efficiency for each sample.

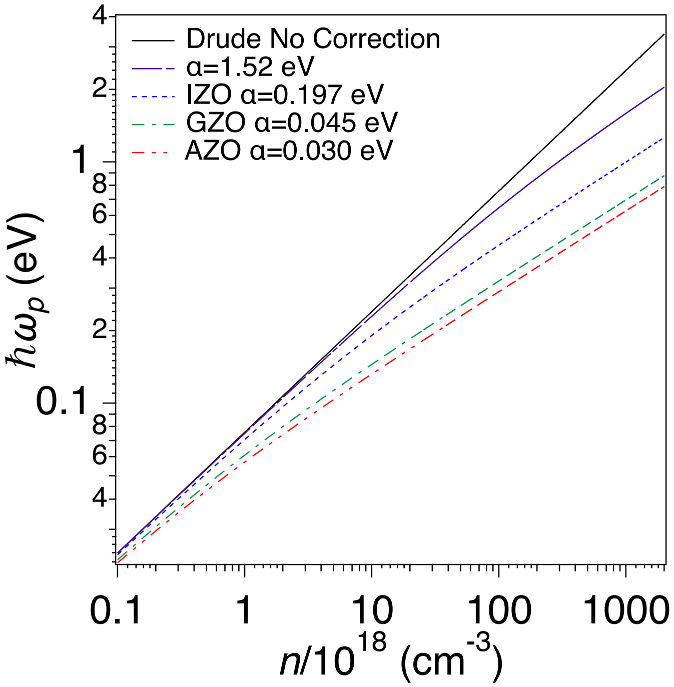

Figure 31. Advanced effective mass model calculations for MZO NCs compared to the uncorrected Drude model and the literature value for ZnO α=1.52 eV

By combining the experimentally measured values of ω_p (obtained via FTIR) and n (obtained via chemical titration), the value for α can be calculated and the relationship between n

and ω_p can be modeled for each sample. These values, and their effect on the deviation from the simple Drude model, are presented in Figure 31. The degree to which each sample varies from the simple Drude model calculated values corresponds to the ionic radius of the dopant. The uncorrected Drude model is linear on a log/log scale, while the MZO samples start similarly at low carrier concentrations and then curve downwards at higher values. As the percent mismatch of the dopant increases, so too does the deviation from the uncorrected model. This reflects the change in aliovalent substitution efficiency with decreasing dopant ionic radius. The mean free path of the free carriers is reduced as a larger percentage of the dopant ions are incorporated interstitially, which causes the carrier mobility to decrease and m^* to increase. Even at carrier densities as high as $1*10^{21}$ cm^{-3}, the LSPR for MZO NCs is still limited to MIR region due to this ineffective aliovalent incorporation and its resulting effects on free carrier generation and the mobility of free carriers.

In addition to the uncorrected Drude model, the value for α determined via full band structure calculations for ZnO (1.52 eV) is also plotted.[84] The deviation for all three MZO samples from the theoretical value for n-type ZnO reflects the number of pinned carriers that exist from various defect sites such as F-centers and the existence of a surface depletion region. The difference between the calculated values of α for each sample and the literature value of 1.52 eV reflects the change in the number of pinned carriers generated depending on the dopant identity. These values (AZO-1.49 eV, GZO-1.48 eV, IZO-1.32 eV) indicate that better size matching of the dopant ion also leads to less pinned carriers being generated and ultimately higher dopant activation. The nature of these defects, surface depletion region, and the local chemical environment of dopant and host lattice nuclei are investigated in the next chapter.

3.4 Conclusions

Al, Ga, and In doped (12%), 10 nm ZnO NCs have been synthesized and observed to exhibit dopant dependent plasmonic properties. ICP-MS and analysis of the optical band edge confirm dopant incorporation and free carrier generation. pXRD and TEM data show that all samples are of the wurtzite phase and that dopant incorporation has no significant effect on the size or morphology of the NCs. Analysis of the (110) reflection revealed a Vegard shift to lower values of 2θ, indicating the smaller dopant ions (Al^{3+}, Ga^{3+}) incorporate interstitially as well as substitutionally. This effect results in a difference in the number of free carriers generated per dopant ion, which is confirmed via Drude fitting of the LSPR and by chemical titration. Carrier density and LSPR dampening increase inversely with M^{3+}/Zn^{2+} size mismatch, which is explained by aliovalent substitution efficiency and increased el-el scattering. Interstitial dopants sit in octahedral coordination environments and likely form an insulating spinel phase (AB_2X_4), which lowers dopant activation. Deviations between the Drude and $NOBF_4$ calculated carrier densities indicate that there are many pinned carriers, which also do not contribute to the observed LSPR. Such pinned carriers are analyzed using an advanced effective mass model, which takes into account the full band structure of ZnO and its resulting effect on m^*. These results inform on the mechanisms behind the formation of LSPRs in ZnO and are crucial for the future rational design and application of PSNCs.

CHAPTER 4

NMR CRYSTALLOGRAPHY OF PLASMONIC M^{3+} DOPED ZINC OXIDE NANOCRYSTALS

4.1 Introduction

Plasmonic semiconductor nanocrystals (NCs) have grown in popularity due to their tunable carrier density and ultrafast switching plasmon resonances.[38,54,104,113] A great deal of research has focused on near-infrared (NIR) plasmonic NCs for electrochromic and biological applications.[73,108,138] However, materials with tunable and high extinction mid-infrared (MIR) absorption bands are needed for applications in resonant surface enhanced Raman,[22,23] MIR sensing,[105,107] and thermal waste management.[41,119] Photo and aliovalently doped ZnO NCs has been shown to exhibit localized surface plasmon resonances (LSPRs) in the MIR region of interest for the previously mentioned MIR applications.[7,30,111,112] Aliovalent doping of ZnO with group 3A metals such as Al^{3+}, Ga^{3+}, and In^{3+} provide an advantage over photodoping in that the materials are intrinsically plasmonic and do not require a hole scavenger in order to generate free carriers.[30,112]

It has been previously shown in chapter 3 that the size of the dopant in MZO NCs will affect how it incorporates into the ZnO lattice and ultimately the resulting plasmonic properties.[30] Better dopant/host size matching leads to an increase in the efficiency of aliovalent substitution and therefore the free carrier density, which leads to an increase in the LSPR frequency of the sample. While the LSPR of MZO NCs increases in energy from Al^{3+} to In^{3+},[30,112] these materials do not show any significant shift in energy with increased dopant incorporation. This result is in contrast with other known n-type plasmonic materials such as ITO[10,29] and In:CdO,[63] where increasing the dopant concentration is the key factor to tuning the

LSPR frequency. In order to identify the cause of this phenomenon, the variables which govern the LSPR's frequency must be understood.

The observed frequency of a LSPR is determined by its plasma frequency (ω_p), which can be related to both free carrier density (n) and effective mass (m^*) by the Drude model,

$$\omega_p = \sqrt{\frac{ne^2}{\varepsilon_0 m^*}} \tag{2}$$

where e is the charge of the free carrier (an electron for a n-type system such as MZO) and ε_0 is the permittivity of free space.[27] Following this equation, there are two possibilities for a LSPR to remain at the same frequency with varying dopant levels: 1) both n and m^* change while maintaining a constant n/m^* ratio (e.g. InN)[69] or 2) neither of these variables change at all. The first of these possibilities represents the case where the change in the local density of states as the Fermi level moves through the conduction band with increasing carrier density causes a corresponding increase in m^*. The second scenario describes a situation where increasing dopant concentration does not result in higher free carrier concentrations. This may occur due to the presence of deactivated dopants through a surface depletion layer, defect mediated pinning of free carriers, or inclusions of insulating microphases. Previous studies of MZO NCs via far-field optical measurements suggest that dopant deactivation is the key,[30] however no direct evidence of the defect sites can be provided from absorption data. Here, the exact nature of the deactivated dopants is directly examined using SSNMR. SSNMR is an element specific probe, which allows for the investigation of the local chemical environments of a wide variety of nuclei. This provides direct insight into the nature of defects within the NC by investigating both the dopant and host lattice nuclei. This work utilizes ^{27}Al, ^{71}Ga, and ^{67}Zn SSNMR to examine dopant incorporation, defect formation, and how the generation of free carriers impacts the NMR spectra.

4.2 Experimental Methods

4.2.1 Synthesis of X% M:ZnO Nanocrystals (M=Al^{3+}, Ga^{3+})

MZO NCs were synthesized using a modified method previously reported by Gaspera and coworkers.[112] X mmol of $Al(acac)_3$ or $Ga(acac)_3$ were combined with 5-X mmol of $Zn(OAc)_2$ dihydrate and 10 mL of oleic acid. This mixture was degassed at 110 °C for one hour, followed by the addition of 5 mL of oleylamine and subsequent degassing for 30 min. The metal oleate precursors are then added dropwise at a rate of 0.3 mL/min to 62.5 mL of oleyl alcohol kept at 240 °C while N_2 is continuously run over the reaction. After the injection is complete, the solution was kept at 240 °C for an additional 20 minutes, followed by cooling to R.T. and isolation/cleanup of the NCs using toluene/ethanol (3x) and centrifugation.

4.2.2 General Characterization

ICP-MS was performed using a Thermo Scientific iCAP RQ ICP-MS to confirm the ratio of (Al/Ga):Zn in the NCs. Samples were digested in concentrated nitric acid and then diluted to 2% HNO_3. Calibration curves were prepared from serial dilutions of a Al/Ga/Zn standard dissolved in 2% nitric acid with R^2 values >0.995 for all ions. Each sample was measured in triplicate after an initial survey run and there was a minimum 30 second wash time between samples.

pXRD patterns were collected with a Rigaku MiniFlex powder X-ray diffractometer using a Cu-Kα. Samples were dried out and crushed into a fine powder and then loaded onto a zero-background micro-powder plate. Scans were collected from 20-70° 2ϴ at a rate of 5°/min and a 0.1° step size. Whole powder pattern fitting and the Halder-Wagner method for Scherrer analysis were completed using the Rigaku SmartLab Studio software and performed for all NCs.

FTIR was performed on purified MZO NCs were suspended in tetrachloroethylene and diluted to appropriate concentrations. Samples were then loaded into a Pike Technologies Liquid FTIR cell with BaF_2 windows and a pathlength of 0.5 mm. FTIR measurements were performed in transmission mode using a Jasco 6800 FTIR spectrometer. Ligand absorption features were removed using Jasco's Spectra Manager software and the spectra were smoothed using a Savitzky-Golay filter.

4.2.3 Multinuclear SSNMR

All SSNMR experiments were conducted at the National High Magnetic Field Laboratory (NHMFL). ^{27}Al spectra were acquired using 18.8 T (800 MHz) and 11.7 T (500 MHz) spectrometers with a spin-echo experiment under 12 kHz MAS conditions. The $\pi/2$ pulse was set to 9.5 μs and the recycle day was set to 5 s. ^{71}Ga spectra were acquired using a 14.1 T (600 MHz) spectrometer with a quadrupolar Carr-Purcell-Meiboom-Gill (QCPMG) pulse sequence under static conditions. The π pulse was set to 2.5 μs and the recycle delay was set to 0.5 s. ^{67}Zn spectra were acquired using a 19.5 T (830 MHz) spectrometer with a QCPMG pulse sequence under static conditions. The π pulse was set to 16.667 μs and the recycle delay was set to 2.5 s.

4.3 Results and Discussion

X% M:ZnO NCs (M=Al^{3+}, Ga^{3+}) were synthesized following the procedure of Gaspera and coworkers.[112] The dopant concentration was varied for both Al:ZnO (AZO) and Ga:ZnO (GZO) NCs, as verified by ICP-MS. pXRD patterns (Figure 32). for all samples are assigned to the hexagonal wurtzite phase of ZnO (PDF #036-1451). No significant changes in lattice parameter or formation of secondary phases are observed with increased doping levels of both Al

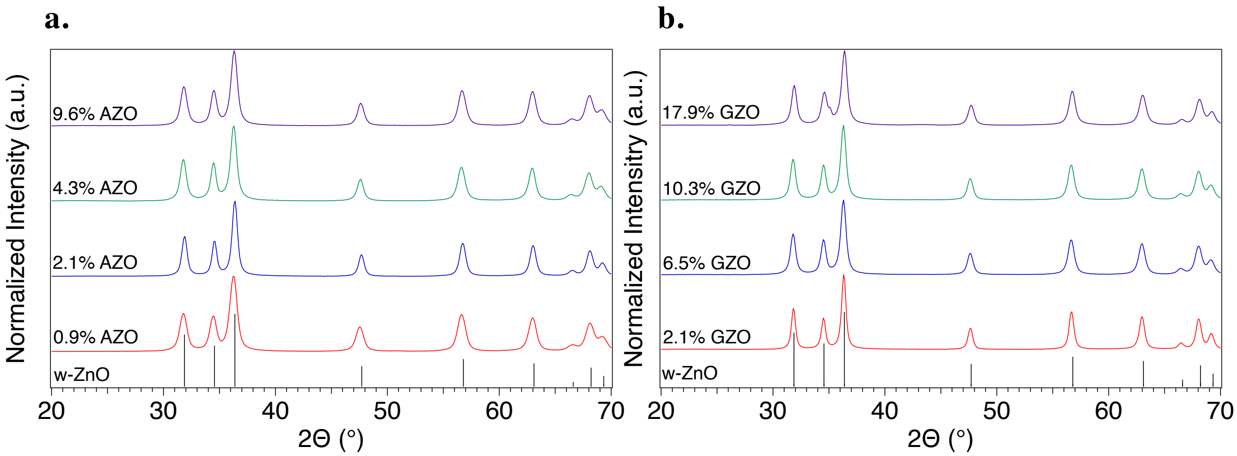

Figure 32. pXRD patterns of (a.) X% AZO NCs and (b.) X% GZO NCs

and Ga. Whole powder pattern fitting and Scherrer analysis show consistent sizes for all NCs of approximately 10 nm.

4.3.1 Lack of LSPR Tunability with Increased Doping

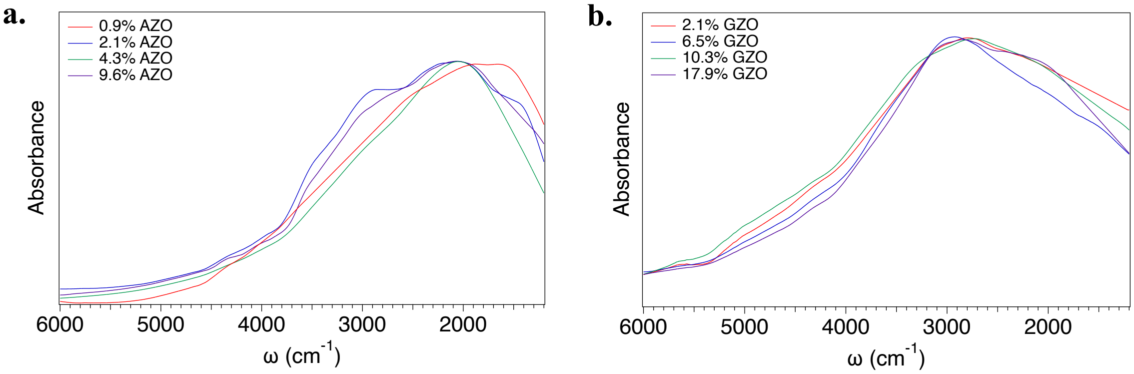

Figure 33. FTIR spectra of X% AZO (a.) and GZO (b.) NCs. Ligand absorption features are removed for clarity and spectra are smoothed using a Savitsky-Golay filter

FTIR spectra of the AZO and GZO NCs (Figure 33) reveal LSPRs in the MIR region centered at roughly 2000 and 2700 cm^{-1} respectively. The unique plasmon frequency for each sample has been previously reported.[112] The plasmon resonance shows no significant change in frequency when the dopant concentration is increased, unlike what is seen for other n-type systems such as ITO[10,29] or In:CdO.[63] This indicates that additional free carriers are not being generated with increased doping levels or that the carriers are being pinned at defect sites. The differing ionic radii of the dopants results in varying amounts of aliovalent substitution and therefore differences in the free carrier concentrations. Both Al^{3+} (0.53 Å) and Ga^{3+} (0.61 Å) ions have a smaller ionic radius than Zn^{2+} (0.74 Å) when located in a IV coordinate crystal environment.[122] This size mismatch leads to a combination of substitution and interstitial dopant incorporation. Far-field optical studies can only provide indirect evidence of the relative amounts of aliovalent substitution. Therefore, SSNMR was used as an element specific probe to directly investigate the local chemical environments of these dopant atoms.

4.3.2 ^{71}Ga SSNMR

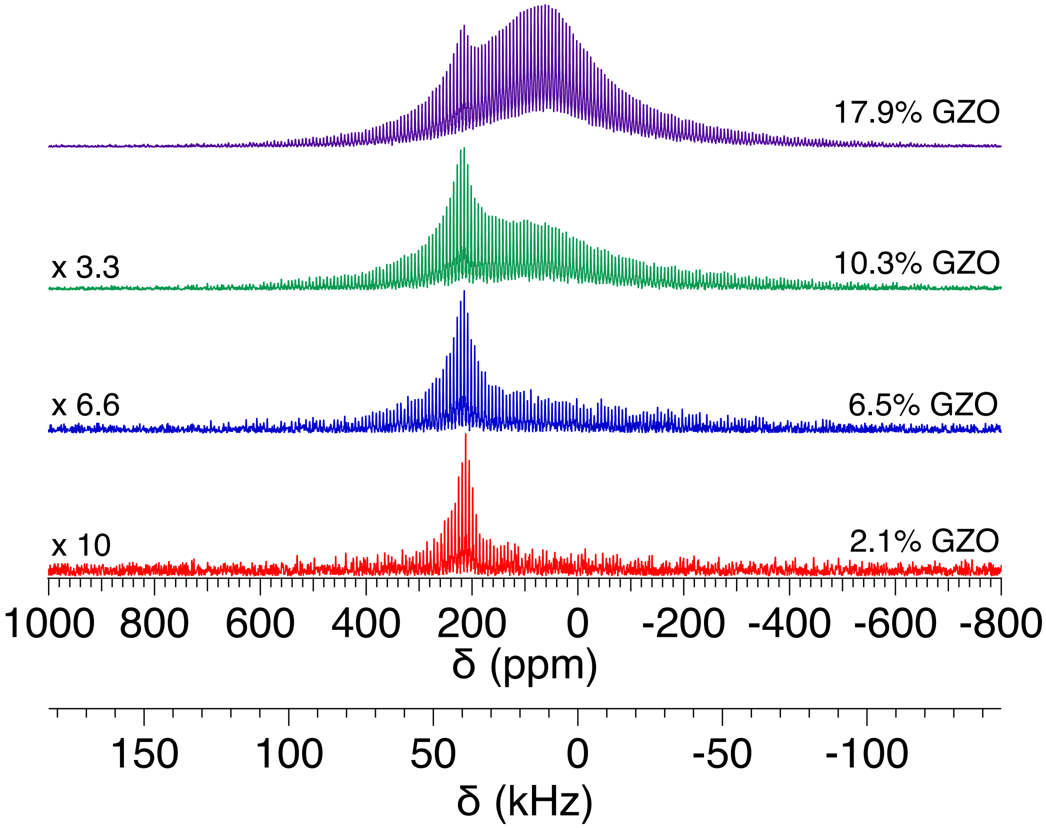

Figure 34. ^{71}Ga QCPMG spectra of X% Ga:ZnO NCs. Spectra were acquired under static conditions at 14.1 T (600 MHz).

GZO NCs with a range of doping concentrations were synthesized to determine the relative concentrations of substitutional and interstitial incorporation. Figure 34 shows the ^{71}Ga quadrupolar Carr-Purcell-Meiboom-Gill (QCPMG) spectrum for each sample.[47,48] At low concentrations of Ga^{3+}, there is only one feature present in the NMR spectrum centered at approximately 210 ppm. This signal is assigned to the IV coordinate $Ga_{Zn}^{\cdot}$ substitution, which generates one free carrier per occurrence due to the difference in oxidation states of Ga^{3+} and Zn^{2+}. The Zn site in the wurtzite lattice is a highly symmetric (C_{3v}) and amenable crystal site towards hosting Ga^{3+} ions.[124] This results in a very well-defined NMR signal with a distinct quadrupolar lineshape due to the nuclear spin of ^{71}Ga (I=3/2). As the dopant concentration increases, a new signal appears that is centered around 70 ppm. This feature is assigned to the disordered VI coordinate Ga interstitial. Within the wurtzite lattice lies an interstitial space where smaller ions can coordinate to six lattice oxygens.[124] The disorder of this site results in a broadening of the NMR signal and a loss of the distinct quadrupolar lineshape as a gaussian distribution of sites are formed. This distribution is formed due to the larger freedom of movement of the Ga^{3+} ion in the interstitial site when compared to the crystalline substitution.

Oxygen vacancies are also expected in the crystal structure, which would lead to V and possibly IV coordinate Ga^{3+} interstitials. These results indicate that Ga^{3+} initially prefers to incorporate entirely as a substitutional dopant. At 6.5% Ga, signal from the interstitial site begins to appear and continues to increase with further doping. The VI coordinate Ga^{3+} is likely forming a spinel microinclusion within the lattice. This line phase (AB_2O_4) is made up of a IV coordinate Zn^{2+} A site and a VI coordinate Ga^{3+} B site.[139] The spinel phase has a wide bandgap (~5 eV)[139] and forms an insulating phase within the NC that results in no free carriers being generated from interstitial dopant. These results explain why the LSPR does not change frequency with increased Ga^{3+}, since aliovalent doping reaches a maximum at low concentrations and further interstitial doping results in large amounts of deactivated dopant.

4.3.3 ^{27}Al SSNMR

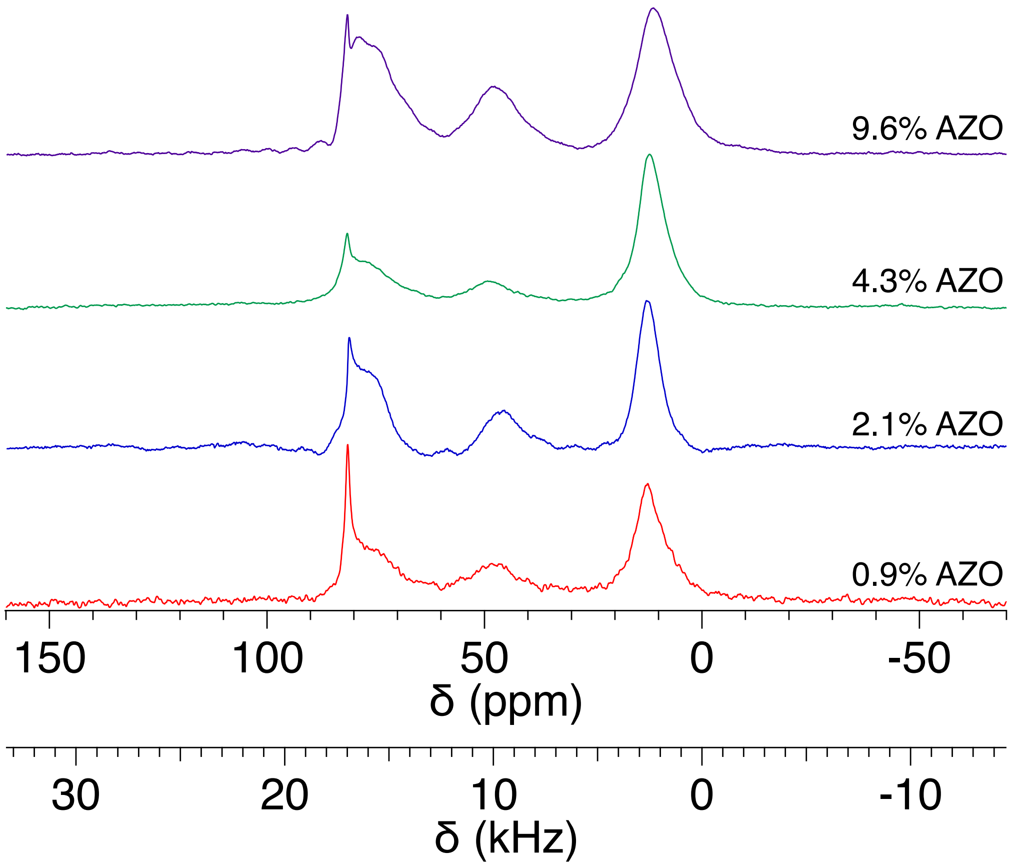

Figure 35. ^{27}Al spin-echo spectra of X% AZO NCs. Spectra were acquired under 12 kHz MAS at 18.8 T (800 MHz).

To investigate the possible dopant coordination environments more precisely within the ZnO lattice, a range of AZO NCs with varying dopant concentrations were prepared. While ^{27}Al is also a quadrupolar nucleus (I=5/2), it typically presents sharper features compared to ^{71}Ga.[140] This allows for more insight into the possibility of less than VI coordinate interstitial sites. Figure 35 shows the ^{27}Al SSNMR spectra for each AZO sample, revealing four unique NMR signals. The sharp feature located at 80 ppm is assigned to the IV coordinate $Al_{Zn}^{\cdot}$ substitution. The high symmetry of the Zn site results in a very narrow peak found in the frequency region expected for a IV coordinate Al site.[140] The feature centered at approximately 10 ppm is assigned to the interstitial Al. This chemical shift region previously reported to be where VI coordinate Al sites will appear.[141] Similar to the ^{71}Ga spectra, there is a gaussian distribution of interstitial sites that leads to a broadening of the quadrupolar lineshape of this feature. However, some of the quadrupolar asymmetric tailing towards lower frequency is visible at low doping concentrations.

This Al site also forms a spinel phase ($ZnAl_2O_4$), which behaves identically in terms of dopant deactivation to that seen in the GZO NCs. In contrast to the GZO, the IV coordinate spinel Al can be seen at approximately 75 ppm. This signal is present due to inversion of the A and B sites of the spinel, a well-known phenomenon.[139] In a fully inverted spinel, 50% of the trivalent B site cations swap with 100% of the divalent A site cations. The measure of the number of antisite defects that are formed is referred to as the degree of inversion. By performing a multipeak fitting of the ^{27}Al spectra, the integrated area for each site can be calculated. The ratio of the IV and VI spinel site all samples is approximately 1:1, indicating that there is equal occupation of the A and B sites by the Al cations. This ratio can only be achieved by a fully inverse spinel $Al_A(ZnAl)_BO_4$. Since the Al^{3+} dopant is known to incorporate at the IV coordinate wurtzite Zn site, the formation of an inverse spinel is not unexpected as interstitial Al likely creates the microinclusion by forming defect complexes with the existing aliovalently substituted Al. These spinel inclusions have no long-range ordering and are therefore invisible via pXRD. SSNMR can identify these defects as it only relies on the local chemical environments of each Al site (i.e. short range order).

An initially unexpected feature appears at approximately 50 ppm. Signals in this chemical shift region has been previously reported to be V coordinate Al sites.[140] The defect free wurtzite structure does not have any V coordinate sites, nor does the normal or inverse spinel. This V coordinate site is therefore attributed to interstitial Al coordinated to a single $V_{Ox}^{\cdot\cdot}$. The presence of an oxygen vacancy reduces the coordination sphere of the interstitial site to V and the defects are known to readily occur in ZnO.[7] Previous work examining free carrier pinning in MZO NCs led to the conclusion that the formation of f-centers (the pinning of free electrons at $V_{Ox}^{\cdot\cdot}$) is one of the significant sources of dopant deactivation for these materials.[135]

4.3.4 ^{67}Zn SSNMR

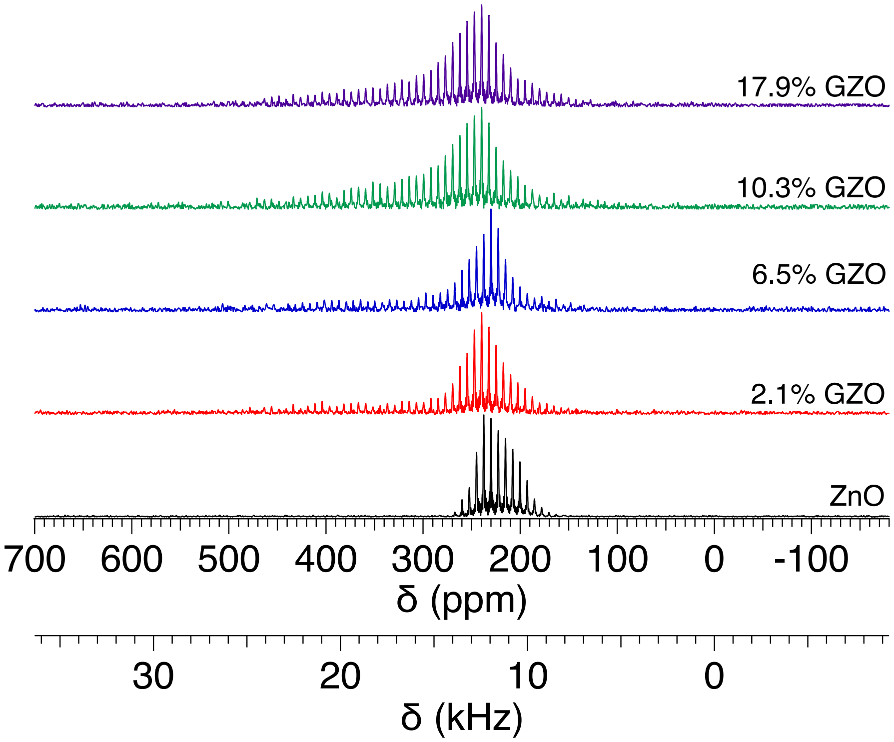

Figure 36. ^{67}Zn QCPMG spectra of X% Ga:ZnO NCs. Spectra were acquired under static conditions at 19.5 T (830 MHz).

^{67}Zn SSNMR experiments were performed on the GZO NCs to investigate the effects of pinned and delocalized carriers on a nucleus which composes most of the electronic band structure. Since AZO and GZO are n-type semiconductors, the free carriers reside in the conduction band of the NCs. Much of this conduction band is composed of Zn 4s orbitals,[142] which means there is a non-zero probability of the free carriers interacting with the ^{67}Zn nucleus. Figure 36 shows the QCPMG spectra for ZnO and X% GZO NCs. The undoped ZnO NC sample shows a single feature assigned to the IV coordinate Zn site in the wurtzite crystal structure.

Upon doping with Ga, the signal broadens asymmetrically towards higher frequencies. This change in the observed chemical shift is attributed to a Knight shift.[93] A Knight shift occurs when free carriers interact directly with nuclear spins and results in a paramagnetic enhancement of the nuclear relaxation rate. This phenomenon is typically only seen in metallic samples; however, the high carrier densities of degenerately doped semiconductors result in these samples becoming metallic in nature. It is important to note that the presence of s character at the Fermi level is key to the observation of a Knight shift, as the s orbital is the only orbital where there is a non-zero probability of the electron residing at the nucleus (ie. there is no node). Therefore, the Knight shift will only be observed in the ^{67}Zn spectra of MZO NCs and not the dopant NMR due to the nature of the electronic band structure. The conduction band of these nanomaterials is primarily composed of Zn 4s orbitals[142] and has little contribution from dopant states. This means that it statistically unlikely for a delocalized electron in the conduction band to interact with a dopant s orbital and cause a Knight shift.

The ^{67}Zn signal shifts primarily towards lower frequencies, which is indicative of a delocalization mechanism consistent with the presence of free carriers at the Fermi level.[67] While the observed LSPR does not shift with increased Ga doping, an increase in Knight shifted signal intensity is seen in the ^{67}Zn spectra as dopant concentration reaches >10%. This result signifies that the SSNMR spectra of GZO NCs is a more sensitive measure of free carrier density than the far-field infrared extinction measure of the LSPR. The integrated intensity of the Knight shifted feature increases from 0 to 10% Ga and then decreases at 18% doping. This result is further evidence of the formation of insulating spinel phases that begin to form more efficiently than aliovalent Ga substitutions and result in a net loss in free carrier density above a certain dopant threshold.

4.4 Conclusions

Al and Ga dopants were introduced into 10 nm ZnO NCs at varying concentrations to examine the underlying mechanisms behind free carrier generation. Analysis of the LSPR features for X% AZO and GZO using FTIR reveal that the plasmon resonance does not shift significantly with increasing dopant as would be expected. SSNMR was therefore used to investigate where the dopant ions are incorporating within the NC to identify what neutral defect complexes are formed. ^{71}Ga SSNMR experiments show a single, four-coordinate Ga site at low doping levels, indicative of aliovalent substitutional dopant incorporation at the C_{3v} Zn site. As the dopant concentration increases, a six coordinate Ga site increases in intensity. This site reflects the interstitial incorporation of Ga into the octahedral holes within the wurtzite ZnO crystal structure. ^{27}Al SSNMR experiments provide further insight due to the sharper line features of ^{27}Al. Al dopants are shown to incorporate into four unique crystalline environments, including a highly crystalline substitution on the Zn site, a five-coordinate interstitial dopant site, as well evidence of the formation of the insulating spinel ($ZnAl_2O_4$) phase. ^{67}Zn SSNMR was used to investigate the effect of free carrier generation on the host lattice nuclei. The ^{67}Zn signal is shifted downfield as the dopant concentration increases, indicative of a Knight shift. The intensity of the Knight shifted intensity reaches a maximum at 10% Ga, which is likely near the crossover point where the spinel phase is primarily formed, and no further free carriers are created. This work identifies the crystalline sites in MZO NCs where dopants incorporate and how this effects the generation of free carriers and ultimately the observed LSPR.

APPENDIX

SURFACE DEPLETION WIDTH CALCULATIONS

The surface depletion region width equation and all appropriate constants for ZnO were adapted from ref. 134.

$$d = \left[\frac{2\varepsilon_{ZnO}\varepsilon_0\Phi_S}{e^2 N_D^+(T)}\right]^{1/2} \tag{16}$$

Here, d represents the width of the surface depletion region, ε_{ZnO} is the relative dielectric constant of ZnO (8.7), ε_0 is the permittivity of free space, Φ_S is the height of potential barrier calculated for ZnO (0.5 eV), e is the elementary charge of an electron, and $N_D^+(T)$ is the temperature dependent activated donor concentration (chosen to be 1 x 10^{21} cm^{-3} based on the $NOBF_4$ titration results).

Using these values, the surface depletion width is determined to be 0.7 nm for a ZnO material with a free carrier density of 1 x 10^{21} cm^{-3}. In order to calculate the percentage of dopant deactivation within a NC based on this depletion width, the volume of a 10 nm sphere is first calculated using the following equation,

$$V = \frac{4}{3}\pi r^3 \tag{17}$$

where V is the volume of the sphere and r is the radius. Then, the volume of the undepleted NC core is calculated by subtracting the depletion width from the diameter of the NC (10 – 0.7 = 9.3 nm) and calculating the volume of the resulting 9.3 nm sphere. The percentage of the NC affected by the surface depletion region can then be calculated using the following equation.

$$\%\ depleted\ volume = \frac{V_{10\ nm} - V_{9.3\ nm}}{V_{10\ nm}} * 100 \tag{18}$$

REFERENCES

(1) Kittel, C. *Kittel's Introduction to Solid State Physics*; John Wiley & Sons, Limited, 2018.

(2) Holgate, S. A. *Understanding Solid State Physics*; CRC Press, 2009.

(3) Ashcroft, N.; Mermin, N. D. *Solid State Physics*; 1976.

(4) Van Zeghbroeck, B. *Principles of Semiconductor Devices*; 2009.

(5) Green, M. A. Intrinsic Concentration, Effective Densities of States, and Effective Mass in Silicon. *J. Appl. Phys.* **1990**, *67* (6), 2944–2954.

(6) Agrawal, A.; Hum Cho, S.; Zandi, O.; Ghosh, S.; W. Johns, R.; J. Milliron, D. Localized Surface Plasmon Resonance in Semiconductor Nanocrystals. *Chem. Rev.* **2018**, *118* (6), 3121–3207.

(7) Soriano, V.; Galland, D. Photosensitivity of the EPR Spectrum of the F+ Center in ZnO. *Phys. status solidi* **1976**, *77* (2), 739–743.

(8) Ali, A.; Almowali, A. Doping, Vacancy Formation and Substitutional Effects on Semiconductor Selectivity of Rutile TiO 2 Crystal. *Chem. Mater. Res.* **2013**, *3*, 22–32.

(9) D. Lounis, S.; L. Runnerstrom, E.; Bergerud, A.; Nordlund, D.; J. Milliron, D. Influence of Dopant Distribution on the Plasmonic Properties of Indium Tin Oxide Nanocrystals. *J. Am. Chem. Soc.* **2014**, *136* (19), 7110–7116.

(10) Kanehara, M.; Koike, H.; Yoshinaga, T.; Teranishi, T. Indium Tin Oxide Nanoparticles with Compositionally Tunable Surface Plasmon Resonance Frequencies in the Near-IR Region. *J. Am. Chem. Soc.* **2009**, *131* (49), 17736–17737.

(11) Conti III, C. R.; Quiroz-Delfi, G.; S. Schwarck, J.; Chen, B.; F. Strouse, G. Carrier Density, Effective Mass, and Nuclear Relaxation Pathways in Plasmonic Sn:In2O3 Nanocrystals. *J. Phys. Chem. C* **2020**, *0* (0).

(12) Ma, K.; Zhou, N.; Yuan, M.; Li, D.; Yang, D. Tunable Surface Plasmon Resonance Frequencies of Monodisperse Indium Tin Oxide Nanoparticles by Controlling Composition, Size, and Morphology. *Nanoscale Res. Lett.* **2014**, *9* (1), 547.

(13) Heo, S.; Hum Cho, S.; J. Dahlman, C.; Agrawal, A.; J. Milliron, D. Influence of Crystalline and Shape Anisotropy on Electrochromic Modulation in Doped Semiconductor Nanocrystals. *ACS Energy Lett.* **2020**, *5* (8), 2662–2670.

(14) Heo, S.; Kim, J.; K. Ong, G.; J. Milliron, D. Template-Free Mesoporous Electrochromic Films on Flexible Substrates from Tungsten Oxide Nanorods. *Nano Lett.* **2017**, *17* (9), 5756–5761.

(15) Poole, C. P.; Owens, F. J. *Introduction to Nanotechnology*; Wiley, 2003.

(16) Haug, H.; Koch, S. *Quantum Theory of the Optical and Electronic Properties of Semiconductors*; World Scientific, 1994.

(17) Yu, P. Y.; Cardona, M. *Fundamentals of Semiconductors: Physics and Materials Properties*; Springer, 2001.

(18) Agrawal, A.; Johns, R. W.; Milliron, D. J. Control of Localized Surface Plasmon Resonances in Metal Oxide Nanocrystals. *Annu. Rev. Mater. Res.* **2017**, *47* (1), 1–31.

(19) Staller, C. M.; L. Gibbs, S.; A. Saez Cabezas, C.; J. Milliron, D. Quantitative Analysis of Extinction Coefficients of Tin-Doped Indium Oxide Nanocrystal Ensembles. *Nano Lett.* **2019**, *19* (11), 8149–8154.

(20) Fleischmann, M.; Hendra, P. J.; McQuillan, A. J. Raman Spectra of Pyridine Adsorbed at a Silver Electrode. *Chem. Phys. Lett.* **1974**, *26* (2), 163–166.

(21) Starowicz, Z.; Wojnarowska-Nowak, R.; Ozga, P.; Sheregii, E. M. The Tuning of the Plasmon Resonance of the Metal Nanoparticles in Terms of the SERS Effect. *Colloid Polym. Sci.* **2018**, *296* (6), 1029–1037.

(22) Milekhin, A. G.; Sveshnikova, L. L.; Duda, T. A.; Yeryukov, N. A.; Rodyakina, E. E.; Gutakovskii, A. K.; Batsanov, S. A.; Latyshev, A. V; Zahn, D. R. T. Surface-Enhanced Raman Spectroscopy of Semiconductor Nanostructures. *Phys. E Low-dimensional Syst. Nanostructures* **2016**, *75*, 210–222.

(23) Langer, J.; Jimenez de Aberasturi, D.; Aizpurua, J.; A. Alvarez-Puebla, R.; Auguié, B.; J. Baumberg, J.; C. Bazan, G.; E. J. Bell, S.; Boisen, A.; G. Brolo, A.; Choo, J.; Cialla-May, D.; Deckert, V.; Fabris, L.; Faulds, K.; Javier García de Abajo, F.; Goodacre, R.; Graham, D.; J. Haes, A.; L. Haynes, C.; Huck, C.; Itoh, T.; Käll, M.; Kneipp, J.; A. Kotov, N.; Kuang, H.; C. Le Ru, E.; Kwee Lee, H.; Li, J.-F.; Yi Ling, X.; A. Maier, S.; Mayerhöfer, T.; Moskovits, M.; Murakoshi, K.; Nam, J.-M.; Nie, S.; Ozaki, Y.; Pastoriza-Santos, I.; Perez-Juste, J.; Popp, J.; Pucci, A.; Reich, S.; Ren, B.; C. Schatz, G.; Shegai, T.; Schlücker, S.; Tay, L.-L.; George Thomas, K.; Tian, Z.-Q.; P. Van Duyne, R.; Vo-Dinh, T.; Wang, Y.; A. Willets, K.; Xu, C.; Xu, H.; Xu, Y.; S. Yamamoto, Y.; Zhao, B.; M. Liz-Marzán, L. Present and Future of Surface-Enhanced Raman Scattering. *ACS Nano* **2019**, *14* (1), 28–117.

(24) Hum Cho, S.; Ghosh, S.; J. Berkson, Z.; A. Hachtel, J.; Shi, J.; Zhao, X.; C. Reimnitz, L.; J. Dahlman, C.; Ho, Y.; Yang, A.; Liu, Y.; Idrobo, J.-C.; F. Chmelka, B.; J. Milliron, D. Syntheses of Colloidal F:In2O3 Cubes: Fluorine-Induced Faceting and Infrared Plasmonic Response. *Chem. Mater.* **2019**, *31* (7), 2661–2676.

(25) Tandon, B.; Ghosh, S.; J. Milliron, D. Dopant Selection Strategy for High-Quality Factor Localized Surface Plasmon Resonance from Doped Metal Oxide Nanocrystals. *Chem.*

Mater. **2019**, *31* (18), 7752–7760.

(26) G. Kravets, V.; V. Kabashin, A.; L. Barnes, W.; N. Grigorenko, A. Plasmonic Surface Lattice Resonances: A Review of Properties and Applications. *Chem. Rev.* **2018**, *118* (12), 5912–5951.

(27) Drude, P. Zur Elektronentheorie Der Metalle. *Ann. Phys.* **1900**, *306* (3), 566–613.

(28) Mendelsberg, R. J.; Garcia, G.; Milliron, D. J. Extracting Reliable Electronic Properties from Transmission Spectra of Indium Tin Oxide Thin Films and Nanocrystal Films by Careful Application of the Drude Theory. *J. Appl. Phys.* **2012**, *111* (6), 063515.

(29) Conti III, C. R.; Quiroz-Delfi, G.; Schwarck, J. S.; Chen, B.; Strouse, G. F. Carrier Density, Effective Mass, and Nuclear Relaxation Pathways in Plasmonic Sn:In 2 O 3 Nanocrystals . *J. Phys. Chem. C* **2020**, *124* (51), 28220–28229.

(30) Conti III, C, R..;McBride, J. R.;Strouse, G. F. Examining the Effect of Dopant Ionic Radius on Plasmonic M:ZnO Nanocrystals (M = Al3+, Ga3+, In3+). *J. Phys. Chem. C* **2021**, *0* (0).

(31) Fang, H.; Hegde, M.; Yin, P.; V. Radovanovic, P. Tuning Plasmon Resonance of In2O3 Nanocrystals throughout the Mid-Infrared Region by Competition between Electron Activation and Trapping. *Chem. Mater.* **2017**, *29* (11), 4970–4979.

(32) Derkachova, A.; Kolwas, K.; Demchenko, I. Dielectric Function for Gold in Plasmonics Applications: Size Dependence of Plasmon Resonance Frequencies and Damping Rates for Nanospheres. *Plasmonics* **2016**, *11* (3), 941–951.

(33) Chen, Z.; Zhuo, Y.; Tu, W.; Li, Z.; Ma, X.; Pei, Y.; Wang, G. High Mobility Indium Tin Oxide Thin Film and Its Application at Infrared Wavelengths: Model and Experiment. *Opt. Express* **2018**, *26* (17), 22123–22134.

(34) Schleife, A.; Neumann, M. D.; Esser, N.; Galazka, Z.; Gottwald, A.; Nixdorf, J.; Goldhahn, R.; Feneberg, M. Optical Properties of In $_2$ O $_3$ from Experiment and First-Principles Theory: Influence of Lattice Screening. *New J. Phys.* **2018**, *20* (5), 053016.

(35) Link, S.; A. El-Sayed, M. Size and Temperature Dependence of the Plasmon Absorption of Colloidal Gold Nanoparticles. *J. Phys. Chem. B* **1999**, *103* (21), 4212–4217.

(36) Moores, A.; Goettmann, F. The Plasmon Band in Noble Metal Nanoparticles: An Introduction to Theory and Applications. *New J. Chem.* **2006**, *30* (8), 1121–1132.

(37) Luther, J. M.; Jain, P. K.; Ewers, T.; Alivisatos, A. P. Localized Surface Plasmon Resonances Arising from Free Carriers in Doped Quantum Dots. *Nat. Mater.* **2011**, *10* (5), 361–366.

(38) Mattox, T. M.; Ye, X.; Manthiram, K.; Schuck, P. J.; Alivisatos, A. P.; Urban, J. J. Chemical Control of Plasmons in Metal Chalcogenide and Metal Oxide Nanostructures. *Adv. Mater.* **2015**, *27* (38), 5830–5837.

(39) Mkawi, E. M.; Ibrahim, K.; Ali, M. K. M.; Farrukh, M. A.; Mohamed, A. S. The Effect of Dopant Concentration on Properties of Transparent Conducting Al-Doped ZnO Thin Films for Efficient Cu2ZnSnS4 Thin-Film Solar Cells Prepared by Electrodeposition Method. *Appl. Nanosci.* **2015**, *5* (8), 993–1001.

(40) Dahlman, C. J.; Agrawal, A.; M. Staller, C.; Adair, J.; J. Milliron, D. Anisotropic Origins of Localized Surface Plasmon Resonance in N-Type Anatase TiO_2 Nanocrystals. *Chem. Mater.* **2019**, *31* (2), 502–511.

(41) Boriskina, S.; Tong, J.; Huang, Y.; Zhou, J.; Chiloyan, V.; Chen, G. Enhancement and Tunability of Near-Field Radiative Heat Transfer Mediated by Surface Plasmon Polaritons in Thin Plasmonic Films. *Photonics* **2015**, *2* (2), 659–683.

(42) Jin, S.; Sugawa, K.; Takeshima, N.; Tahara, H.; Igari, S.; Yoshinari, S.; Kurihara, Y.; Watanabe, S.; Enoki, M.; Sato, K.; Inoue, W.; Tokuda, K.; Akiyama, T.; Katoh, R.; Takase, K.; Ozawa, H.; Okazaki, T.; Watanabe, T.; Otsuki, J. Precise Control of Localized Surface Plasmon Wavelengths Is Needed for Effective Enhancement of Triplet–Triplet Annihilation-Based Upconversion Emission. *ACS Photonics* **2018**, *5* (12), 5025–5037.

(43) Skoog, D. A.; Holler, F. J.; Crouch, S. R. *Principles of Instrumental Analysis*; Thomson Brooks/Cole, 2007.

(44) Griffiths, P.; de Hasseth, J. A. *Fourier Transform Infrared Spectrometry*; Wiley-Blackwell, 2007.

(45) Gunter, H. *NMR Spectroscopy: Basic Principles, Concepts, and Applications in Chemistry*; Wiley-VCH, 2013.

(46) Reif, B.; Ashbrook, S. E.; Emsley, L.; Hong, M. Solid-State NMR Spectroscopy. *Nat. Rev. Methods Prim.* **2021**, *1* (1), 2.

(47) Carr, H. Y.; Purcell, E. M. Effects of Diffusion on Free Precession in Nuclear Magnetic Resonance Experiments. *Phys. Rev.* **1954**, *94* (3), 630–638.

(48) Meiboom, S.; Gill, D. Modified Spin-Echo Method for Measuring Nuclear Relaxation Times. *Rev. Sci. Instrum.* **1958**, *29* (8), 688–691.

(49) Berrettini, M. G.; Braun, G.; Hu, J. G.; Strouse, G. F. NMR Analysis of Surfaces and Interfaces in 2-Nm CdSe. *J. Am. Chem. Soc.* **2004**, *126* (22), 7063–7070.

(50) Pinto, L. F.; Marín-Montesinos, I.; Lloveras, V.; Muñoz-Gómez, J. L.; Pons, M.; Veciana, J.; Vidal-Gancedo, J. NMR Signal Enhancement of >50 000 Times in Fast Dissolution

Dynamic Nuclear Polarization. *Chem. Commun.* **2017**, *53* (26), 3757–3760.

(51) Hanrahan, M. P.; Stein, J. L.; Park, N.; Cossairt, B. M.; Rossini, A. J. Elucidating the Location of Cd2+ in Post-Synthetically Treated InP Quantum Dots Using Dynamic Nuclear Polarization 31P and 113Cd Solid-State NMR Spectroscopy. *J. Phys. Chem. C* **2021**, *125* (5), 2956–2965.

(52) Chen, Y.; W. Dorn, R.; P. Hanrahan, M.; Wei, L.; Blome-Fernández, R.; M. Medina-Gonzalez, A.; A. S. Adamson, M.; H. Flintgruber, A.; Vela, J.; J. Rossini, A. Revealing the Surface Structure of CdSe Nanocrystals by Dynamic Nuclear Polarization-Enhanced ^{77}Se and ^{113}Cd Solid-State NMR Spectroscopy. *J. Am. Chem. Soc.* **2021**, *143* (23), 8747–8760.

(53) J. Mendelsberg, R.; Garcia, G.; Li, H.; Manna, L.; J. Milliron, D. Understanding the Plasmon Resonance in Ensembles of Degenerately Doped Semiconductor Nanocrystals. *J. Phys. Chem. C* **2012**, *116* (22), 12226–12231.

(54) A. Balitskii, O.; Sytnyk, M.; Stangl, J.; Primetzhofer, D.; Groiss, H.; Heiss, W. Tuning the Localized Surface Plasmon Resonance in Cu2–XSe Nanocrystals by Postsynthetic Ligand Exchange. *ACS Appl. Mater. & Interfaces* **2014**, *6* (20), 17770–17775.

(55) H. Hartstein, K.; M. Schimpf, A.; Salvador, M.; R. Gamelin, D. Cyclotron Splittings in the Plasmon Resonances of Electronically Doped Semiconductor Nanocrystals Probed by Magnetic Circular Dichroism Spectroscopy. *J. Phys. Chem. Lett.* **2017**, *8* (8), 1831–1836.

(56) Mattox, T. M.; Coffman, D. K.; Roh, I.; Sims, C.; Urban, J. J. Moving the Plasmon of LaB_6 from IR to Near-IR via Eu-Doping. *Materials* . 2018.

(57) B. Mogensen, K.; Kneipp, K. Size-Dependent Shifts of Plasmon Resonance in Silver Nanoparticle Films Using Controlled Dissolution: Monitoring the Onset of Surface Screening Effects. *J. Phys. Chem. C* **2014**, *118* (48), 28075–28083.

(58) Zhao, T.; W. Jarrett, J.; S. Johnson, J.; Park, K.; A. Vaia, R.; L. Knappenberger, K. Plasmon Dephasing in Gold Nanorods Studied Using Single-Nanoparticle Interferometric Nonlinear Optical Microscopy. *J. Phys. Chem. C* **2016**, *120* (7), 4071–4079.

(59) Zhang, X.; Huang, C.; Wang, M.; Huang, P.; He, X.; Wei, Z. Transient Localized Surface Plasmon Induced by Femtosecond Interband Excitation in Gold Nanoparticles. *Sci. Rep.* **2018**, *8* (1), 10499.

(60) Buonsanti, R.; Llordes, A.; Aloni, S.; A. Helms, B.; J. Milliron, D. Tunable Infrared Absorption and Visible Transparency of Colloidal Aluminum-Doped Zinc Oxide Nanocrystals. *Nano Lett.* **2011**, *11* (11), 4706–4710.

(61) Burstein, E. Anomalous Optical Absorption Limit in InSb. *Phys. Rev.* **1954**, *93* (3), 632–633.

(62) Moss, T. S. The Interpretation of the Properties of Indium Antimonide. *Proc. Phys. Soc. Sect. B* **1954**, *67* (10), 775–782.

(63) Mendelsberg, R. J.; Zhu, Y.; Anders, A. Determining the Nonparabolicity Factor of the CdO Conduction Band Using Indium Doping and the Drude Theory. *J. Phys. D. Appl. Phys.* **2012**, *45* (42), 425302.

(64) Muñoz, M.; Pollak, F. H.; Kahn, M.; Ritter, D.; Kronik, L.; Cohen, G. M. Burstein-Moss Shift of n-Doped $In_{0.53}Ga_{0.47}As$/InP. *Phys. Rev. B* **2001**, *63* (23), 233302.

(65) Kim, S.; Park, J.; Kim, S.; Lee, Y.; Ahn, S.; Cho, J.; Ju, M.; Lakshminarayan, N.; Dao, V. A.; Yi, J. Free-Carrier Absorption and Burstein–Moss Shift Effect on Quantum Efficiency in Heterojunction Silicon Solar Cells. *Vacuum* **2014**, *108*, 39–44.

(66) -C. Sun, Q.; Yadgarov, L.; Rosentsveig, R.; Seifert, G.; Tenne, R.; L. Musfeldt, J. Observation of a Burstein–Moss Shift in Rhenium-Doped MoS_2 Nanoparticles. *ACS Nano* **2013**, *7* (4), 3506–3511.

(67) Bertini, I.; Luchinat, C.; Parigi, G.; Ravera, E. Chapter 4 - Relaxation. In *NMR of Paramagnetic Molecules (Second Edition)*; Bertini, I., Luchinat, C., Parigi, G., Ravera, E., Eds.; Elsevier: Boston, 2017; pp 77–126.

(68) Pell, A. J.; Pintacuda, G.; Grey, C. P. Paramagnetic NMR in Solution and the Solid State. *Prog. Nucl. Magn. Reson. Spectrosc.* **2019**, *111*, 1–271.

(69) Liu, Z.; Beaulac, R. Nature of the Infrared Transition of Colloidal Indium Nitride Nanocrystals: Nonparabolicity Effects on the Plasmonic Behavior of Doped Semiconductor Nanomaterials. *Chem. Mater.* **2017**, *29* (17), 7507–7514.

(70) E. Marbella, L.; Yee Gan, X.; C. Kaseman, D.; E. Millstone, J. Correlating Carrier Density and Emergent Plasmonic Features in $Cu_{2-X}Se$ Nanoparticles. *Nano Lett.* **2017**, *17* (4), 2414–2419.

(71) Levin, E. M. Effects of Ge Substitution in GeTe by Ag or Sb on the Seebeck Coefficient and Carrier Concentration Derived from ^{125}Te NMR. *Phys. Rev. B* **2016**, *93* (4), 45209.

(72) Levin, E. M.; Cook, B. A.; Ahn, K.; Kanatzidis, M. G.; Schmidt-Rohr, K. Electronic Inhomogeneity and Ag:Sb Imbalance of $Ag_{1-y}Pb_{18}Sb_{1+z}Te_{20}$ High-Performance Thermoelectrics Elucidated by ^{125}Te and ^{207}Pb NMR. *Phys. Rev. B* **2009**, *80* (11), 115211.

(73) Runnerstrom, E. L.; Llordés, A.; Lounis, S. D.; Milliron, D. J. Nanostructured Electrochromic Smart Windows: Traditional Materials and NIR-Selective Plasmonic Nanocrystals. *Chem. Commun.* **2014**, *50* (73), 10555–10572.

(74) Xu, J.; Zhang, Y.; Zhai, T.-T.; Kuang, Z.; Li, J.; Wang, Y.; Gao, Z.; Song, Y.-Y.; Xia, X.-H. Electrochromic-Tuned Plasmonics for Photothermal Sterile Window. *ACS Nano* **2018**,

12 (7), 6895–6903.

(75) Lemos de Souza, M.; Pereira dos Santos, D.; Corio, P. Localized Surface Plasmon Resonance Enhanced Photocatalysis: An Experimental and Theoretical Mechanistic Investigation. *RSC Adv.* **2018**, *8* (50), 28753–28762.

(76) Gellé, A.; Moores, A. Water Splitting Catalyzed by Titanium Dioxide Decorated with Plasmonic Nanoparticles. *Pure Appl. Chem.* **2017**, *89* (12), 1817–1827.

(77) Wang, S.; Riedinger, A.; Li, H.; Fu, C.; Liu, H.; Li, L.; Liu, T.; Tan, L.; J. Barthel, M.; Pugliese, G.; De Donato, F.; Scotto D'Abbusco, M.; Meng, X.; Manna, L.; Meng, H.; Pellegrino, T. Plasmonic Copper Sulfide Nanocrystals Exhibiting Near-Infrared Photothermal and Photodynamic Therapeutic Effects. *ACS Nano* **2015**, *9* (2), 1788–1800.

(78) Liu, Z.; Liu, X.; Du, Y.; Ren, J.; Qu, X. Using Plasmonic Copper Sulfide Nanocrystals as Smart Light-Driven Sterilants. *ACS Nano* **2015**, *9* (10), 10335–10346.

(79) Ito, D.; Yokoyama, S.; Zaikova, T.; Masuko, K.; E. Hutchison, J. Synthesis of Ligand-Stabilized Metal Oxide Nanocrystals and Epitaxial Core/Shell Nanocrystals via a Lower-Temperature Esterification Process. *ACS Nano* **2014**, *8* (1), 64–75.

(80) González, G. B.; Mason, T. O.; Quintana, J. P.; Warschkow, O.; Ellis, D. E.; Hwang, J.-H.; Hodges, J. P.; Jorgensen, J. D. Defect Structure Studies of Bulk and Nano-Indium-Tin Oxide. *J. Appl. Phys.* **2004**, *96* (7), 3912–3920.

(81) Frank, G.; Köstlin, H. Electrical Properties and Defect Model of Tin-Doped Indium Oxide Layers. *Appl. Phys. A* **1982**, *27* (4), 197–206.

(82) D. Lounis, S.; L. Runnerstrom, E.; Llordés, A.; J. Milliron, D. Defect Chemistry and Plasmon Physics of Colloidal Metal Oxide Nanocrystals. *J. Phys. Chem. Lett.* **2014**, *5* (9), 1564–1574.

(83) Zandi, O.; Agrawal, A.; Shearer, A. B.; Reimnitz, L. C.; Dahlman, C. J.; Staller, C. M.; Milliron, D. J. Impacts of Surface Depletion on the Plasmonic Properties of Doped Semiconductor Nanocrystals. *Nat. Mater.* **2018**, *17* (8), 710–717.

(84) Jung, J.; Pedersen, T. G. Analysis of Plasmonic Properties of Heavily Doped Semiconductors Using Full Band Structure Calculations. *J. Appl. Phys.* **2013**, *113* (11), 114904.

(85) Bel Hadj Tahar, R.; Ban, T.; Ohya, Y.; Takahashi, Y. Tin Doped Indium Oxide Thin Films: Electrical Properties. *J. Appl. Phys.* **1998**, *83* (5), 2631–2645.

(86) Liu, X.; Park, J.; Kang, J.-H.; Yuan, H.; Cui, Y.; Hwang, H. Y.; Brongersma, M. L. Quantification and Impact of Nonparabolicity of the Conduction Band of Indium Tin Oxide on Its Plasmonic Properties. *Appl. Phys. Lett.* **2014**, *105* (18), 181117.

(87) Tauc, J. Optical Properties and Electronic Structure of Amorphous Ge and Si. *Mater. Res. Bull.* **1968**, *3* (1), 37–46.

(88) Khusayfan, N. M.; El-Nahass, M. M. Study of Structure and Electro-Optical Characteristics of Indium Tin Oxide Thin Films. *Adv. Condens. Matter Phys.* **2013**, *2013*, 408182.

(89) Gupta, L.; Mansingh, A.; Srivastava, P. K. Band Gap Narrowing and the Band Structure of Tin-Doped Indium Oxide Films. *Thin Solid Films* **1989**, *176* (1), 33–44.

(90) Wang, L.; E. Kefalidis, C.; Roisnel, T.; Sinbandhit, S.; Maron, L.; Carpentier, J.-F.; Sarazin, Y. Structure vs 119Sn NMR Chemical Shift in Three-Coordinated Tin(II) Complexes: Experimental Data and Predictive DFT Computations. *Organometallics* **2014**, *34* (11), 2139–2150.

(91) Hamaed, H.; Johnston, K. E.; Cooper, B. F. T.; Terskikh, V. V; Ye, E.; Macdonald, C. L. B.; Arnold, D. C.; Schurko, R. W. A 115In Solid-State NMR Study of Low Oxidation-State Indium Complexes. *Chem. Sci.* **2014**, *5* (3), 982–995.

(92) Townes, C. H.; Herring, C.; Knight, W. D. The Effect of Electronic Paramagnetism on Nuclear Magnetic Resonance Frequencies in Metals. *Phys. Rev.* **1950**, *77* (6), 852–853.

(93) Rubens, A.; deCastro, B.; Schumacher, R. T. Knight-Shift Anisotropy in Cubic Crystals. *Phys. Rev. B* **1973**, *7* (1), 105–118.

(94) Abraham, R. J. Principles of Magnetic Resonance. C. P. Slichter. Springer, Berlin, 1990, ISBN 3 540 5057 6, 640 Pages, DM89.00. *Magn. Reson. Chem.* **1990**, *28* (12), 1078.

(95) Dey, T.; Khuntia, P.; Mahajan, A. V.; Kumar, N.; Sundaresan, A. ^{119}Sn NMR Probe of Magnetic Fluctuations in SnO $_2$ Nanoparticles. *EPL (Europhysics Lett.* **2011**, *96* (6), 67008.

(96) Tunstall, D. P.; Patou, S.; Liu, R. S.; Kao, Y. H. Size Effects in the NMR of SnO_2 Powders. *Mater. Res. Bull.* **1999**, *34* (10), 1513–1520.

(97) szántay Jr., C. NMR and the Uncertainty Principle: How to and How Not to Interpret Homogeneous Line Broadening and Pulse Nonselectivity. I. The Fundamentals. *Concepts Magn. Reson. Part A* **2007**, *30A* (6), 309–348.

(98) Chavhan, G. B.; Babyn, P. S.; Thomas, B.; Shroff, M. M.; Haacke, E. M. Principles, Techniques, and Applications of T^{2*}-Based MR Imaging and Its Special Applications. *RadioGraphics* **2009**, *29* (5), 1433–1449.

(99) Weiss, A. G. S. Carter, L. H. Bennett, D. J. Kahan: Metallic Shifts in NMR, A Review of Theory and Comprehensive Critical Data Compilation of Metallic Materials. Part I—IV (Progress in Materials Science, Vol. 20, Editors: B. Chalmers, J. W. Christian, T. B.

Massals. *Berichte der Bunsengesellschaft für Phys. Chemie* **1977**, *81* (8), 779–780.

(100) Milman, V. Klockmannite, CuSe: Structure, Properties and Phase Stability from Ab Initio Modeling. *Acta Crystallogr. Sect. B* **2002**, *58* (3 Part 2), 437–447.

(101) Tyagi, K.; Gahtori, B.; Bathula, S.; Auluck, S.; Dhar, A. Band Structure and Transport Studies of Copper Selenide: An Efficient Thermoelectric Material. *Appl. Phys. Lett.* **2014**, *105* (17), 173905.

(102) Mryasov, O. N.; Freeman, A. J. Electronic Band Structure of Indium Tin Oxide and Criteria for Transparent Conducting Behavior. *Phys. Rev. B* **2001**, *64* (23), 233111.

(103) Liu, Z.; Zhong, Y.; Shafei, I.; Borman, R.; Jeong, S.; Chen, J.; Losovyj, Y.; Gao, X.; Li, N.; Du, Y.; Sarnello, E.; Li, T.; Su, D.; Ma, W.; Ye, X. Tuning Infrared Plasmon Resonances in Doped Metal-Oxide Nanocrystals through Cation-Exchange Reactions. *Nat. Commun.* **2019**, *10* (1), 1394.

(104) Yin, H.; Kuwahara, Y.; Mori, K.; Louis, C.; Yamashita, H. Properties, Fabrication and Applications of Plasmonic Semiconductor Nanocrystals. *Catal. Sci. Technol.* **2020**, *10* (13), 4141–4163.

(105) Law, S.; Yu, L.; Rosenberg, A.; Wasserman, D. All-Semiconductor Plasmonic Nanoantennas for Infrared Sensing. *Nano Lett.* **2013**, *13* (9), 4569–4574.

(106) Stewart, M. E.; Anderton, C. R.; Thompson, L. B.; Maria, J.; Gray, S. K.; Rogers, J. A.; Nuzzo, R. G. Nanostructured Plasmonic Sensors. *Chem. Rev.* **2008**, *108* (2), 494–521.

(107) Elsayed, M. Y.; Ismail, Y.; Swillam, M. A. Semiconductor Plasmonic Gas Sensor Using On-Chip Infrared Spectroscopy. *Appl. Phys. A* **2017**, *123* (1), 113.

(108) Garcia, G.; Buonsanti, R.; Llordés, A.; Runnerstrom, E.; Bergerud, A.; Milliron, D. Near-Infrared Spectrally Selective Plasmonic Electrochromic Thin Films. *Adv. Opt. Mater.* **2013**, *1*.

(109) Manzi, A.; Simon, T.; Sonnleitner, C.; Döblinger, M.; Wyrwich, R.; Stern, O.; K. Stolarczyk, J.; Feldmann, J. Light-Induced Cation Exchange for Copper Sulfide Based CO_2 Reduction. *J. Am. Chem. Soc.* **2015**, *137* (44), 14007–14010.

(110) Lou, Z.; Gu, Q.; Liao, Y.; Yu, S.; Xue, C. Promoting Pd-Catalyzed Suzuki Coupling Reactions through near-Infrared Plasmon Excitation of WO_{3-x} Nanowires. *Appl. Catal. B Environ.* **2016**, *184*, 258–263.

(111) Della Gaspera, E.; S. R. Chesman, A.; van Embden, J.; J. Jasieniak, J. Non-Injection Synthesis of Doped Zinc Oxide Plasmonic Nanocrystals. *ACS Nano* **2014**, *8* (9), 9154–9163.

(112) Wainer, P.; Kendall, O.; Lamb, A.; J. Barrow, S.; Tricoli, A.; E. Gómez, D.; van Embden, J.; Della Gaspera, E. Continuous Growth Synthesis of Zinc Oxide Nanocrystals with Tunable Size and Doping. *Chem. Mater.* **2019**, *31* (23), 9604–9613.

(113) M. Schimpf, A.; D. Lounis, S.; L. Runnerstrom, E.; J. Milliron, D.; R. Gamelin, D. Redox Chemistries and Plasmon Energies of Photodoped In_2O_3 and Sn-Doped In_2O_3 (ITO) Nanocrystals. *J. Am. Chem. Soc.* **2015**, *137* (1), 518–524.

(114) Hu, W.; Guo, S.; P. Gaul, J.; G. Boebinger, M.; T. McDowell, M.; A. Filler, M. Reversible Tuning of the Surface Plasmon Resonance of Indium Tin Oxide Nanocrystals by Gas-Phase Oxidation and Reduction. *J. Phys. Chem. C* **2017**, *121* (29), 15970–15976.

(115) Sakamoto, M.; Kawawaki, T.; Kimura, M.; Yoshinaga, T.; Vequizo, J. J. M.; Matsunaga, H.; Ranasinghe, C. S. K.; Yamakata, A.; Matsuzaki, H.; Furube, A.; Teranishi, T. Clear and Transparent Nanocrystals for Infrared-Responsive Carrier Transfer. *Nat. Commun.* **2019**, *10* (1), 406.

(116) Janotti, A.; Van de Walle, C. G. Fundamentals of Zinc Oxide as a Semiconductor. *Reports Prog. Phys.* **2009**, *72* (12), 126501.

(117) Liu, L.; Mei, Z.; Tang, A.; Azarov, A.; Kuznetsov, A.; Xue, Q.-K.; Du, X. Oxygen Vacancies: The Origin of *n*-Type Conductivity in ZnO. *Phys. Rev. B* **2016**, *93* (23), 235305.

(118) Erhart, P.; Klein, A.; Albe, K. First-Principles Study of the Structure and Stability of Oxygen Defects in Zinc Oxide. *Phys. Rev. B* **2005**, *72* (8), 85213.

(119) Boriskina, S. V; Ghasemi, H.; Chen, G. Plasmonic Materials for Energy: From Physics to Applications. *Mater. Today* **2013**, *16* (10), 375–386.

(120) Look, D. C.; Leedy, K. D.; Vines, L.; Svensson, B. G.; Zubiaga, A.; Tuomisto, F.; Doutt, D. R.; Brillson, L. J. Self-Compensation in Semiconductors: The Zn Vacancy in Ga-Doped ZnO. *Phys. Rev. B* **2011**, *84* (11), 115202.

(121) Bragg, W. H.; Bragg, W. L. The Reflection of X-Rays by Crystals. *Proc. R. Soc. London. Ser. A, Contain. Pap. a Math. Phys. Character* **1913**, *88* (605), 428–438.

(122) Shannon, R. Revised Effective Ionic Radii and Systematic Studies of Interatomic Distances in Halides and Chalcogenides. *Acta Crystallogr. Sect. A* **1976**, *32* (5), 751–767.

(123) Vegard, L. Die Konstitution Der Mischkristalle Und Die Raumfüllung Der Atome. *Zeitschrift für Phys.* **1921**, *5* (1), 17–26.

(124) Brehm, J. U.; Winterer, M.; Hahn, H. Synthesis and Local Structure of Doped Nanocrystalline Zinc Oxides. *J. Appl. Phys.* **2006**, *100* (6), 64311.

(125) Muth, J. F.; Kolbas, R. M.; Sharma, A. K.; Oktyabrsky, S.; Narayan, J. Excitonic Structure and Absorption Coefficient Measurements of ZnO Single Crystal Epitaxial Films Deposited by Pulsed Laser Deposition. *J. Appl. Phys.* **1999**, *85* (11), 7884–7887.

(126) Oshikiri, M.; Imanaka, Y.; Aryasetiawan, F.; Kido, G. Comparison of the Electron Effective Mass of the N-Type ZnO in the Wurtzite Structure Measured by Cyclotron Resonance and Calculated from First Principle Theory. *Phys. B Condens. Matter* **2001**, *298* (1), 472–476.

(127) Calzolari, A.; Nardelli, M. B. Dielectric Properties and Raman Spectra of ZnO from a First Principles Finite-Differences/Finite-Fields Approach. *Sci. Rep.* **2013**, *3* (1), 2999.

(128) Nakrela, A.; Benramdane, N.; Bouzidi, A.; Kebbab, Z.; Medles, M.; Mathieu, C. Site Location of Al-Dopant in ZnO Lattice by Exploiting the Structural and Optical Characterisation of ZnO:Al Thin Films. *Results Phys.* **2016**, *6*, 133–138.

(129) Gabás, M.; Torelli, P.; Barrett, N. T.; Sacchi, M.; Ramos Barrado, J. R. Electronic Structure of Al- and Ga-Doped ZnO Films Studied by Hard X-Ray Photoelectron Spectroscopy. *APL Mater.* **2014**, *2* (1), 12112.

(130) Kröger, F. A.; Vink, H. J. Relations between the Concentrations of Imperfections in Crystalline Solids; Seitz, F., Turnbull, D. B. T.-S. S. P., Eds.; Academic Press, 1956; Vol. 3, pp 307–435.

(131) Zheng, W.; Singh, K.; Wang, Z.; T. Wright, J.; van Tol, J.; S. Dalal, N.; W. Meulenberg, R.; F. Strouse, G. Evidence of a $ZnCr_2Se_4$ Spinel Inclusion at the Core of a Cr-Doped ZnSe Quantum Dot. *J. Am. Chem. Soc.* **2012**, *134* (12), 5577–5585.

(132) E. Foley, M.; W. Meulenberg, R.; R. McBride, J.; F. Strouse, G. Eu^{3+}-Doped ZnB_2O_4 (B = Al^{3+}, Ga^{3+}) Nanospinels: An Efficient Red Phosphor. *Chem. Mater.* **2015**, *27* (24), 8362–8374.

(133) Tandon, B.; Agrawal, A.; Heo, S.; J. Milliron, D. Competition between Depletion Effects and Coupling in the Plasmon Modulation of Doped Metal Oxide Nanocrystals. *Nano Lett.* **2019**, *19* (3), 2012–2019.

(134) Liao, Z.-M.; Zhang, H.-Z.; Zhou, Y.-B.; Xu, J.; Zhang, J.-M.; Yu, D.-P. Surface Effects on Photoluminescence of Single ZnO Nanowires. *Phys. Lett. A* **2008**, *372* (24), 4505–4509.

(135) Wei, W. F. F+ Center in ZnO. *Phys. Rev. B* **1977**, *15* (4), 2250–2253.

(136) Donovan, B. F.; Sachet, E.; Maria, J.-P.; Hopkins, P. E. Interplay between Mass-Impurity and Vacancy Phonon Scattering Effects on the Thermal Conductivity of Doped Cadmium Oxide. *Appl. Phys. Lett.* **2016**, *108* (2), 21901.

(137) Hwang, J.-H.; Edwards, D. D.; Kammler, D. R.; Mason, T. O. Point Defects and Electrical Properties of Sn-Doped In-Based Transparent Conducting Oxides. *Solid State Ionics* **2000**, *129* (1), 135–144.

(138) Liu, Z.; Liu, X.; Du, Y.; Ren, J.; Qu, X. Using Plasmonic Copper Sulfide Nanocrystals as Smart Light-Driven Sterilants. *ACS Nano* **2015**, *9* (10), 10335–10346.

(139) A. Hardy, D.; A. Tigaa, R.; R. McBride, J.; E. Ortega, R.; F. Strouse, G. Structure–Function Correlation: Engineering High Quantum Yields in Down-Shifting Nanophosphors. *J. Am. Chem. Soc.* **2019**, *141* (51), 20416–20423.

(140) Martineau, C.; Taulelle, F.; Haouas, M. The Use of ^{27}Al NMR to Study Aluminum Compounds: A Survey of the Last 25 Years. *PATAI'S Chemistry of Functional Groups*. March 31, 2016, pp 1–51.

(141) Avadhut, Y. S.; Weber, J.; Hammarberg, E.; Feldmann, C.; Schmedt auf der Günne, J. Structural Investigation of Aluminium Doped ZnO Nanoparticles by Solid-State NMR Spectroscopy. *Phys. Chem. Chem. Phys.* **2012**, *14* (33), 11610–11625.

(142) Mora-Fonz, D.; Buckeridge, J.; J. Logsdail, A.; O. Scanlon, D.; A. Sokol, A.; Woodley, S.; Richard A. Catlow, C. Morphological Features and Band Bending at Nonpolar Surfaces of ZnO. *J. Phys. Chem. C* **2015**, *119* (21), 11598–11611.

BIOGRAPHICAL SKETCH

Education

Florida State University
Tallahassee, FL
Ph.D. Materials Chemistry: 2018-2022
M.S. Materials Chemistry: 2020
Awards: 2018 Hoffman Fellowship, 2021 Rmaile and Usher Endowed Fellowship Award, 2022 GSSPC Co-Chair

Michigan State University
East Lansing, MI
B.S. Chemistry, Minor Spanish: 2016
Awards: 2016 ACS Yates Award for Inorganic Chemistry

Experience

10/2021-Present **Senior Engineer**
Raytheon Technologies – McKinney, TX

- Chemistry subject matter expert in the McKinney Failure Analysis Lab
- Provide detailed failure analysis assessments and solutions for Raytheon Technologies programs
- Collaborate with multi-disciplinary team of scientists and engineers

07/2018-04/2022 **Graduate Student Researcher**
Florida State University – Tallahassee, FL

- Synthesize and characterize plasmonic semiconductor nanocrystals (NCs) with varying sizes/dopants
- Collaborate with various groups at FSU and outside universities
- Written successful proposal funded by the NSF for plasmonics research
- Written successful proposals for various user facilities (NHMFL, LBNL)

01/2017-06/2018 **Laboratory Technician**
XG Sciences – Lansing, MI

- Worked with customers to produce value-added products utilizing our exfoliated graphene nanoplatelets (xGnP)
- Conducted original research for IP generation in fields of lithium-ion batteries, polymers, and graphene nanoplatelets

04/2016-12/2016 **Undergraduate Student Researcher**
Michigan State University – East Lansing, MI

- Synthesized organometallic complexes using strict air-free techniques
- Characterized samples via NMR, GC-MS, and XRD

Publications

Conti III, C. R.; Smith, R.; Altenhof, A. R.; Schurko, R. W.; Strouse, G. F.* Probing the Origin of Free Carriers in Plasmonic M:ZnO Nanocrystals (M=Al^{3+}, Ga^{3+}) via Multinuclear SSNMR. **In Preparation**

Kuszynski, J. E.; Kays, J. C.; **Conti III, C. R.**; McGill, S. A.; Dennis, A. M. Strouse, G. F.* Investigation of the Cu:Fe Ratio on Effective Carrier Mass and Density for Cu_xFeS_4 (x=7, 5, 3) through Magnetic Circular Dichroism. **In Preparation**

Conti III, C. R.; Bieber, A. S.; VanOrman, Z. A.; Moller, G.; Wieghold, S.; Schaller, R. D.; Strouse, G. F.; Nienhaus, L.* Ultrafast Triplet Generation at the Lead Halide Perovskite/Rubrene Interface. *ACS Energy Lett.* **2022**, *7*, 617-623. DOI: 10.1021/acsenergylett.1c02732

Kays, J. C.; **Conti III, C. R.**; Margaronis, A.; Kuszynski, J. E.; Strouse, G. F.; Dennis, A. M.* Controlled Synthesis and Exploration of Cu_xFeS_4 Bornite Nanocrystals. *Chem. Mater.* **2021**, *33*, 7408-7416. DOI: 10.1021/acs.chemmater.1c02029

Conti III, C. R.; McBride, J. R.; Strouse, G. F.* Examining the Effect of Dopant Ionic Radius on Plasmonic M:ZnO Nanocrystals (M= Al^{3+}, Ga^{3+}, In^{3+}). *J. Phys. Chem. C.* **2021**, *125*, 7772-7779. DOI: 10.1021/acs.jpcc.1c00529

VanOrman, Z. A.; **Conti III, C. R.**; Strouse, G. F.; Nienhaus, L.* Red-to-Blue Photon Upconversion Enabled by One Dimensional CdTe Nanorods. *Chem. Mater.* **2021***, 33,* 452−458. DOI: 10.1021/acs.chemmater.0c04468

Conti III, C. R.; Quiroz-Delfi, G.; Schwarck, J. S.; Chen, B.; Strouse, G. F.* Carrier Density, Effective Mass, and Nuclear Relaxation Pathways in Plasmonic Sn:In_2O_3 Nanocrystals. *J. Phys. Chem. C* **2020***, 124,* 28220−28229. DOI: 10.1021/acs.jpcc.0c09448